

國立交通大學
光電工程研究所
碩士論文

使用半導體光放大器作光波波長之轉換

Wavelength Conversion Using
Semiconductor Optical Amplifiers

The logo of National Tsing Hua University is a circular emblem with a blue border. Inside the circle, there is a stylized representation of a building or a gear-like structure, and the university's name in Chinese characters is visible within the design.

研 究 生：魏 嘉 建

指 導 教 授：陳 智 弘 老 師

中 華 民 國 九 十 三 年 六 月

使用半導體光放大器作光波波長之轉換

Wavelength Conversion Using Semiconductor Optical Amplifiers

研究生：魏嘉建

Student : Chia-Chien Wei

指導教授：陳智弘 老師

Advisor : Assistant Prof. Jyehong Chen



A Thesis

Submitted to Institute of Electro-Optical Engineering
College of Electrical Engineering and Computer Science

National Chiao Tung University

In Partial Fulfillment of the Requirements

For the Degree of

Master

In

Institute of Electro-Optical Engineering

June 2004

Hsinchu, Taiwan, Republic of China

中華民國九十三年六月

ACKNOWLEDGEMENTS

能夠完成碩士的學業，我最要感謝的就是我的指導教授，陳智弘老師。沒有老師的因循善誘，我不可能從材料固態的領域跳到光纖通訊，並順利完成碩士論文，除了專業領域的幫助，陳老師生活態度給我的影響，也是我碩士生涯的另一個重大收穫。

還要感謝實驗室成員，宥燁、建宏、馥宇、峰生、偉志，他們的陪伴使我的碩士生涯更添色彩，並且在互相的討論中，讓我學習到更多；還有玉民學長在通訊領域、實驗硬體等各方面的幫助。另外，我要謝謝林恭如老師以及林俊榮學長在碩一時給我的指導與幫助。

我的高中同學兼室友，紀建宇，感謝他陪我度過那些最難熬的日子，與我分享生活中的點點滴滴。還有 Mars，牠使我的生活更加有趣。

最後，我最重要的家人，我的父、母親、大姐、二姐以及哥哥，感謝他們的包容，並讓我有一個溫暖的家。



嘉建 2004/06/09

使用半導體光放大器作光波波長之轉換

學生：魏嘉建

指導教授：陳智弘 老師

國立交通大學光電工程研究所碩士班

摘要

近幾年來，光通訊的高傳輸需求快速上升，波長多工有效地運用光纖的頻寬並提升系統傳輸量。而波長轉換器，除了在波長多工系統中扮演增加彈性與容量的重要角色外，也可在複雜的網狀通訊系統中作為管理訊號路徑的路由器。

在本篇論文中，我們模擬並實驗測試了四種藉由半導體光放大器作為波長轉換器的方法，包括了交叉增益調變、交叉相位調變、四波混頻、交叉極化調變，它們皆不需要經過光電轉換便能完成波長的轉換。另外，將從各個方面討論及比較這四種方法的優缺點，並從模擬中可以明白轉換過程的細節，而實驗則更可實際地測試訊號轉換的效能。

Wavelength Conversion Using Semiconductor Optical Amplifiers

Student : Chia-Chien Wei

Advisor : Dr. Jyehong Chen

Institute of Electro-Optical Engineering
National Chiao Tung University



Abstract

In recent years, the requirement for high speed transmission has increased rapidly. Wavelength Division multiplexed (WDM) networks which offer a very effective utilization of the fiber bandwidth directly in the wavelength domain can increase the system capacity. The role of wavelength converters can be to increase the flexibility and the capacity of WDM networks or be used in routers which manage the wavelength paths through the optical networks base on complex meshes, rather than point-to-point architectures.

In this thesis, four methods which convert signal from one wavelength to another without optoelectronic conversion by using SOA's, including cross gain modulation (XGM), cross phase modulation (XPM), four wave mixing (FWM), and cross polarization modulation, are simulated and experimented. The advantages and disadvantages of these schemes are compared and discussed in all respects. The simulations are helpful to realize details of conversion processes and the experiments test the performance of the conversions realistically.

CONTENTS

Acknowledgements	i
Chinese Abstract	ii
English Abstract	iii
Contents	iv
List of Figures	vii
List of Tables	x

CHAPTER 1 Introduction

1.1 Wavelength conversion in WDM system.....	1
1.2 Wavelength conversion in SOA's.....	3
1.3 Structure of the thesis.....	5

CHAPTER 2 Basic Concepts

2.1 Gain spectrum and rate equations of SOA's.....	6
2.1.1 Gain model of SOA's.....	6
2.1.2 Pulse propagation equations.....	8
2.2 Wave mixing in SOA's.....	10
2.2.1 Intraband processes in SOA's.....	10
2.2.2 Equations for inter- and intraband processes.....	12
2.3 Interference between TM and TE modes in SOA's.....	16

CHAPTER 3 Simulations

3.1 Simulation method for wavelength conversion.....	19
3.2 Simulation results and discussions of XGM.....	25
3.2.1 Overshoot and chirp of the converted signal.....	25

3.2.2	Modulation bandwidth for XGM.....	30
3.3	Simulation results and discussions of XPM.....	34
3.3.1	Operation point of XPM.....	34
3.3.2	Modulation bandwidth and polarization dependence for XPM.....	39
3.4	Simulation results and discussion of FWM.....	41
3.4.1	Frequency response of inter- and intraband processes.....	41
3.4.2	Spectral inversion due to FWM.....	43
3.4.3	ER improvement in rFWM.....	46
3.5	Simulation results and discussion of cross polarization modulation.....	49
3.5.1	Rotation of SOP in a SOA.....	49
3.5.2	Changing conversion styles by the polarizer.....	50

CHAPTER 4 Experiments and Results of Wavelength Converters

5.0	Cross gain modulation.....	54
4.1.1	Experimental setup.....	54
4.1.2	Performance analysis for XGM.....	56
4.1.3	The relation between BER and operation powers.....	57
4.1.4	Timing jitter for co- and counter-propagation.....	59
4.2	Cross phase modulation.....	60
4.2.1	Experimental setup.....	60
4.2.2	Performance analysis for XPM.....	61
4.2.3	Polarization dependent performance of XPM.....	63
4.3	Four wave mixing.....	65
4.3.1	Experimental setup.....	65
4.3.2	Performance analysis for FWM and rFWM.....	67
4.4	Cross polarization modulation.....	70

4.4.1 Experimental setup..... 70
4.4.2 Performance analysis for cross polarization modulation..... 71
4.4.3 Wavelength conversion to different wavelengths..... 75

CHAPTER 5 Conclusions

5.1 Cross gain modulation..... 76
5.2 Future works..... 78

Reference..... 79



LIST OF FIGURES

- Figure 1-1: Schema of the co- and counter-propagation XGM
- Figure 1-2: Schema of the XPM
- Figure 2-1: SOA schematic
- Figure 2-2: The inter- and intraband process in semiconductor.
- Figure 2-3: The schemata of interference between TE and TM mode
- Figure 3-1: Schematic of the TMM-based SOA model
- Figure 3-2: Schematic of transfer matrices
- Figure 3-3: Input signals pattern (upper), converted signals pattern (middle), and frequency chirp (lower) using XGM method.
- Figure 3-4: The variation of carrier density from the front to the end part of a SOA.
- Figure 3-5: Gain spectra for different signal powers (upper), and the ER of converted signal obtained by subtracting the -5 and -15 dBm gain spectra.
- Figure 3-6: Contour plot of output ER with different signal and CW wavelength
- Figure 3-7: Peak Chirp (solid lines) and the extinction ratio (dashed line) of converted signals using XGM scheme.
- Figure 3-8: Wavelength conversion with 10 Gbps input signal by XGM
- Figure 3-9: EOR and peak-to-peak chirp as a function of the data rate for different cavity length.
- Figure 3-10: Carrier distribution in longitudinal direction as level-1 signal input (left) and level-0 signal input (right)
- Figure 3-11: Eye diagrams of XGM in co- and counter-propagation configurations
- Figure 3-12: EOR of converted signal as a function of the data rate in co- and counter-propagation configurations.
- Figure 3-13: The phase shift with the gain saturation as a function of signal input

power

Figure 3-14: Transfer function of XPM wavelength converter by changing phase current

Figure 3-15: Pattern and frequency chirping of converted signals by XPM scheme. Upper and lower ones illustrate the non-inverted operation and inverted operation, respectively.

Figure 3-16: ER degradation as a function of the power and wavelength

Figure 3-17: EOR and peak chirp as a function of the bit-rate in XPM scheme

Figure 3-18: Static transfer function of XPM as a function of the polarization of the CW

Figure 3-19: Conversion efficiency by FWM as a function of wavelength shift

Figure 3-20: Illustration of directions of third-order susceptibilities

Figure 3-21: Pulse pattern and frequency chirping of the input signal (upper) and the converted signal (lower).

Figure 3-22: ER and parasitic chirp of the converted signal as a function of the pump and the signal power.

Figure 3-23: ER (upper) and conversion efficiency (lower) of the converted signal using rFWM scheme as a function of the pump and signal power.

Figure 3-24: Pulse pattern and frequency chirping of the input signal (upper) and the converted signal (lower) using rFWM scheme.

Figure 3-25: Parasitic peak chirp (upper) and overshoot (lower) of the converted signal using rFWM scheme as a function of the pump and signal power.

Figure 3-26: The paths of rotation of the output polarization in cross polarization modulation

Figure 3-27: Transfer function of the CW with different input polarization

containing inverted and non-inverted conversion.

Figure 3-28: Different transfer curves (solid lines) with different orientation of polarizer and the total CW output power (dashed line) decreases as input signal power increasing.

Figure 3-29: Input signal patten (1st), pulse pattern and frequency chirping of the non-inverted converted signal (2nd& 3rd) and the inverted converted signal (4th& 5th).

Figure 4-1: Experimental setup of counter-propagation XGM scheme.

Figure 4-2: Gain spectrums of the Alcatel SOA for different injection currents

Figure 4-3: The eye diagrams (left) and 2^7-1 PRBS pulse patterns (right) of the converted signal for back-to-back (upper) and transmission after 25 km of SMF28 fiber (lower) in counter-propagation XGM scheme.

Figure 4-4: BER curves of the input signal and converted signal

Figure 4-5: BER curve as a function of the input signal power

Figure 4-6: BER curve as a function of the CW power

Figure 4-7: The eye diagrams of the converted signal in co- (right) and counter- (left) propagation XGM schemes.

Figure 4-8: Experimental setup of co-propagation XPM scheme.

Figure 4-9: The BER curves of the input signal, non-inverted converted signal, and inverted converted signal with and without transmission.

Figure 4-10: Eye diagrams of the input signal (upper), the non-inverted conversion signal (middle), and inverted conversion signal (lower) for back-to-back (left) and transmission in 50 km SMF.

Figure 4-11: The static transfer function of XPM method on different polarization state of the input CW.

Figure 4-12: The eye diagrams and pulse patterns of the input signal (upper), the

best converted signal (middle), and the worst converted signal (lower).

Figure 4-13: Experimental setup of FWM scheme.

Figure 4-14: The conversion efficiency of FWM as a function of wavelength shift

Figure 4-15: The BER curves of the input signal and converted signal by FWM and rFWM scheme for back-to-back and transmission in 50 km SMF.

Figure 4-16: The eye diagrams of the signals converted by FWM (left) and rFWM (right) schemes. Conversion with large signal-to-pump power ratio of -4.5 dB (upper) and small signal-to-pump power ratio of -10.5 dB (middle) for back-to-back and transmission in 50 km SMF (lower).

Figure 4-17: Experimental setup of cross polarization modulation scheme.

Figure 4-18: The static transfer function of cross polarization scheme.

Figure 4-19: The BER curves of the original signal and conversion signals at 2.5 Gb/s and 5 Gb/s.

Figure 4-20: The eye diagrams of the 2.5 Gb/s inverted (1st row), 10 Gb/s inverted (2nd row), 2.5 Gb/s non-inverted (3rd row) and 10 Gb/s non-inverted (4th row) signals for back-to-back (left) and transmission in 50 km SMF (right).

Figure 4-21: The power penalties of the converted signal by cross polarization modulation as a function of CW wavelength.

LIST OF TABLES

Table 3-1: Device Parameters in SOA's

Table 3-2: Nonlinear Parameters in SOA's

CHAPTER 1

INTRODUCTION

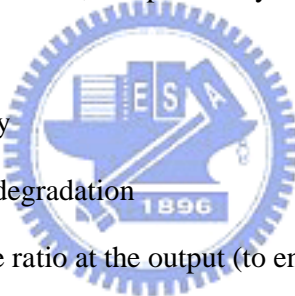
1.1 Wavelength Conversion in WDM Systems

In recent years, the requirement for high speed transmission has increased rapidly. Multimedia services, HDTV, and computer links in the national information highway will undoubtedly benefit us by improving the way of life and increasing efficiency. Single-mode fibers deployed in the public telecommunications network today can potentially accommodate more than 1 Tb/s traffic. Higher bit-rate at 40 Gb/s are becoming available, however, the dispersion and nonlinearities in the fiber severely limit the transmission distance. Wavelength Division multiplexed (WDM) networks which offer a very effective utilization of the fiber bandwidth directly in the wavelength domain, rather than in the time domain, can increase the system capacity. In addition, wavelength can be used to perform functions as routing and switching, which becomes an important consideration for realization of an all-optical transparent network layer in the network.

The number of wavelength in WDM networks determines the number of independent wavelength addresses, or paths. Although this number may be large enough to fulfill the required information capacity, it often is not large enough to support a large number of nodes. In such cases, the blocking probability rises due to possible wavelength contention when two channels at the same wavelength are to be routed at the same output. One method to overcome this limitation is to convert signals from one wavelength to another. Thereby, wavelength converters are expected to be key components. The role of wavelength converters can be to increase the flexibility and the capacity of WDM networks or be used in routers which

manage the wavelength paths through the optical networks base on complex meshes, rather than point-to-point architectures.

There are numerous techniques of wavelength conversion. Although Optoelectronic conversion (O/E-E/O) techniques have some advantages, such as signal regeneration, signal-to-noise ratio improvement, and re-timing, this methods face the cost penalties, especially for high bit-rate transmission, and this kind of the wavelength converters will be failed when the system bit-rate upgrades. For this reason, all-optical wavelength conversions (AOWC), which transform information from one wavelength to another in optical domain without optical-to-electrical conversion, are expected to be crucial components. The requirements to the converters will be system dependent, but preferably the converters should feature the following.

- 
- | Bit-rate transparency
 - | No extinction ratio degradation
 - | High signal-to-noise ratio at the output (to ensure cascadability)
 - | Moderate input power levels
 - | Large wavelength span for both input and output signals
 - | Possibility for same input and output wavelengths (no conversion)
 - | Low chirp
 - | Fast setup time of output wavelength
 - | Insensitivity to input signal polarization
 - | Format transparency
 - | Simple implementation

Many methods of AOWC have been proposed, for example, cross gain modulation (XGM) in semiconductor optical amplifiers (SOA) [1], cross phase modulation (XPM) in SOA [2], four wave mixing (FWM) in SOA [3], cross

polarization modulation in SOA [4], cross absorption modulation in electroabsorption modulator [5], cascaded second harmonic generation and difference frequency generation (SHG/DFG) in quasi-phase matching (QPM) periodically poled lithium-niobate (PPLN) [6], and sinusoidal amplitude and phase hybrid modulation [7], in which SOA's are popularly used because they generally appear to be most efficient.

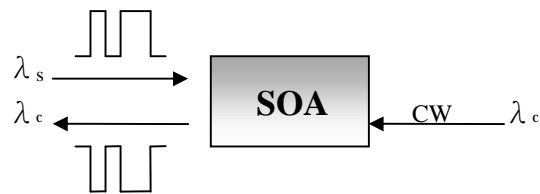
1.2 Wavelength Conversion in SOA's

In my thesis, AOWC's using SOA's are focused. The XGM, XPM, FWM, and cross polarization modulation schemes in SOA's are considered.

When an amplitude modulated input signal was transmitted to a SOA, the signal light will modulate the carrier density and consequently also the gain of the SOA provided that the optical power exceeded the saturation power of the SOA. In addition, a continuous wave (CW) beam (called the probe) which is placed at the desired output wavelength was transmitted into the SOA simultaneously, and this CW would be modulated by the gain of the SOA, that is wavelength conversion by XGM.



Co-propagation scheme



Counter-propagation scheme

Figure 1-1: Schema of the co- and counter-propagation XGM

Both waves can be injected either co- or counter-propagating (see Fig.1-1). The XGM-based wavelength converters are very simple to realize. On the other hand, two disadvantages are associated with the XGM scheme. First, the input extinction ratio might significantly be degraded when the signal is wavelength up conversion. Secondly, the large amount of chirp makes the converted signal with transmission over standard-single mode fiber in particular at high bit rates a severe problem.

XPM-based wavelength converters rely on optically controlled refractive index change in a SOA. This originates from that the refractive index and the gain of the SOA are not independent, but they are related through the Kramers-Kronig relation (K-K relation). In other words, an amplitude modulated signal can also modulate the index of the SOA. The SOA's are situated in a Mach-Zehnder configuration in order to transfer the phase modulation into an amplitude modulated signal (see Fig.1-2). The advantage of this scheme is the low operation power needed as well as the ability to improve the signal quality of the converted signal with respect to extinction ratio and chirp.

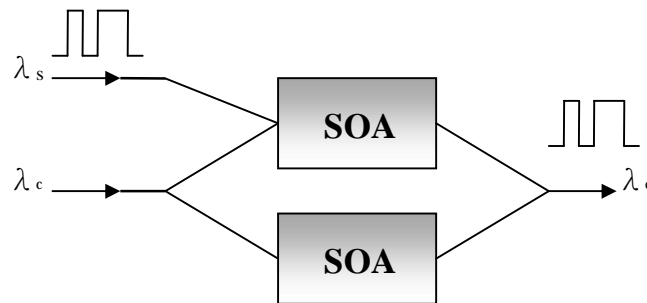


Figure 1-2: Schema of the XPM

Wavelength conversion using FWM in SOA's utilizes the high nonlinearity of SOA's, and this scheme is transparent to bit-rate and modulation format and is fully tunable over a wide range of wavelengths. Because of the high nonlinearity of the

SOA's, this process almost considers no problem about phase matching which is important for any nonlinear effect. However, the optical signal-to-noise ratio of FWM drops rapidly with increasing wavelength shifts, which limits its ability to provide large wavelength shifts. This is especially true for shifts to longer wavelengths.

Cross polarization modulation bases on nonlinear polarization rotation in a single SOA. Owing to the asymmetric waveguide geometry, the confinement factors, effective guide refractive indices and carrier distribution are not identical at the TE/TM orientations of a SOA, and this difference correlates monotonously with the input signal power through the SOA. When the input power turns high, the polarization of CW light is rotated and then the output power of CW could be modulate by a polarizer. There is a remarkable similarity between the characteristics of a wavelength converter based on nonlinear polarization rotation in a single SOA and XPM scheme. This similarity can be explained by the fact that cross polarization modulation scheme operate by interferometric principles, since the TE and TM modes that independently propagate through the SOA play the roles of the different light paths in the MZI. Unfortunately, the conversion efficiency for this scheme is not very high, and is very sensitive to polarization of CW light.

1.3 Structure of The Thesis

In chapter 2, the theory about nonlinearity of SOA's and dynamic SOA model are described in detail. The simulation model and the simulation result of wavelength conversion schemes are given in chapter 3. Chapter 4 shows some experiment results which include XGM, XPM, FWM, and cross polarization modulation schemes. Finally, conclusions are given in the chapter 5.

CHAPTER 2

BASIC CONCEPTS

2.1 Gain Spectrum and Rate Equations of SOA's

2.1.1 Gain model of SOA's

Considerable attention has focus on SOA's which are also called semiconductor laser amplifier and their potential use in optical communication systems both for optical fiber transmission and for optical data processing. SOA's provide high gain, with low power consumption and their single-mode waveguide structure makes them particularly suitable for use with single mode fiber. They can be used in both linear and nonlinear modes of operation and thereby there are many possible applications to optical systems [8].

Fig.2-1 is a schematic diagram of a SOA, which is based on the normal semiconductor laser structure, with active region width W , thickness d , and length L . The input and output laser facet reflectivities are denoted R_1 and R_2 , respectively. In the literature two types of amplifier are often distinguished, the Fabry-Perot (FP) amplifier and the traveling wave (TW) amplifier, both have the normal semiconductor laser structure, but differ in their facet reflectivities. The most promising candidate

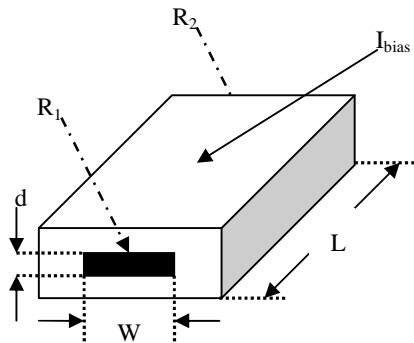


Figure 2-1: SOA schematic

for applications in optical systems is TW SOA in which the facet reflectivities of a semiconductor laser are reduced below 0.1 percent by the use of anti-reflection coatings. Anti-reflection coatings have the effect of increasing the amplifier bandwidth and make the transmission characteristics less dependent on fluctuations in bias current, temperature, and input signal polarization.

Amplification takes place in the active region of the semiconductor laser and the material gain coefficient per unit length g_m is generally assumed to have a peak value proportional to carrier density N , a cubic gain-wavelength characteristic, and a peak gain wavelength which is a function of the carrier density. Thus, the material gain is approximated by [9]:

$$g_m(N, I) = a(N - N_0) - g_1(I - I_p)^2 + g_2(I - I_p)^3 \quad (2-1)$$

where a_0 , g_1 , and g_2 are gain constants which are empirically determined in order to fit the experimentally measured SOA gain curve, N_0 is carrier density at transparency, and the gain peak wavelength I_p is given by:

$$I_p = I_0 - k(N - N_0) \quad (2-2)$$

where k is also empirically determined, and I_0 is the wavelength at transparency.

It generally treats a SOA as a two-level system, which is an approach suitable for gaseous and solid state amplifiers. It can be extended for SOA's if the active region is modeled as a collection of non-interacting two-level systems with transition energies extending over the whole range of the conduction and valence bands. If the input signal pulse width is assumed to be much larger than the intraband relaxation time which governs the dynamics of the induced polarization, the considerable simplification which neglects the intraband processes could be held. In general, the condition for simplification is typically held when signal pulse width is larger than 1

ps. In this approximation, the carrier density rate equation of SOA which medium response to the photon density S is described by [10]:

$$\frac{\partial N}{\partial t} = D\nabla^2 N + \frac{I}{qV} - \frac{N}{t_e} - \sum v_g \Gamma g_m S \quad (2-3)$$

where D is the diffusion coefficient, I is the injection current, q is the electron charge, V is the active volume, v_g is the group velocity, Γ is the confinement factor, and t_e is the carrier lifetime which is equal to :

$$t_e^{-1} = c_1 + c_2 N + c_3 N^2 \quad (2-4)$$

where c_1 , c_2 , and c_3 are the constants of nonradiative recombination rate, radiative recombination rate, and Auger recombination rate, respectively.

2.1.2 Pulse propagation equations in SOA's

The propagation of the electromagnetic field inside the amplifier is governed by the wave equation which comes from Maxwell's equations:

$$\nabla^2 \mathbf{E} - \frac{e}{c^2} \frac{\partial^2 \mathbf{E}}{\partial t^2} = 0 \quad (2-5)$$

where c is the velocity of light, and \mathbf{E} is the optical field. The dielectric constant e is given by

$$e = n_b^2 + c \quad (2-6)$$

where the background refractive index n_b is generally a function of the transverse coordinates x and y to account for the dielectric waveguide in SOA's. The susceptibility c represents the contribution of the charge carriers inside the active region of the amplifier and is a function of the carrier density N . The exact dependence of c on N is quite complicated as it depends on details of the band structure (among other things). A simple phenomenological model has been found

quite useful in the theory of semiconductor lasers [11]. In this model, c is assumed to depend on the material gain g_m linearly and is given by

$$c(N) = -\frac{\bar{n}c}{w_0}(a+i)g_m \quad (2-7)$$

where \bar{n} is the effective mode index, w_0 is photon frequency, and a is the chirp parameter or sometimes called the linewidth enhancement factor.

Equation (2-3) ~ (2-7) provide a general theoretical framework for the propagation of optical pulses in SOA's. In practice, it is necessary to make several simplifying approximations. We consider an ideal TW amplifier and assume that the active region dimensions are such that the amplifier supports a single waveguide mode. Assuming that the input light is linearly polarized and remains linearly polarized during propagation, the electric field the amplifier can be written as:

$$\mathbf{E}(x, y, z, t) = \hat{x} \frac{1}{2} \left\{ F(x, y) A(z, t) \cdot \exp[i(k_0 z - w_0 t)] + c.c. \right\} \quad (2-8)$$

where \hat{x} is the polarization unit vector, $F(x, y)$ is the waveguide-mode distribution, $k_0 = \bar{n}w_0/c$ is wave number, and $A(z, t)$ is the slowly-varying envelope associated with the optical pulse. If the equation (2-8) is substituted in (2-5), neglect the second derivatives of $A(z, t)$ with respect to z and t , and integrate over the transverse dimensions. It gives

$$\frac{\partial^2 F}{\partial x^2} + \frac{\partial^2 F}{\partial y^2} + (n_b^2 - \bar{n}^2) \frac{w_0^2}{c^2} F = 0 \quad (2-9)$$

$$\frac{\partial A}{\partial z} + \frac{1}{v_g} \frac{\partial A}{\partial t} = \frac{iw_0 \Gamma}{2\bar{n}c} cA - \frac{1}{2} a_{\text{int}} A \quad (2-10)$$

where $v_g = c/n_g$, the group index $n_g = \bar{n} + w_0(\partial\bar{n}/\partial w)$, and the confinement factor Γ is defined as:

$$\Gamma = \frac{\int_0^W \int_0^d |F(x, y)|^2 dx dy}{\int_{-\infty}^{\infty} \int_{-\infty}^{\infty} |F(x, y)|^2 dx dy} \quad (2-11)$$

The solution of (2-9) provides the transverse distribution $F(x, y)$ and the effective mode index \bar{n} . Equation (2-10) governs the evolution of the pulse amplitude along the amplifier length. The transverse effects are included through the confinement factor Γ . The last term in (2-10) takes into account the internal loss a_{int} experienced by the mode when $c=0$. The group velocity dispersion related to $\partial^2 \bar{n} / \partial \omega^2$ is neglected since its effect on pulse propagation is negligible for typical amplifier lengths (≤ 1 mm) and pulse widths (≥ 1 ps). It can be included by adding a term containing $\partial^2 A / \partial t^2$ on the left hand side of (2-10).

2.2 Wave Mixing in SOA's

2.2.1 Intraband processes in SOA's

Four wave mixing in active semiconductor waveguide has been studied quite extensively in recent years. In general, two optical fields, a strong pump at an angular frequency ω_0 and a weaker probe at ω_1 , can mix nonlinearly to produce a so-called conjugate signal at $\omega_2 = 2\omega_0 - \omega_1$. Thus, the beating of the pump and probe fields leads to modulation of various parameters of the medium at the beat frequency $\Omega = \omega_1 - \omega_0$. For detuning frequencies in the MHz-GHz range, modulation of the carrier density is very effective due to the relatively slow recovery of the carrier density determined by the carrier lifetime $t_e \sim 10^2$ ps. However, as detuning frequency exceed about 10 GHz, the intraband dynamics start to become important. The intraband processes affect the shape of the carrier distributions in k-space, but not the corresponding total carrier density. Since there are strong forces, carrier-carrier and carrier-phonon scattering, which tend to restore the distributions to equilibrium Fermi distributions, intraband contributions intrinsical have a small

efficiency. Conversely, the small intraband relaxation times imply that the bandwidths of intraband contributions will be very large.

There are two basically two different kinds of intraband dynamics that are local non-Fermian population pulsations and carrier-temperature pulsations. The two effects have the same origin as the spectral-hole burning (SHB) and carrier heating (CH). SHB arises due to the finite value of the intraband carrier-carrier scattering

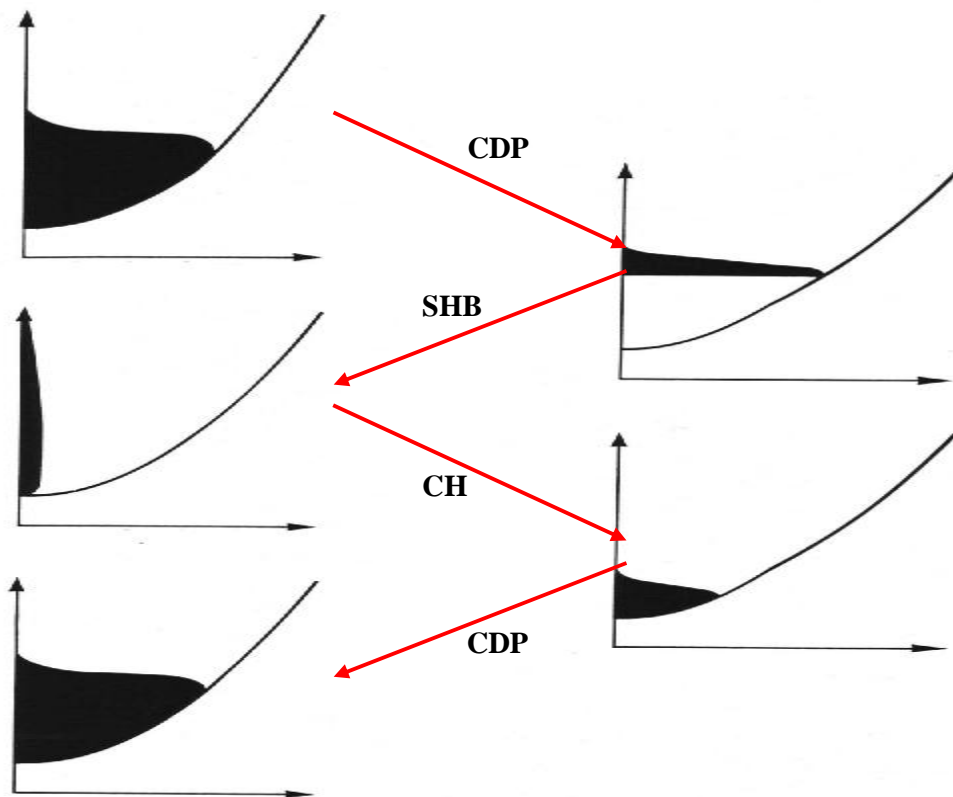


Figure 2-2: The inter- and intraband process in semiconductor.

time ($\sim 10fs$), which sets the time scale on which a quasi-equilibrium Fermi distribution is established among the carriers in a band. There are also processes that tend to increase the temperature of the carrier distributions beyond the lattice temperature. The main processes heating the carrier distributions are stimulated emission, since it involves the removal of cold-carriers close to the band edge, and

free-carrier absorption. The hot-carrier distributions relax to the lattice temperature by the emission of optical phonons with a characteristics time constant ($\sim 10^2$ fs). On the other hand, the interband process is called CDP (carrier density pulsations) for short. The processes, CDP, SHB, and CH, which dominate the FWM effect, are illustrated in fig. 2-2.

2.2.2 Equations for inter- and intraband processes

In order to calculate the polarization induced by an electromagnetic field in a semiconductor medium, the density-matrix formalism is used. The equations of motion for diagonal and off-diagonal elements of the density matrix r are [11]

$$\dot{r}_{c,k}(t) = -\frac{r_{c,k}(t) - f_{c,k}(t)}{t_{lc}} - \frac{r_{c,k}(t) - f_{c,k}^L(t)}{t_{hc}} - \frac{r_{c,k}(t) - f_{c,k}^{eq}}{t_e} - \frac{i}{\hbar} [d_k^* r_{cv,k}(t) - d_k r_{vc,k}(t)] E(z,t) + \Lambda_{c,k} \quad (2-12)$$

$$\dot{r}_{v,k}(t) = -\frac{r_{v,k}(t) - f_{v,k}(t)}{t_{lv}} - \frac{r_{v,k}(t) - f_{v,k}^L(t)}{t_{hv}} - \frac{r_{v,k}(t) - f_{v,k}^{eq}}{t_e} - \frac{i}{\hbar} [d_k^* r_{cv,k}(t) - d_k r_{vc,k}(t)] E(z,t) + \Lambda_{v,k} \quad (2-13)$$

$$\dot{r}_{cv,k}(t) = \left(-i\omega_k - \frac{1}{t_2} \right) r_{cv,k}(t) - \frac{i}{\hbar} d_k (r_{c,k}(t) + r_{v,k}(t) - 1) E(z,t) \quad (2-14)$$

$$r_{vc,k} = r_{cv,k}^* \quad (2-15)$$

These equations treat the semiconductor as being composed of an inhomogeneously broadened set of two-level systems which are labeled by the electron wavevector k . $r_{c,k}$ and $r_{v,k}$ denote the electron and hole occupation probabilities in conduction and valence band, respectively, for state k , and $r_{cv,k}$ is proportional to the corresponding atomic polarization. t_{lx} , and t_{hx} are time constants for intraband carrier-carrier and carrier-phonon scattering, respectively, and

$x = c$ or v . $f_{x,k}(t)$, $f_{x,k}^L(t)$, $f_{x,k}^{eq}$ are the Fermi distribution functions defined by instantaneous carrier density and by the carrier temperature, the lattice temperature, and equilibrium state, respectively. w_k and d_k are the transition frequency and dipole moment of the transition, respectively, and $\Lambda_{x,k}$ denotes pumping due to current injection. The first term on the right-hand side (RHS) of equation (2-12) and (2-13) describes the relaxation of the carriers to a Fermi distribution. The second term on the RHS of (2-12) and (2-13) describes equilibration of the carrier temperatures toward the lattice temperature due to electron-phonon collisions. The third term accounts for relaxation toward the thermal equilibrium distribution. Finally, the term proportional to $E(z,t)$ denotes stimulated emission and absorption.

The macroscopic polarization induced by the optical field $E(z,t)$ can be expressed as

$$P(t) = \frac{1}{V} \sum_k d_k (r_{cv,k} + r_{vc,k}) \quad (2-16)$$

Assume the pump and probe at w_0 and w_1 , respectively. In general case, nonlinearities in the semiconductor material lead to generation of fields at the combination frequency $w_l = w_0 + l\Omega$, where $l = \pm 1, \pm 2, \dots$. If the pump is much stronger than all other fields, only the pump saturates the medium. This allows us neglect fields at frequencies different from w_0 , w_1 , and conjugate $w_2 = w_0 - \Omega$. Thus the total electric field propagating in the SOA:

$$E(z,t) = E_o(z) \exp(-iw_0t) + E_1(z) \exp(-iw_1t) + E_2(z) \exp(-iw_2t) + c.c. \quad (2-17)$$

And the $P(z,t)$ induced by $E(z,t)$ is

$$P(z,t) = P_o(z) \exp(-iw_0t) + P_1(z) \exp(-iw_1t) + P_2(z) \exp(-iw_2t) + c.c. \quad (2-18)$$

In order to find the polarizations P_j , some assumptions are made:

$$r_{cv,k} = s_{k,0} \exp(-iw_0t) + s_{k,1} \exp(-iw_1t) + s_{k,2} \exp(-iw_2t) \quad (2-19)$$

$$r_{x,k} = \bar{r}_{x,k} + \mathcal{P}_{x,k} \exp(-i\Omega t) + \mathcal{P}_{x,k}^* \exp(i\Omega t) \quad (2-20)$$

$$N = \bar{N} + \Delta N \exp(-i\Omega t) + \Delta N^* \exp(i\Omega t) \quad (2-21)$$

$$T_x = \bar{T}_x + \Delta T_x \exp(-i\Omega t) + \Delta T_x^* \exp(i\Omega t) \quad (2-22)$$

Use equation (2-14), (2-16), (2-17), (2-19), and (2-20), and then

$$P_0 = \frac{1}{V} \sum_k \frac{d_k^2}{\mathbf{h}} \hat{c}_k(w_0) (\bar{r}_{c,k} + \bar{r}_{v,k} - 1) E_0 \quad (2-23)$$

$$P_1 = \frac{1}{V} \sum_k \frac{d_k^2}{\mathbf{h}} \hat{c}_k(w_1) [(\bar{r}_{c,k} + \bar{r}_{v,k} - 1) E_1 + (\mathcal{P}_{c,k} + \mathcal{P}_{v,k}) E_0] \quad (2-24)$$

$$P_2 = \frac{1}{V} \sum_k \frac{d_k^2}{\mathbf{h}} \hat{c}_k(w_1) [(\bar{r}_{c,k} + \bar{r}_{v,k} - 1) E_2 + (\mathcal{P}_{c,k}^* + \mathcal{P}_{v,k}^*) E_0] \quad (2-25)$$

Thus, the problem reduces to the determination of the population-inversion factors $(\bar{r}_{c,k} + \bar{r}_{v,k} - 1)$ and $(\mathcal{P}_{c,k} + \mathcal{P}_{v,k})$.

In order to solve $(\bar{r}_{c,k} + \bar{r}_{v,k} - 1)$ and $(\mathcal{P}_{c,k} + \mathcal{P}_{v,k})$, carrier density $N(t)$ and energy density U_x are defined as

$$N(t) = \frac{1}{V} \sum_k r_{x,k}(t) = \frac{1}{V} \sum_k f_{x,k}(t) = \frac{1}{V} \sum_k f_{x,k}^L(t) \quad (2-26)$$

$$U_x(t) = \frac{1}{V} \sum_k e_{x,k} r_{x,k}(t) \quad (2-27)$$

where $e_{x,k}$ is the carrier energy. Summing up (2-12), (2-13) over k and

multiplying by $e_{x,k}$ before summing, the rate equations become:

$$\frac{dN}{dt} = \frac{I}{eV} - \frac{N}{t_e} - \frac{i}{\mathbf{h}V} \sum_k d_k [r_{cv,k}(t) - r_{vc,k}(t)] \cdot E(z,t) \quad (2-28)$$

$$\begin{aligned} \frac{dU_x}{dt} = & \langle \mathbf{e}^p \rangle \frac{I}{eV} - \frac{U_x}{t_e} - \frac{U_x - U_x^L}{t_{hx}} + K_x \langle |E(z,t)|^2 \rangle \\ & - \frac{i}{\mathbf{h}V} \sum_k e_{x,k} d_k [r_{cv,k}(t) - r_{vc,k}(t)] \cdot E(z,t) \end{aligned} \quad (2-29)$$

where $I = e \sum_k \Lambda_{x,k}$ and $\langle \mathbf{e}_x^p \rangle = \frac{e}{I} \sum_k \mathbf{e}_{x,k} \Lambda_{x,k}$. The fourth term on the RHS of (2-29) represents the free-carrier absorption (FCA) and $K_x = e_0 \mathbf{h} h_g v_g \mathbf{s}_x N$, where e_0 , h , h_g , and \mathbf{s}_x are the vacuum permittivity, mode refractive index, group refractive index, and cross section for FCA.

Using equations (2-12)~(2-14), (2-19)~(2-25), and (2-28)~(2-29), assuming that $t_{1x} = t_1 \ll t_{hx} \ll t_e$, and considering the lowest order expansion, the polarizations become

$$P_0 = e_0 \bar{c}(w_0) E_0 \quad (2-30)$$

$$P_1 = e_0 \bar{c}(w_1) E_1 + e_0 \mathcal{C}(w_1; w_0, w_1) E_1 + e_0 \mathcal{C}(w_1; w_2, w_0) \frac{E_0^2}{|E_0|^2} E_2^* \quad (2-31)$$

$$P_2 = e_0 \bar{c}(w_2) E_2 + e_0 \mathcal{C}(w_2; w_0, w_2) E_2 + e_0 \mathcal{C}(w_2; w_1, w_0) \frac{E_0^2}{|E_0|^2} E_1^* \quad (2-32)$$

where $\bar{c}(w) = \frac{1}{e_0} \frac{1}{V} \sum_k \frac{d_k^2}{\mathbf{h}} \hat{c}_k(w) (\bar{r}_{c,k} + \bar{r}_{v,k} - 1)$, $\mathcal{C} = c^{(3)} = c_{CDP}^{(3)} + c_{CH}^{(3)} + c_{SHB}^{(3)}$, and $c_{CH}^{(3)} = c_{T_c}^{(3)} + c_{T_x}^{(3)}$.

$$c_{CDP}^{(3)}(w_i; w_i, w_j) = \frac{S_0}{\wp_i^N} \frac{ch}{w_i} \bar{g}(w_0) \frac{a_N(w_i) + i}{[i(w_i - w_j)t_1 + 1][i(w_i - w_j)t_e + 1 + S_0/\wp_i^N]} \quad (2-33)$$

$$c_{T_x}^{(3)}(w_i; w_i, w_j) = \frac{S_0}{\wp_i^{T_x}} \frac{ch}{w_i} \left[\bar{g}(w_0) + \mathbf{s}_x \bar{N} \frac{\mathbf{h} w_0}{m_x - e_{x0}} \right] \frac{a_{T_x}(w_i) + i}{[i(w_i - w_j)t_1 + 1][i(w_i - w_j)t_{hx} + 1]} \quad (2-34)$$

$$c_{SHB}^{(3)}(w_i; w_i, w_j) = \frac{S_0}{\wp^{SHB}} \frac{1}{(w_i - w_j)t_1 + 1} \frac{1}{e_0} \frac{1}{V} \sum_k \left\{ \frac{d_k^4}{\mathbf{h} d_0^2} \hat{c}(w_i) (\bar{f}_{c,k} + \bar{f}_{v,k} - 1) \frac{-i}{2t_2} [\hat{c}_k(w_j) - \hat{c}_k^*(w_i)] \right\} \quad (2-35)$$

where $\bar{g}(w) = -\frac{w}{ch} \text{Im}[\bar{c}(w)]$ is the saturated gain, and $S_0 = \frac{2e_0 h h_g |E_0|^2}{h w_0}$. The

linewidth enhancement factors and the saturation photon densities are:

$$a_N(w) = \left(\frac{\partial \text{Re}[\bar{c}(w)]}{\partial N} \right) / \left(\frac{\partial \text{Im}[\bar{c}(w)]}{\partial N} \right) \quad (2-36)$$


$$a_{T_x}(w) = \left(\frac{\partial \text{Re}[\bar{c}(w)]}{\partial T_x} \right) / \left(\frac{\partial \text{Im}[\bar{c}(w)]}{\partial T_x} \right) \quad (2-37)$$

$$\frac{1}{\wp_l^N} = v_g t_1 \frac{\partial \bar{g}(w_l)}{\partial N} \quad (2-38)$$

$$\frac{1}{\wp_l^{T_x}} = -v_g t_{hx} \frac{\partial \bar{g}(w_l)}{\partial T_x} (m_x - e_{x0}) h_x^{-1} \quad (2-39)$$

$$\frac{1}{\wp^{SHB}} = \frac{2t_1 t_2 d_0^2 w_0}{e_0 h h_g h} \quad (2-40)$$

Furthermore, $m_x = \frac{\partial U_x}{\partial N}$ and $h_x = \frac{\partial U_x}{\partial T_x}$



2.3 Interference Between TM and TE Modes in SOA's

In SOA's, the transverse electric (TE) and transverse magnetic (TM) effective indices at position z in the active region can be given as

$$n_{TM/TE}(z) = n_{oTM/TE} + \Gamma_{TM/TE} \cdot N(z) \cdot \left(\frac{\partial n}{\partial N} \right)_{TM/TE} \quad (2-41)$$

where $n_{oTM/TE}$ is the effective refractive index of the waveguide for zero-free carrier density, $\Gamma_{TM/TE}$ is the confinement factor, and $\left(\frac{\partial n}{\partial N} \right)_{TM/TE}$ is the rate of change of active layer refractive index for the TM and TE mode, respectively. Because the TE/TM are not symmetric, the confinement factors are not equal as well as the unperturbed effective refractive indices of SOA's. In polarization independent

SOA's, the reasonable PDG is technologically achievable, but it is impossible to completely constrain this birefringence. The birefringence of SOA's will vary with different change of TE/TM gains and indices, when the carrier density drops with large input signal power. That is, there are two effects which influence the state of polarization (SOP) simultaneously.

Fig. 2-3 illustrates the interferometric arrangement between the TM and TE modes. Because the TM and TE modes are independently propagating through the SOA's, they could play the roles of the different paths in the Mach-Zehnder interferometer. In order to achieve a Mach-Zehnder interferometer by only using one SOA and to make TM mode interfered with TE mode, a polarizer is needed. As shown in fig. 2-3, when the polarizer is set at 45^o, assuming that the TM and TE modes are in-phase, the projection parts of TM and TE modes which align with and could pass through the polarizer are in the opposite direction. That is, they will destructively interfere with each other, and then there is almost no power coming out from the polarizer. On the other hand, if the TM and TE modes are out-phase, the projection parts of them will constructively interfere with each other. Therefore, the

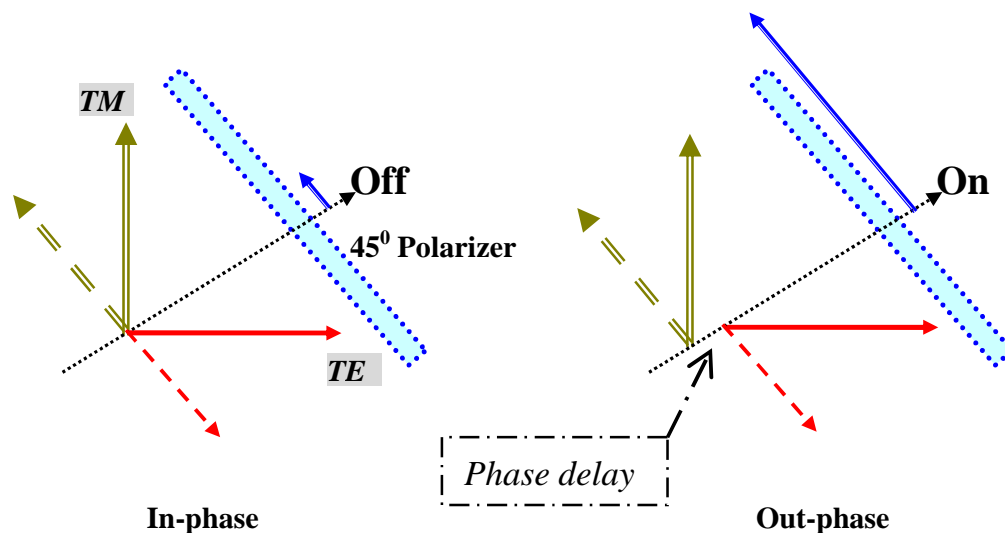


Figure 2-3: The schemata of interference between TE and TM mode

polarizer can not close the output power. However, if the polarizer is tunable and set it at -45° , then the on-off condition of the SOP will be reversed. Since the indices of TM and TE modes in SOA's could be adjusted by the signal power, the interference between TM and TE modes could be used as mechanism of a wavelength converter.



CHAPTER 3

SIMULATIONS

3.1 Simulation Method for Wavelength Conversion

A large signal analysis for SOA's is performed using the time-dependent transfer matrix method (TMM) to calculate converted optical pulse waveforms and chirp in SOA's by self-consistently solving the pulse propagation and rate equations. The time-dependent TMM has been proposed for the purpose of characterizing the multi-electrode distributed feedback (DFB) laser [13]. In order to apply this method to SOA's, we have modified the propagating part of the transfer matrix using the equation (2-10) that describes the propagation of pulses in SOA's. Here, the internal loss a_{int} in SOA's is combined with material gain and confinement factor as the net gain g which is given by [14]

$$g = \Gamma(g_m - a_a) - (1 - \Gamma)a_c - a_{scat} \quad (3-1)$$

where a_a , a_c , and a_{scat} are constants of the loss in active layer, the loss in cladding, and the scattering loss, respectively. Then, equation (2-10) could be re-written as

$$\frac{\partial A(z,t)}{\partial z} + \frac{1}{v_g} \frac{\partial A(z,t)}{\partial t} = -\frac{i}{2} \mathbf{a} \Gamma g_m A(z,t) + \frac{1}{2} g A(z,t) \quad (3-2)$$

The basis of the TMM is to divide a laser structure longitudinally into a number of sections where the structural and material parameters are assumed to be homogeneous throughout each section. However, these parameters may vary between sections, allowing longitudinal inhomogeneities such as those produced by longitudinal spatial hole burning and nonlinear gain to be incorporated into the model. Each of the sections is characterized by a transfer matrix which modifies the forward and backward traveling waves as they propagate through the section. The use of the

TMM here is different from that in the steady-state model where the objective was to obtain the overall transfer matrix for the structure (given by the product of the section transfer matrices) from which the oscillation characteristics were determined. However, in this particular application, the emphasis is on describing the operation of the individual sections themselves where incrementing the model in time involves updating the traveling-wave amplitudes as the pass through a section.

In the conventional form, the transfer matrix $[\mathbf{T}_i]$ of a typical section i expresses the following relationship:

$$\begin{bmatrix} A_{i+1} \\ B_{i+1} \end{bmatrix} = [\mathbf{T}_i] \begin{bmatrix} A_i \\ B_i \end{bmatrix} \quad (3-3)$$

where it relates the amplitudes of the two counter-propagating waves A and B on either side of the section. Note that in this formulation, steady-state operation has implicitly been assumed. In order to develop a time-dependent implementation of the TMM, a typical section i at a time t described by the transfer matrix $[\mathbf{T}_i(t)]$ was considered. In fig. 3-1, impinging on the section are the forward and backward traveling waves $A_i(t)$ and $B_{i+1}(t)$, respectively. Note that the two waves are on

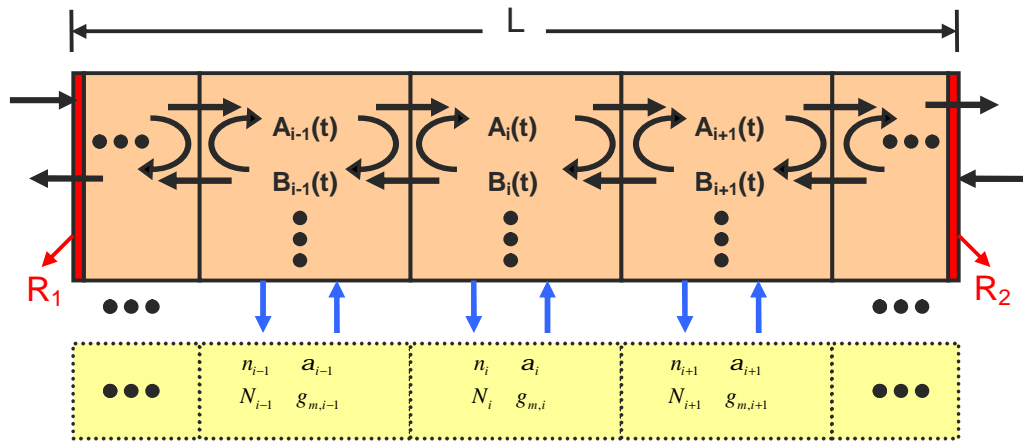


Figure 3-1: Schematic of the TMM-based SOA model

opposite sides of the section. After a time Δt which is corresponding to the section transit time, the two waves emerge at their respective opposite sides with updated amplitudes $A_i(t + \Delta t)$ and $B_{i+1}(t + \Delta t)$. Assuming that $[\mathbf{T}_i(t)]$ remains unchanged over the interval t to $t + \Delta t$, equation (3-3) can be re-written as

$$\begin{aligned} \begin{bmatrix} A_{i+1}(t + \Delta t) \\ B_{i+1}(t) \end{bmatrix} &= [\mathbf{T}_i(t)] \begin{bmatrix} A_i(t) \\ B_i(t + \Delta t) \end{bmatrix} \\ &= \begin{bmatrix} T_{i11}(t) & T_{i12}(t) \\ T_{i21}(t) & T_{i22}(t) \end{bmatrix} \begin{bmatrix} A_i(t) \\ B_i(t + \Delta t) \end{bmatrix} \end{aligned} \quad (3-4)$$

Rearranging these equations produces expressions for the updated amplitudes in terms of the old wave amplitude and the transfer matrix elements:

$$\begin{bmatrix} A_{i+1}(t + \Delta t) \\ B_i(t + \Delta t) \end{bmatrix} = \begin{bmatrix} T_{i11}(t) - \frac{T_{i12}(t)T_{i21}(t)}{T_{i22}(t)} & \frac{T_{i12}(t)}{T_{i22}(t)} \\ \frac{T_{i21}(t)}{T_{i22}(t)} & \frac{1}{T_{i22}(t)} \end{bmatrix} \begin{bmatrix} A_i(t) \\ B_{i+1}(t) \end{bmatrix} \quad (3-5)$$

Equation (3-5) form the basis of the TMM-based dynamic model where it is assumed that the temporal variations in $[\mathbf{T}_i(t)]$. At each time increment, the traveling-waves have advanced along the structure by one section, with their amplitudes at the output of each section being updated by the transfer matrix for the section. Essentially, the TMM is employed here to follow the growth and decay of the two traveling waves A and B as they propagate through the structure.

The carrier density equation (2-3) can also be simplified by noting that the width W and the thickness d of the active region are generally smaller while the amplifier length is much larger than the diffusion length. Since the carrier density is nearly uniform along the transverse dimensions, an average value can be used, to a good approximation, and neglect carrier diffusion. To account for the interaction between carrier density N and photon density S with the TMM method, the SOA

was divided into a number of small sections. Thereby, the rate equation (2-3) would be re-written as

$$\frac{\partial N_i}{\partial t} = \frac{I}{qV} - N_i (c_1 + c_2 N_i + c_3 N_i^2) - \sum v_g \Gamma g_{m,i} S_i \quad (3-6)$$

where the photon density S_i in (3-6) and the pulse envelope A_i (and B_i) in (3-2) are related through

$$S_i = \frac{|A_i|^2 + |A_{i+1}|^2 + |B_i|^2 + |B_{i+1}|^2}{2v_g \hbar \omega_o W d} \quad (3-7)$$

Clearly, S_i in (3-7) is average value in a section.

On the other hand, in order to describe the spectrum hole burning of material gain, the equation (2-1) must be modified empirically as

$$g_{m,i}(N_i, I) = \frac{a(N_i - N_0) - g_1(I - I_{p,i})^2 + g_2(I - I_{p,i})^3}{1 + \mathcal{G} \sum S_i} \quad (3-8)$$

where \mathcal{G} is the gain compression factor.

The chirp parameter a for each small section is considered since the parameter is directly related to frequency chirping due to the self-phase modulation (SPM) and XPM in SOA's.

$$a_i(N_i, I) = -\frac{4p}{I} \frac{dn/dN}{dg/dN} \quad (3-8)$$

This equation could be calculated from the variation of gain using (3-8) and was found to lie in the range of 2-12.

In the simulation, the transfer matrix elements T_{imm} are obtained from n_i , N_i , $g_{m,i}$, and a_i at time t illustrated in fig. 3-1. As mentioned before, every section is seen as homogeneous waveguide. Hence, the transfer matrix in this waveguide could be represented as

$$[\mathbf{T}_{HW}] = \begin{bmatrix} e^{g \cdot \Delta L} & 0 \\ 0 & e^{-g \cdot \Delta L} \end{bmatrix} \quad (3-9)$$

And for a refractive index step from n_1 to n_2 , the transfer matrix of the interface is given by

$$[\mathbf{T}_{IS}] = \begin{bmatrix} \frac{n_2 + n_1}{2\sqrt{n_1 n_2}} & \frac{n_2 - n_1}{2\sqrt{n_1 n_2}} \\ \frac{n_2 - n_1}{2\sqrt{n_1 n_2}} & \frac{n_2 + n_1}{2\sqrt{n_1 n_2}} \end{bmatrix} \quad (3-9)$$

where g is the propagation constant in homogeneous waveguide. n_1 and n_2 are refractive indices of neighbor sections. Two kinds of the transfer matrices are illustrated in fig. 3-2.

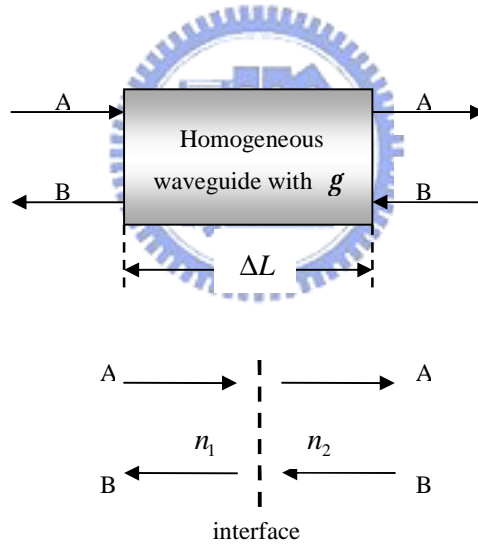


Figure 3-2: Schematic of transfer matrices

In the simulation using TMM method, not only the amplitude information could be calculated, but also the phase information. That is, the chirp of the converted signal could be calculated by differentiating its phase with respect to time in the following equation:

$$chirp = -\frac{1}{2p} \frac{df}{dt} \quad (3-9)$$

The parameters used in the simulation are summarized in Table 3-1.

<i>Symbol</i>	<i>Description</i>	<i>Value</i>	<i>Unit</i>
Γ	Confinement factor	0.3	
L	SOA length	1×10^{-3}	m
V	Active layer volume	1.5×10^{-16}	m^3
c_1	Recombination rate constants	1×10^8	s^{-1}
c_2		2.5×10^{-17}	$m^3 s^{-1}$
c_3		9.4×10^{-41}	$m^6 s^{-1}$
a	Material gain constants	2.5×10^{-20}	m^2
g_1		7.4×10^{18}	m^{-3}
g_2		3.155×10^{25}	m^{-4}
k		3×10^{-32}	m^4
N_0	Carrier density at transparency	1.1×10^{24}	m^{-3}
I_0	Wavelength at transparency	1.605×10^{-6}	m
v_g	Group velocity	7.5×10^7	ms^{-1}
\mathcal{E}	Nonlinear gain compression	1.3×10^{-23}	m^3
dn/dN	Differential refractive index	-1.2×10^{-26}	m^3
a_a	Loss in active layer	1.4×10^4	m^{-1}
a_c	Loss in cladding	2×10^3	m^{-1}
a_{scat}	Scattering loss	1×10^2	m^{-1}

Table 3-1: Device Parameters in SOA's

3.2 Simulation Results And Discussions of XGM

3.2.1 Overshoot and chirp of the converted signal

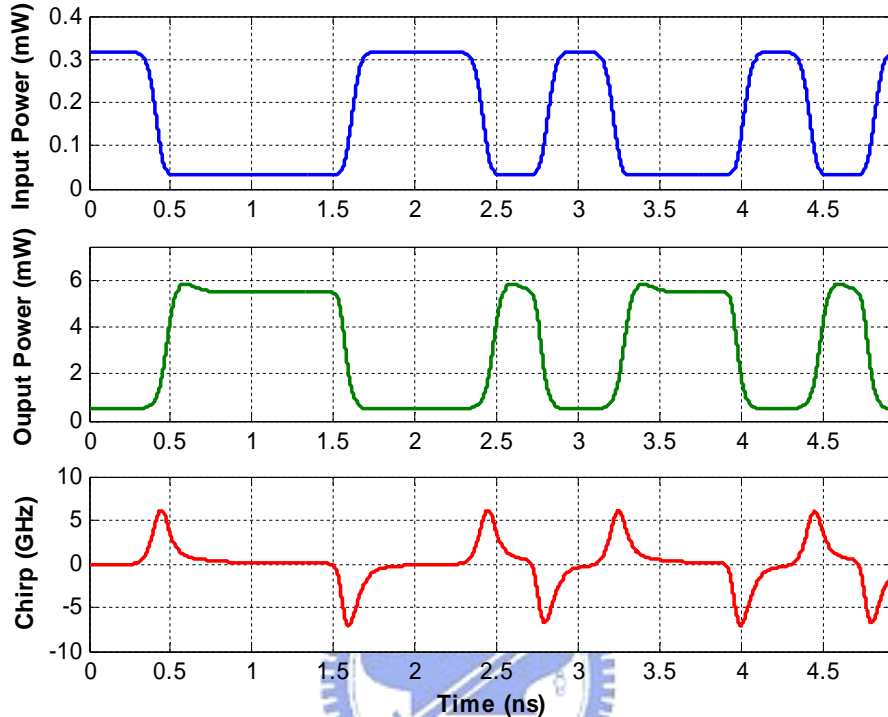


Figure 3-3: Input signals pattern (upper), converted signals pattern (middle), and frequency chirp (lower) using XGM method.

In fig. 3-3, the results of wavelength conversion with co-propagation XGM scheme were shown. Here the super Gaussian pulses ($m=3$) were investigated to simulate more realistic pulse shapes. The facet power reflectivity R , an input signal wavelength I_s , a CW wavelength I_c , and input CW power were 0%, 1550 nm, 1535 nm, and -15 dBm, respectively. Clearly, the converted signal compared with the input signal is negative logical. In the case of chirp, the output pulse undergoes a blue shift (positive chirp) during the rising edge and a red shift (negative chirp) during the falling edge. Because the rise time is longer than the fall time, negative peak chirp is larger than positive peak chirp. Thus, converted signals have

positive chirp which causes pulse broadening when the converted signal is transmitted through the standard single-mode fiber.

The wavelength converted signal undergoes overshoot on the rising edge and a little undershoot on the falling edge. These are caused by the fact that the response of carrier density is slower than the variation of optical pulse. In other words, the carrier lifetime t_e is significantly larger than the photon, thus the front end of the signal experiences unsaturated gain through the SOA, while gain saturation limits the gain experienced by the rest of the pulse. This growing overshoot in photon density causes an increasingly faster depletion of carrier density or gain of the SOA and results in further sharpening of the signal spike and faster depletion of the probe power. On the falling edge of the pulse, a similar situation occurs in that the saturated gain overshoots during recovering to its unsaturated value when the signal

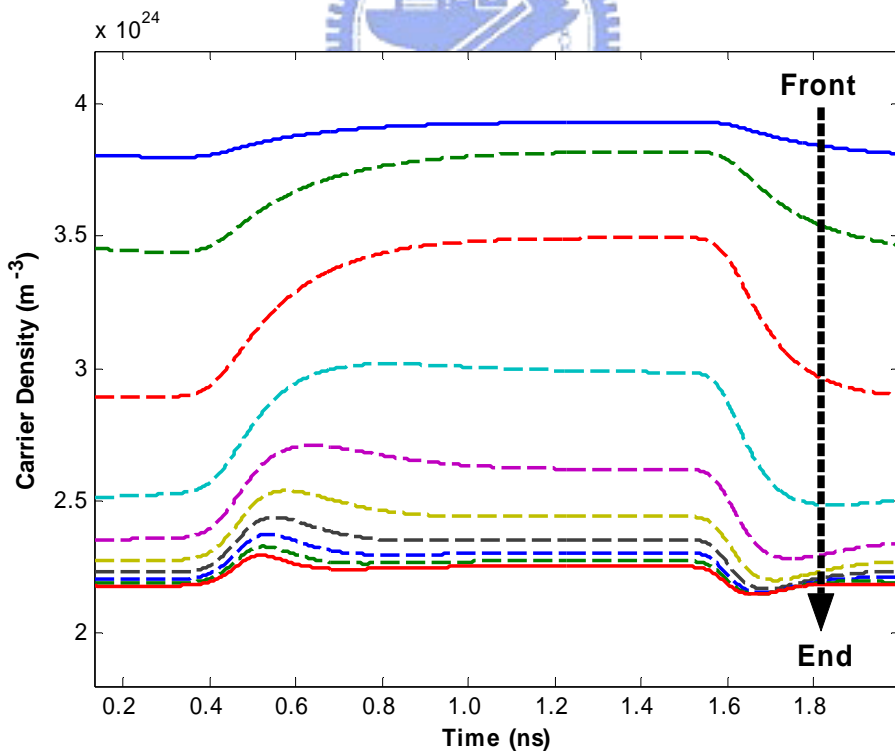


Figure 3-4: The variation of carrier density from the front to the end part of a SOA.

power is absent. This gain overshoot causes the sharpening of the probe and thus reduction of the associated rising time. The net effect is faster conversion as the pulse propagation through the amplifier and it could be observed from the variation of carrier density in different parts of the SOA in fig. 3-4. This result also explains that the conversion bandwidth is larger when longer the length of a SOA is.

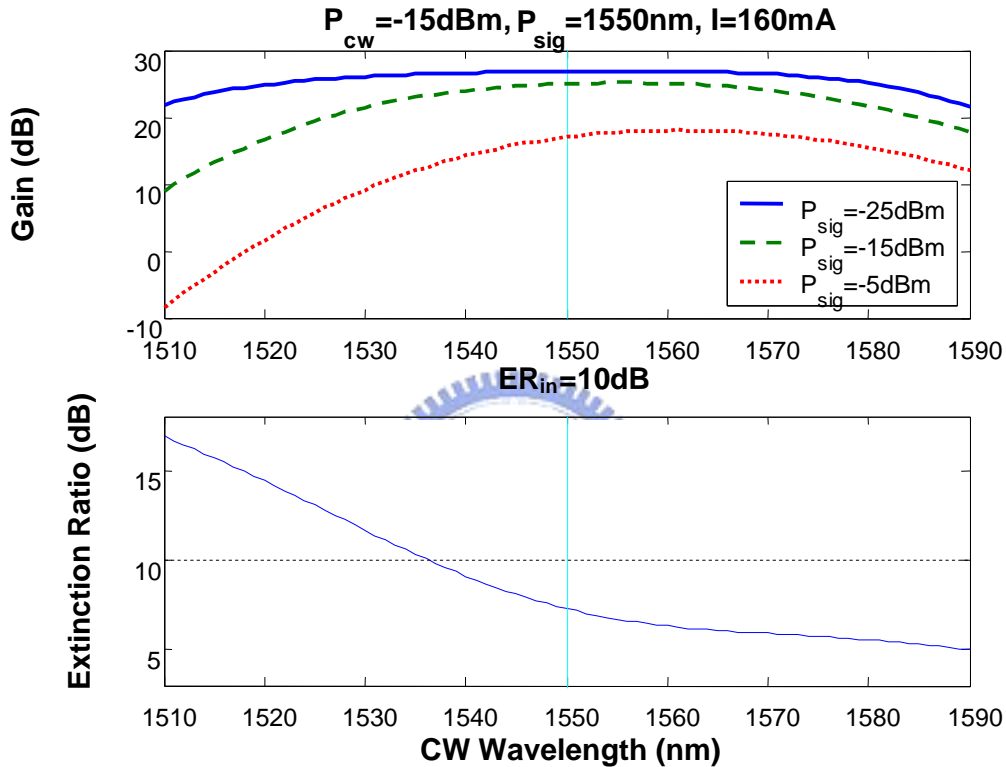


Figure 3-5: Gain spectra for different signal powers (upper), and the ER of converted signal obtained by subtracting the -5 and -15 dBm gain spectra.

In SOA's, the gain peak will shift to shorter wavelength with higher injection current. Namely, the photon with higher energy could get the largest gain. Because the carriers in the conduction band must obey the Fermi-distribution in steady-state, the energy level which the most carriers exist becoming higher as the number of total carriers is getting more. Similarly, when carriers deplete due to large power of input signal pulse, not only the gain of a SOA decreases but also the

gain peak shifts to longer wavelength. The phenomenon is illustrated in fig. 3-5 (upper).

The lower illustration of fig. 3-5 shows the extinction ratio (ER) of converted signal which is a function of CW wavelength. It should notice that this ER is static, not dynamic, while the ER is obtained by subtracted the steady gain curve with different input signal power. From the figure, one drawback of XGM scheme could be known that the ER degradation especially in case of up-wavelength conversion. The contour plot of ER for the signal and CW wavelength is shown in fig. 3-6, in which the red line represents the same CW and signal wavelength. In other words, the triangular region above the dashed line express the up-wavelength conversion, and oppositely the region below the dashed line express the down-wavelength conversion. Clearly, down conversion might lead to a high ER, as shown in fig. 3-6

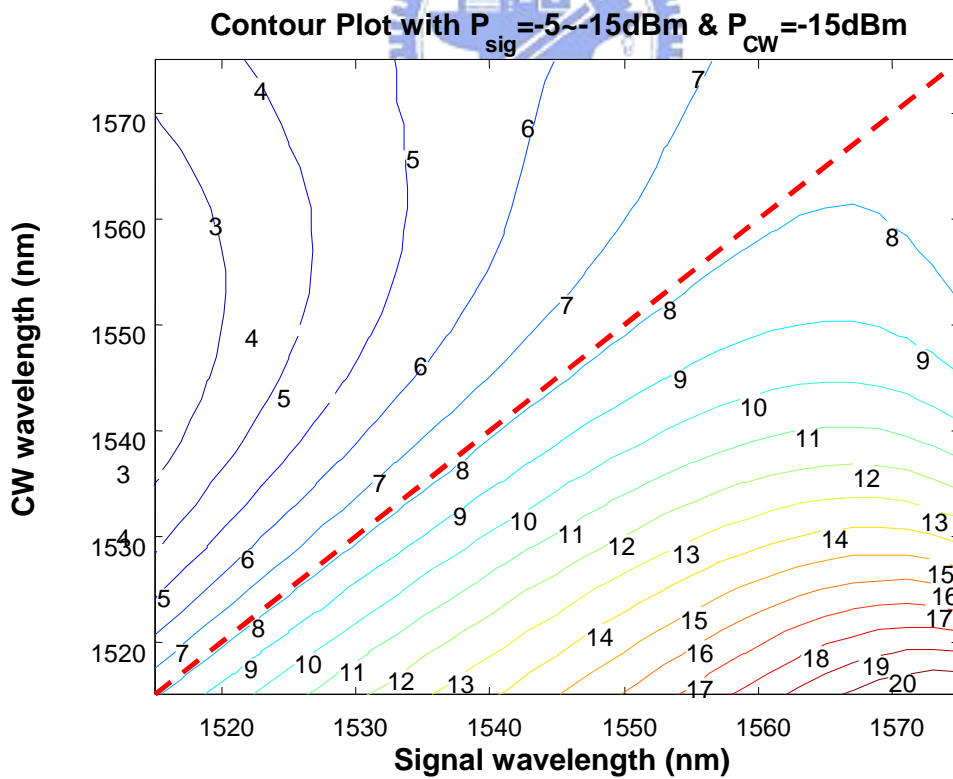


Figure 3-6: Contour plot of output ER with different signal and CW wavelength

In fig. 3-7, there are solid lines and dashed line which represent the peak chirp and ER of the converted signal as a function of average input signal power, respectively. The ER of the converted signal is increasing as the average input signal power is rising. At the same time, no matter positive or negative peak chirps are increasing like the ER vary. Assume that the bit-rate of input signal is smaller the bandwidth of SOA's, and the larger ER means that the huger the carrier depletion is. Through equation (2-7), it could be known that carrier depletion will induce variation of index. Then, the phase of the converted signal rapidly changes. Namely, the frequency chirping defined as equation (3-9) will be enlarged by increasing ER.

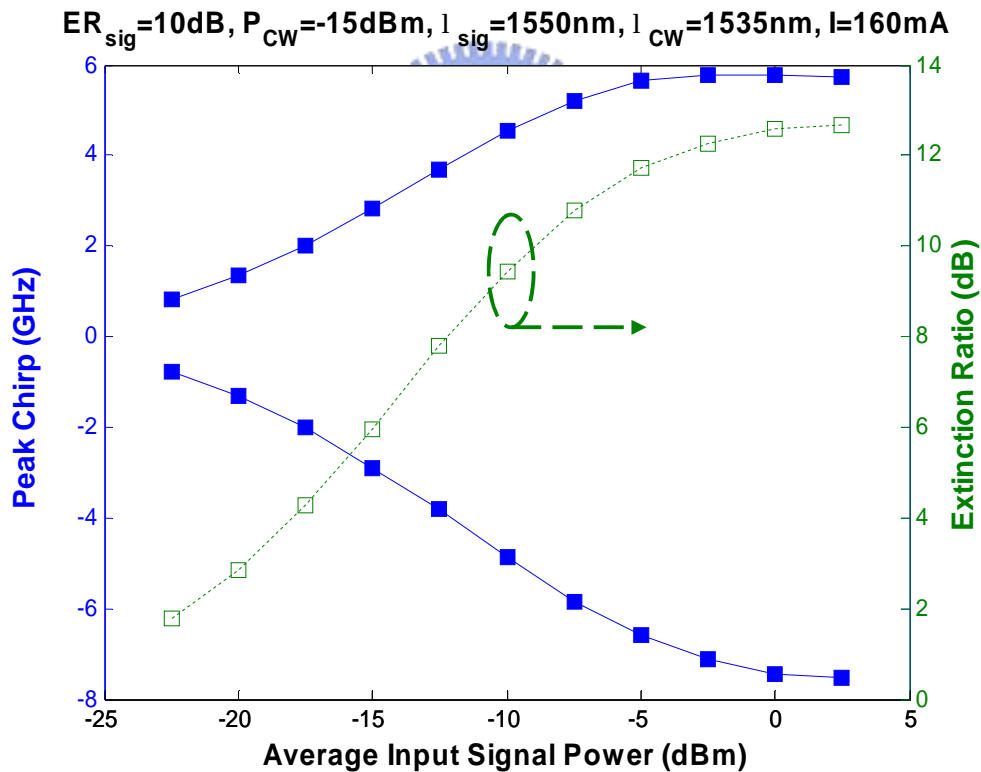


Figure 3-7: Peak Chirp (solid lines) and the extinction ratio (dashed line) of converted signals using XGM scheme.

3.2.2 Modulation bandwidth for XGM

When bit-rate of the input signal increases, the response of carriers may not follow the variation of the input signal. The performance of the converted signal may degrade. Fig. 3-8 shows the wavelength conversion of 10 Gbps signal, in which the pattern effect is significant, and the chirp become very serious due to the phase of the converted signal varying in a very short time interval.

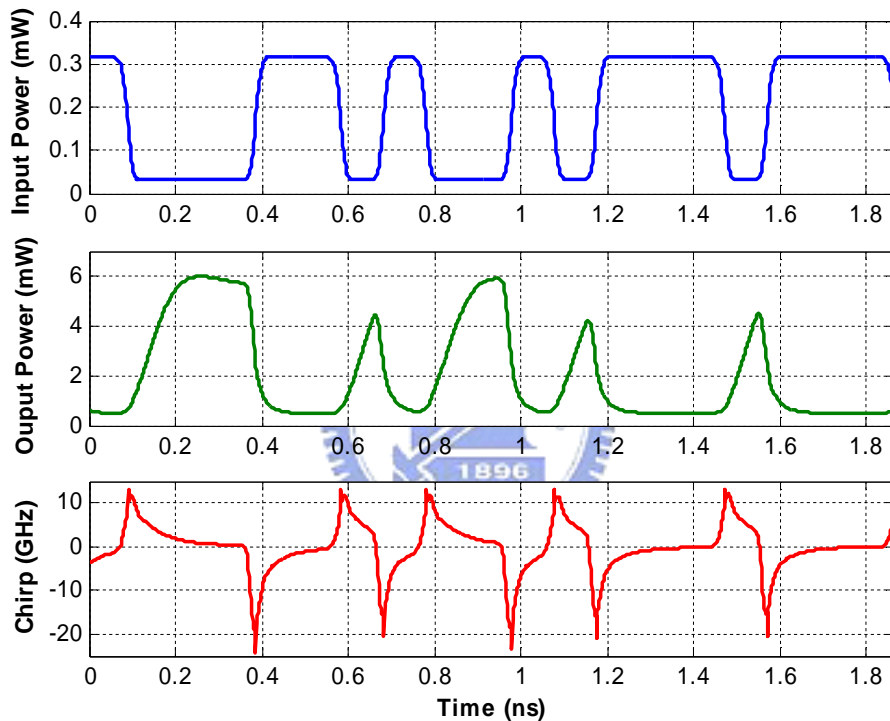


Figure 3-8: Wavelength conversion with 10 Gbps input signal by XGM

Although the small signal model has used to predict the bandwidth of co-propagation XGM scheme [15], it cannot analyze frequency chirping and the extinction ratio for large signal modulation. Here, the bandwidth of XGM is investigated using the eye opening ratio (EOR) which is defined as the power ratio between the minimum level of mark and the maximum level of space. Fig. 3-9 shows the peak chirp and the modulation bandwidth in terms of EOR which drops as

a function of data rate. The modulation bandwidth is improved by increasing the cavity length, since the longer the cavity is, the stronger the modulation effect by gain depletion is. This effect could also be seen in fig. 3-4. However, more gain

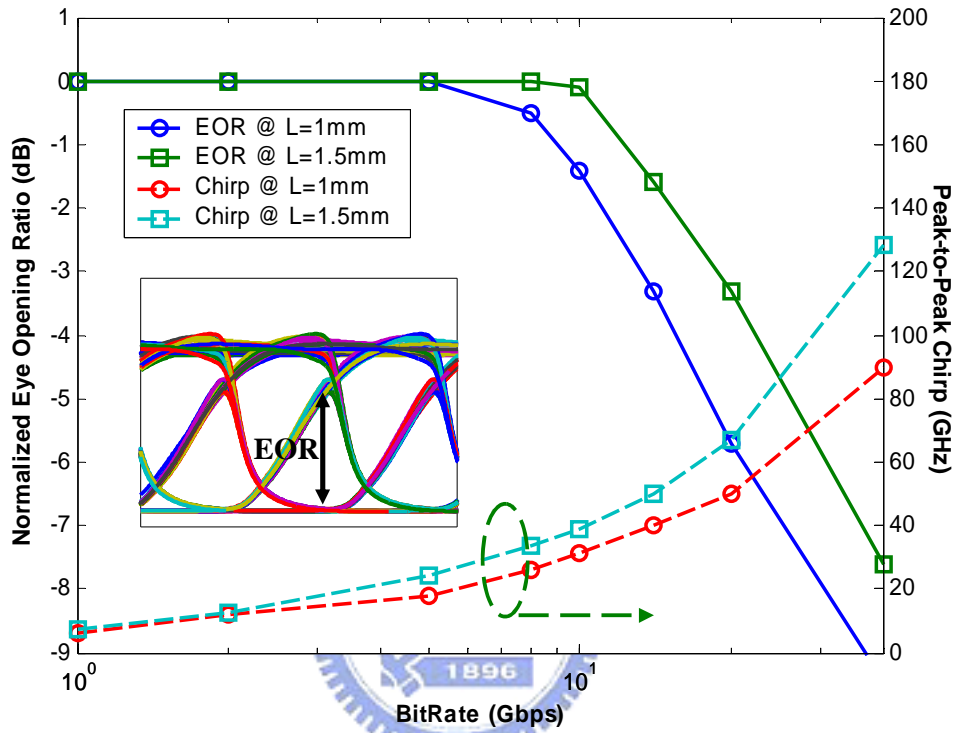


Figure 3-9: EOR and peak-to-peak chirp as a function of the data rate for different cavity length.

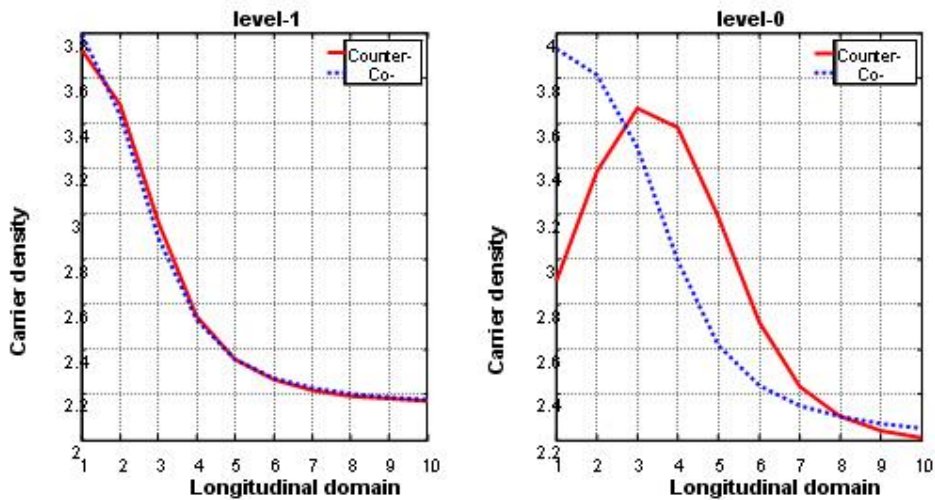


Figure 3-10: Carrier distribution in longitudinal direction as level-1 signal input (left) and level-0 signal input (right)

modulation will also induce more chirp due to larger varying of index simultaneously.

As mentioned, the input signal and CW can propagate either co- or counter-directional. For counter-propagation of the signal and the CW, the carrier density which is illustrated in fig. 3-10 will be lower in the part of the SOA where the CW enters since the amplified input signal, coming from the opposite direction, causes a strong saturation and therefore a higher noise figure than the co-directional case.

However, the counter-propagation of the signal and the CW cause timing jitter as predicted by simulation in fig. 3-11. The jitter results from the power dependent

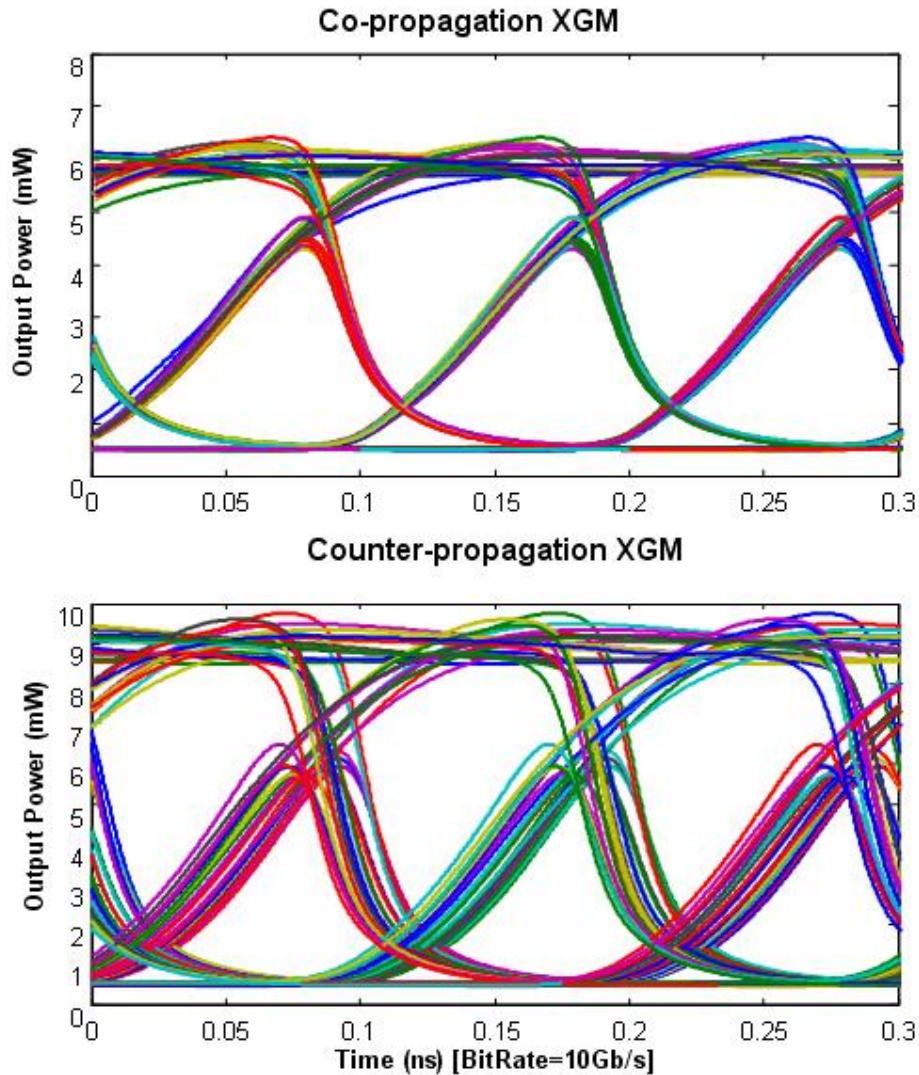


Figure 3-11: Eye diagrams of XGM in co- and counter-propagation configurations

distribution of the carriers in the SOA and is therefore pattern dependent. From the carrier distribution illustrated in fig. 3-10 in which the carrier density in the SOA is given for both a low signal input power (level-0) and a high signal input power (level-1). For the high input signal power, the signal determines the carrier distribution because more carriers are depleted as the signal is amplified. That is why the curves for co- and counter-propagation at level-1 look the same. In contrast, at level-0, the input signal power no longer dominates the carrier distribution that the CW is also important for. Due to the propagation time this movement of the gain distribution in the longitudinal direction of the SOA corresponds to a movement in time for the converted signal depending on the bit pattern. The result is that the converted signal will fluctuate as shown in fig. 3-11.

Besides the timing jitter, counter-propagation can suffer from speed limitations

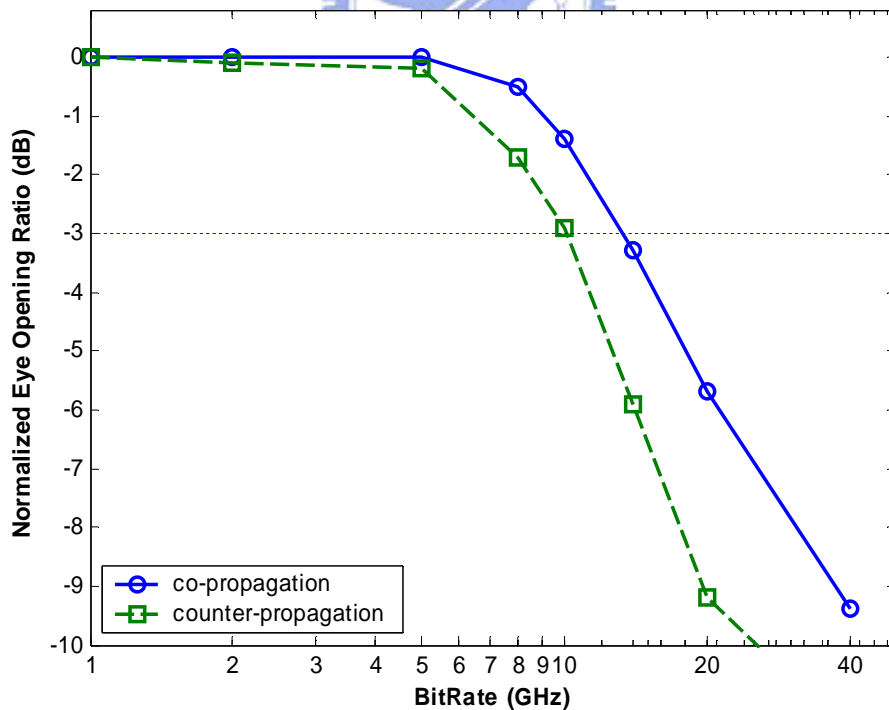


Figure 3-12: EOR of converted signal as a function of the data rate in co- and counter-propagation configurations.

since the input signal and the CW are no longer traveling together in the SOA. This is illustrated in fig. 3-12, which shows the modulation bandwidth by normalized EOR of XGM scheme in both co- and counter-propagation configurations. This is due to large, slow changes in the carrier distribution illustrated in fig. 3-10 along the amplifier cavity in counter-propagation configuration.

3.3 Simulation Results And Discussions of XPM

3.3.1 Operation points of XPM

It was noted in the discussion of XGM wavelength conversions that accompanying the gain modulation with carrier density change is a modulation of the refractive index of the SOA. This XPM can be utilized to good effect in interferometric arrangements to obtain wavelength conversion devices with significant advantages over those relying on XGM alone. The effect which phase is

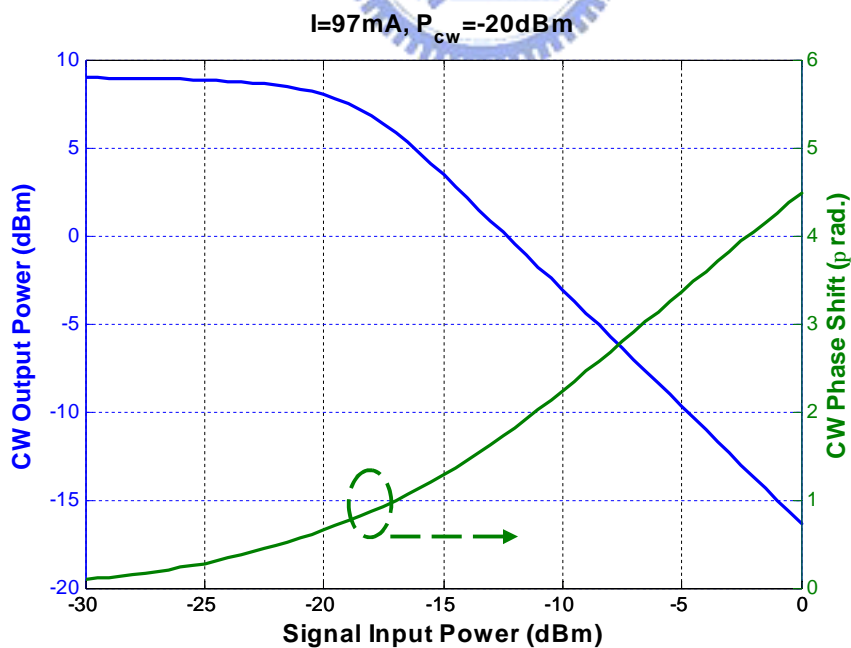


Figure 3-13: The phase shift with the gain saturation as a function of signal input power

modulated as gain depletion is simulated and illustrated in fig. 3-13. In such devices the CW light is split into two paths which contain SOA's, and a relative phase shift is induced by the optical switching signal entering one of the SOA's which is called the "phase SOA" and is saturated, whereas the other one is the "reference SOA". When the light is recombined, constructive or destructive interference will occur depending on the phase difference between the two paths. The unperturbed state of the interferometer can be set up for constructive or destructive interference so that injection of the input signal causes either a decrease or increase, respectively, in the wavelength converted signal. The state of the interferometer is typically set by adjusting the injection current in the two SOA's. Thus, one advantage to note for XPM wavelength converters is the choice between inverting or non-inverting operation. Fig. 3-14 shows that transfer function of the CW as a function of the phase current. In the figure, the solid line and the dashed line represent two different power levels of the static input signal, -16.5 dBm and -23.5 dBm, respectively. If

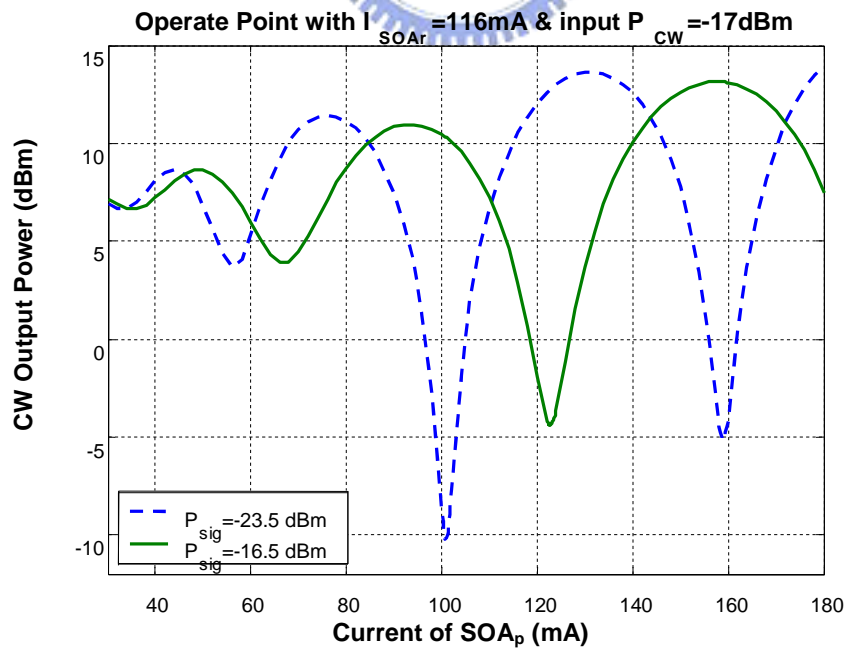


Figure 3-14: Transfer function of XPM wavelength converter by changing phase current

amplitude modulated signal is on-off keying (OOK) between -16.5 and -23.5 dBm, the best ER of output converted signal will be the power difference between solid line and dashed line. Then, there might be negative and positive ER, such as 120 mA and 160 mA current injected into the phase SOA, respectively. In other words, negative ER means the inverted conversion like the conversion in XGM scheme, and, in contrast, the positive ER is the condition of non-inverted conversion. The simulation of non-inverted and inverted converted signal by XPM is showed in fig. 3-15, in which simulation parameters are the same with fig. 3-14, and the injection

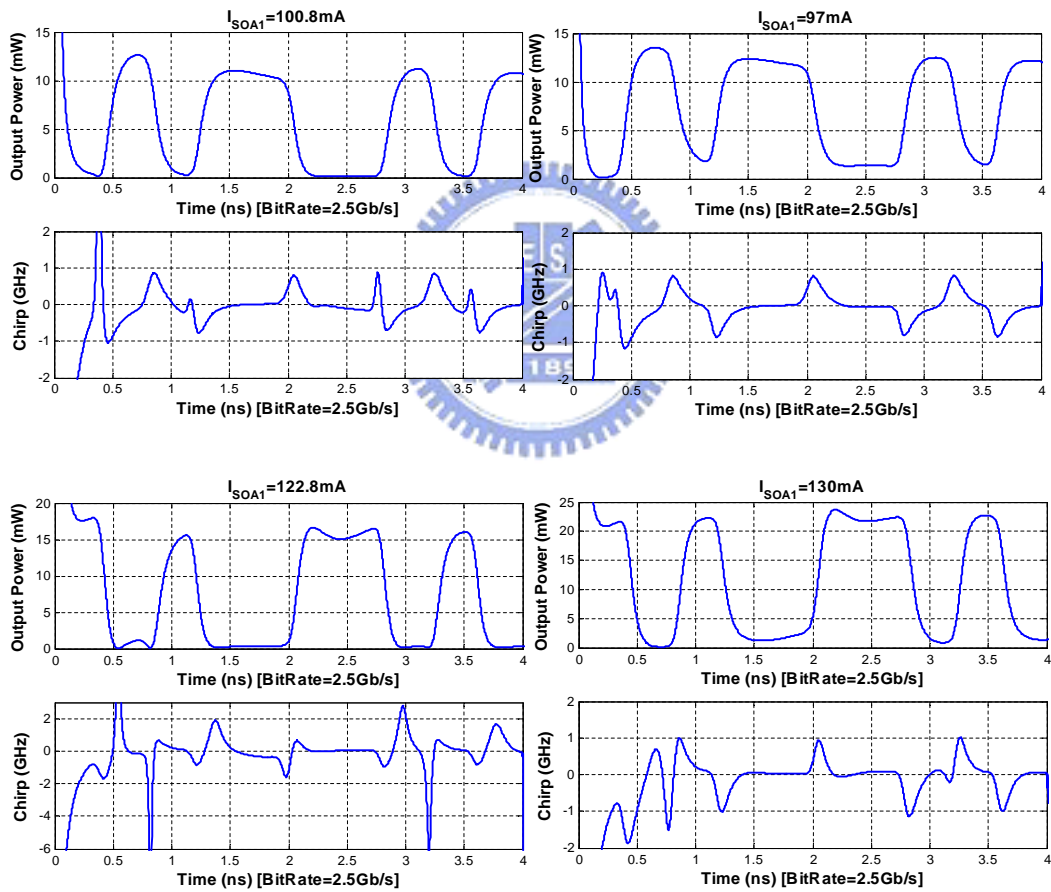


Figure 3-15: Pattern and frequency chirping of converted signals by XPM scheme. Upper and lower ones illustrate the non-inverted operation and inverted operation, respectively.

currents of phase SOA are also based on it. In fig. 3-15, the parts as time is smaller than 0.7 ns are abnormal due to the carrier density of the SOA's going to deplete when the signal and CW are injected in the beginning. Upper two conditions of fig. 3-15 which shows not only amplitude information of the converted signal but also the phase information are operated with non-inverted scheme. Note that the converted signal undergoes a red shift during the rising edge and a blue shift during the falling edge, resulting in pulse compression in the anomalous dispersion region. The negative chirp is due to the increased phase and power of the converted signal and the decreased carrier density caused by increasing the input signal power. In other words, the chirp condition of the rising edge by XGM will appear in the falling edge by XPM operated non-inverted configuration. On the other hands, lower two conditions of fig. 3-15 are inverted operation. By increasing the input signal, the output phase is increased and output power is decreased, like XGM scheme. Thus, the chirp is opposite to non-inverted operation, and pulse will broaden in the fiber.

The left two conditions of fig. 3-15 are very close to right ones, but there is some difference of injection currents and the frequency chirping near the falling or rising edge. The injection currents of left conditions are operated nearly complete destructive interference for the converted signals of level-zero, and the phase of the remaining power would be very sensitive to power fluctuation. So that the frequency chirping of level-zero is so different to right condition which is operated a little away from destructive point.

One of the drawbacks of XPM scheme is the complex operation parameters including two injection currents, the signal power, and the CW power. The static ER of the converted signal as a function of the phase current could be seen in fig. 3-15. On the other hands, the performance of the converted signal is also strongly depend the wavelength and the power, which is describe by static ER degradation and

illustrated in fig 3-16. The upper one of fig 3-16 shows the difference of ER due to different input signal power and CW power. At the same time, the lower one shows the dependence on the wavelength. It's obviously that fluctuation of the power is more seriously damaging the ER of the converted signal than the wavelength.

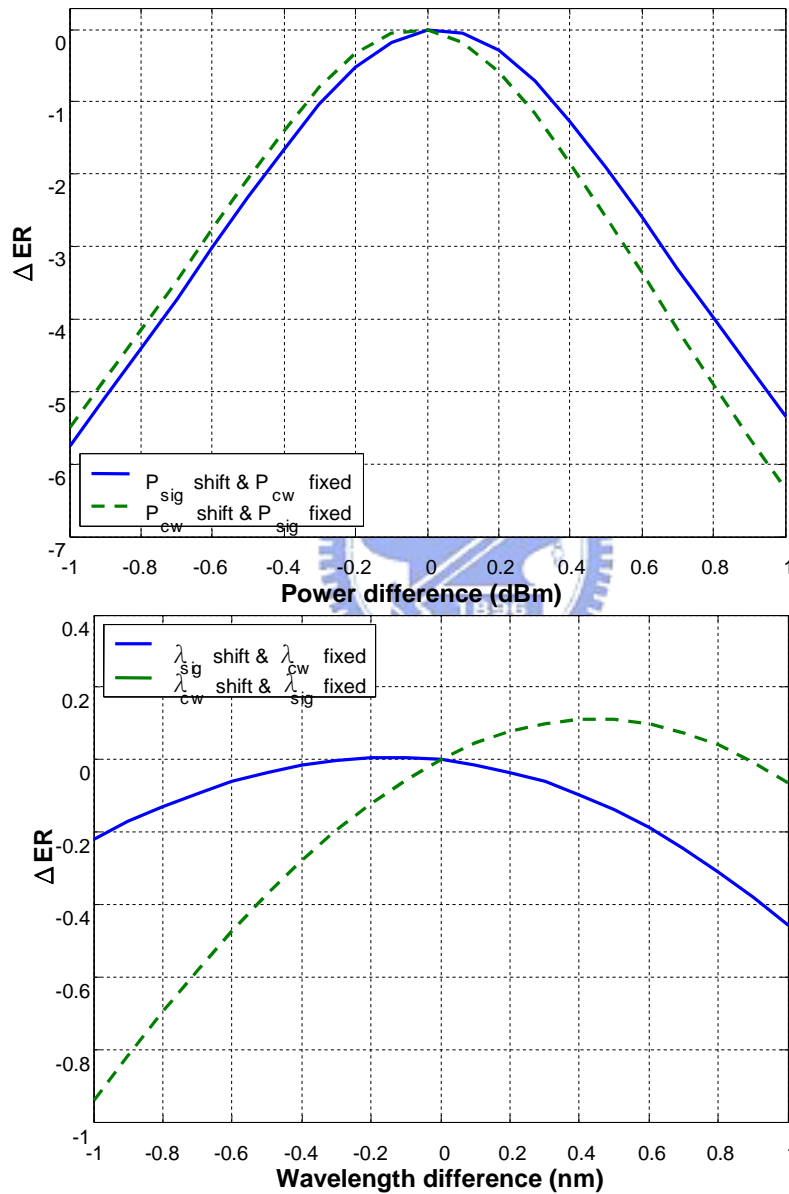


Figure 3-16: ER degradation as a function of the power and wavelength

3.3.2 Modulation bandwidth and polarization dependence for XPM

The calculated modulation bandwidth represented by EOR for the XPM method is shown in fig. 3-17. When the bit-rate of the input signal is increased to 10 Gbps, the peak-to-peak chirp is smaller than 5 GHz. The characteristics of the frequency chirping of the XPM method are superior to the XGM method clearly owing to the smaller degree of the carrier depletion. However, the EOR starts to decrease above 3 dB mainly due to the noise level-zero which is caused by incomplete destructive interference. In other words, in order to achieve higher conversion speed, the operation point of the XPM wavelength conversion should be selected at the steeper slope of the static transfer function.

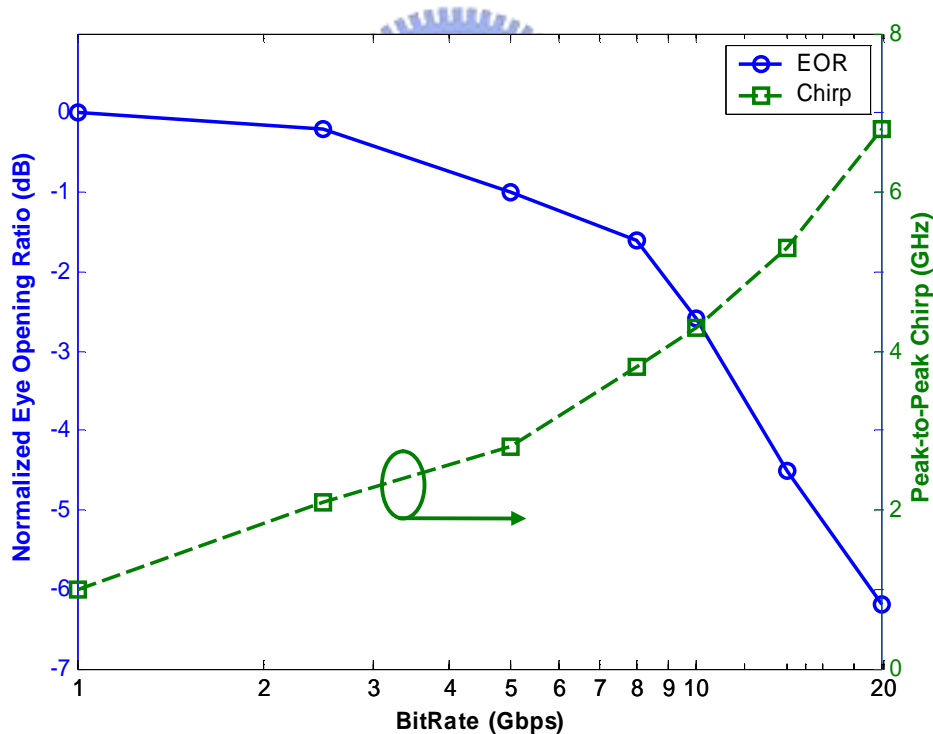


Figure 3-17: EOR and peak chirp as a function of the bit-rate in XPM scheme

Directly perceived through the senses, the XPM scheme might be polarization insensitive like the XGM method if the polarization independent SOA is used. But it

is not truth even for only 1 dB polarization dependent gain (PDG) of a polarization independent SOA. Fig. 3-18 shows that the static transfer function of the XPM scheme as a function of the polarization of the input CW. The PDG's of the phase and reference SOA's are set as 1 dB in the simulation. Most seriously, the converted signal could be distorted completely due to rotation of polarization of the CW. For example, the on-off of the input signal between -16 and -24 dBm will induce 20 dB ER of converted signal for the complete TM mode of the CW but only 4 dB for the complete TE mode.

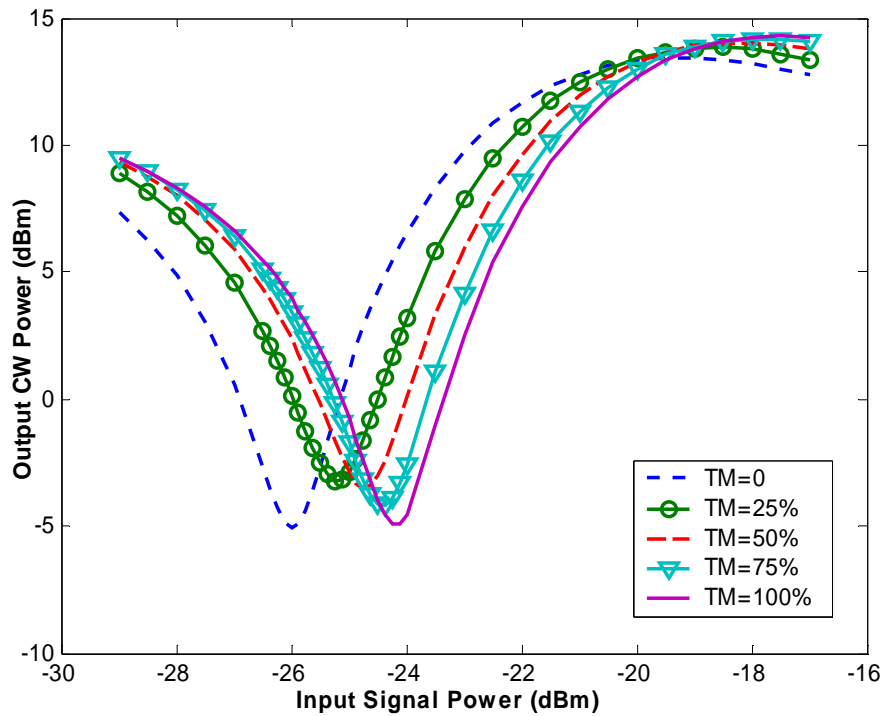


Figure 3-18: Static transfer function of XPM as a function of the polarization of the CW

3.4 Simulation Results And Discussion of FWM

3.4.1 Frequency response of inter- and intraband processes

From chapter 2, the third order susceptibility $c^{(3)}$ which can be decomposed into contributions from CDP, CH, and SHB could be simplified and written as

$$c^{(3)} = \sum_m c_m^{(3)} \cdot h_m(\Delta\omega) \quad (3-10)$$

where m specifies the nonlinear processes contribution to $c^{(3)}$, such as CDP, CH, and SHB. The zero-detuning susceptibility $c_m^{(3)}$ are

$$\begin{aligned} c_{CDP}^{(3)} &= (a\Gamma g + ig_m) / \wp^N \\ c_{CH}^{(3)} &= (a_{CH} + i) (g / \wp^{CH1} + g_m / \wp^{CH2}) \\ c_{SHB}^{(3)} &= (a_{SHB} + i) g / \wp^{SHB} \end{aligned} \quad (3-11)$$

where a_m is linewidth enhancement factor and frequency responses $h_m(\Delta\omega)$ are

$$\begin{aligned} h_{CDP}^{-1}(\Delta\omega) &= (1 - i\Delta\omega t_{SHB})(1 - i\Delta\omega t_{CDP}) \\ h_{CH}^{-1}(\Delta\omega) &= (1 - i\Delta\omega t_{SHB})(1 - i\Delta\omega t_{CH}) \\ h_{SHB}^{-1}(\Delta\omega) &= (1 - i\Delta\omega t_{SHB}) \end{aligned} \quad (3-12)$$

Detuning angular frequency $\Delta\omega$ is defined as $2p(f_p - f_s)$, where f_p and f_s are optical frequencies of the pump and signal. However, for the process of the CDP, a_{CDP} and t_{CDP} are equal to a and t_e which are mentioned at Table 1 and equation (2-4), respectively. The simulation parameters and nonlinear SOA parameters are summarized in Table 3-2 [16].

The conversion efficiency of FWM is shown in fig. 3-19. The conversion efficiency is defined as the ratio of the output converted signal power to the input signal power. The conversion efficiency decreases at large detuning frequency since the frequency response of nonlinear processes which are described in equation (3-11) decrease with the increase of detuning frequency. In addition, down wavelength conversion efficiency is higher than up wavelength conversion. This is mainly

<i>Symbol</i>	<i>Description</i>	<i>Value</i>	<i>Unit</i>
L	SOA length	5×10^{-4}	m
V	Active layer volume	7.5×10^{-17}	m^3
\wp^N	Saturation power	3×10^{-3}	W
\wp^{CH1}	CH parameter	1.82×10^{-1}	W
\wp^{CH2}	CH parameter	2.63×10^{-1}	W
\wp^{SHB}	SHB parameter	4.76×10^{-1}	W
a_{CH}	Linewidth enhancement factor by CH	-2.3	
a_{SHB}	Linewidth enhancement factor by SHB	0	
t_{CH}	CH time	112×10^{-15}	s
t_{SHB}	SHB time	500×10^{-15}	s

Table 3-2: Nonlinear Parameters in SOA's

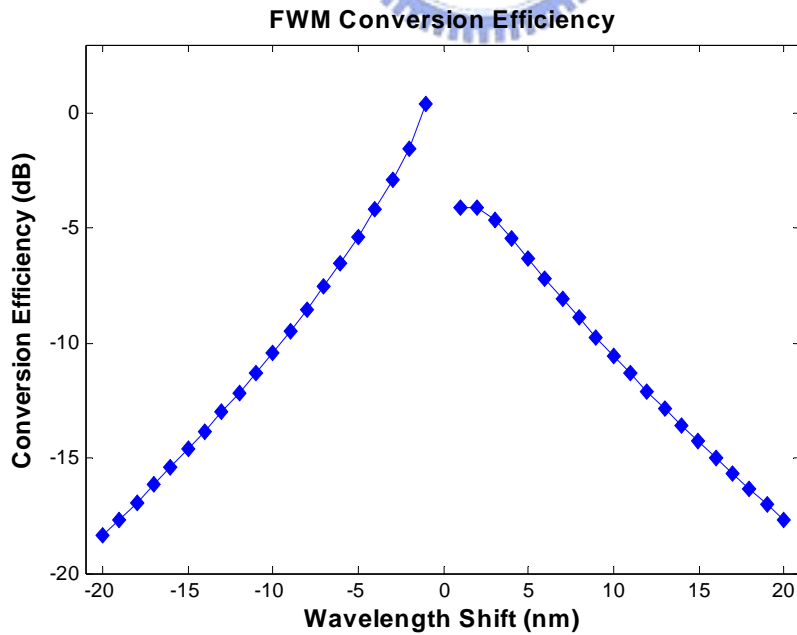


Figure 3-19: Conversion efficiency by FWM as a function of wavelength shift

due to destructive or constructive phase interference between the contributing FWM mechanisms such as CDP, CH, and SHB.

Fig. 3-20 shows schematically the value of $c_m^{(3)}$ which are complex numbers and can be regarded as two-dimensional vectors. For the sake of simplicity, only two processes (CDP and SHB) and $a_{SHB} \approx 0$ compared with a_{CDP} are assumed. Note that, when $|\Delta w|$ increase, the direction of $c_{CDP}^{(3)}$ changes earlier than $c_{SHB}^{(3)}$ because the t_{CDP}^{-1} is smaller than t_{SHB}^{-1} . $c_{CDP}^{(3)}$ and $c_{SHB}^{(3)}$ interfere in phase for

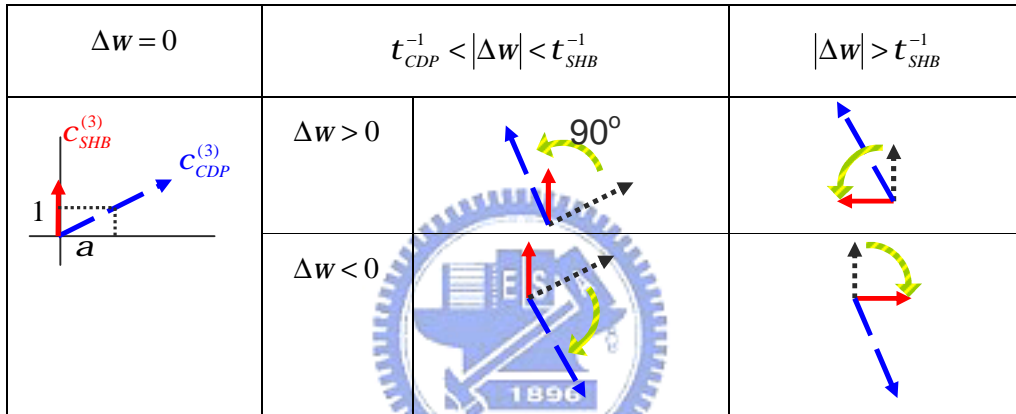


Figure 3-20: Illustration of directions of third-order susceptibilities

positive detuning, and out of phase for negative detuning, which is the origin of the asymmetric conversion characteristics. If $|\Delta w|$ increases beyond t_{SHB}^{-1} , $c_{SHB}^{(3)}$ also rotates, and the phase relationship becomes the same as that for $|\Delta w| = 0$.

3.4.2 Spectral inversion due to FWM

Fig. 3-21 shows the pattern of the input signal and the converted signal. The input signal with positive frequency chirping is illustrated. From the figure, it's obviously that the converted signal not only has the same amplitude modulation but

also the inversion spectrum and these characteristics of the FWM method guaranteed the format transparency of the conversion.

But the drawbacks of the FWM method are that the ER degradation and the parasitic chirp. The ER degradation is due to that the higher signal power level (level-one) will suffer more gain depletion and less conversion efficiency. On the other hands, the parasitic chirp is resulted from the fact that the index of the SOA

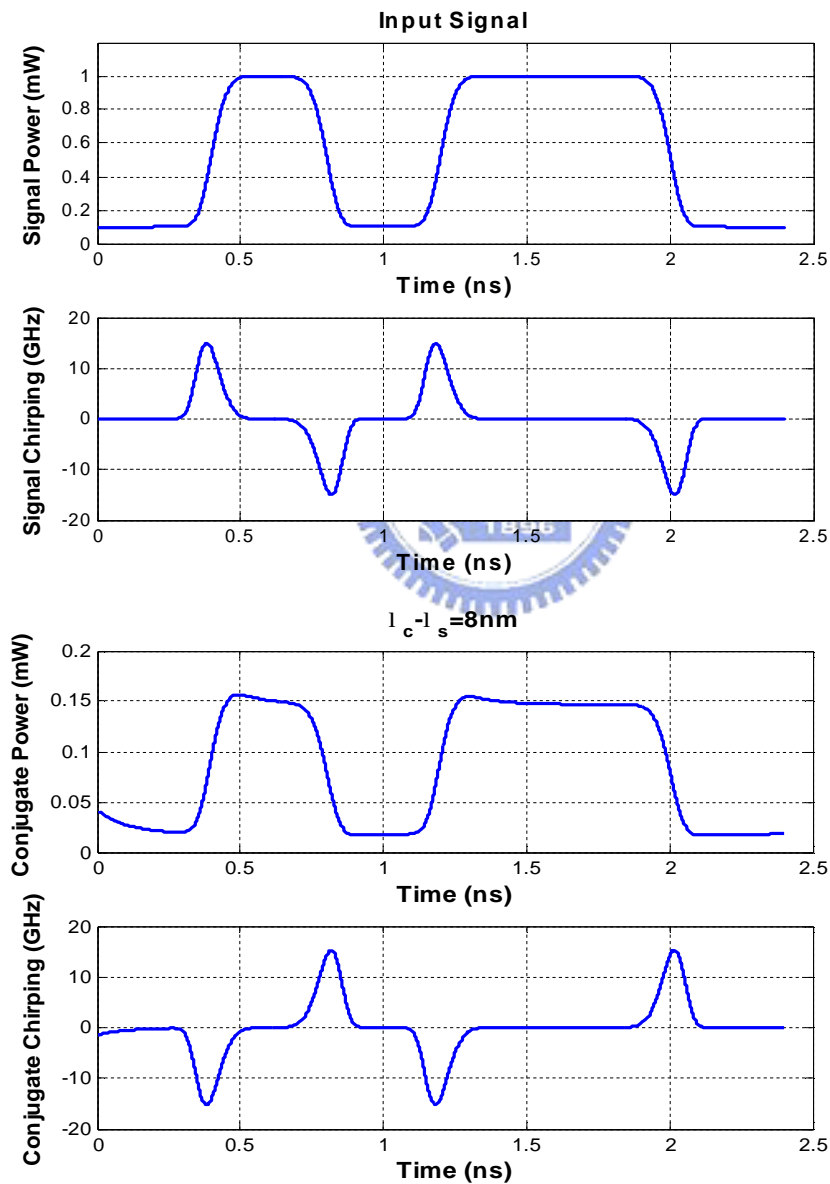


Figure 3-21: Pulse pattern and frequency chirping of the input signal (upper) and the converted signal (lower).

might be modulated by input signal during wavelength conversion. From fig. 3-22 which illustrates the ER and parasitic chirp of the converted signals as a function of the pump and signal power, the signal-to-pump power ratio will dominate the performance of the ER and chirp. When the power ratio is large, the fluctuation of the carrier density becomes more serious and it results the higher ER degradation and more parasitic chirp. In contrast, the lower signal-to-pump power ratio is, the better performance the converted signal is.

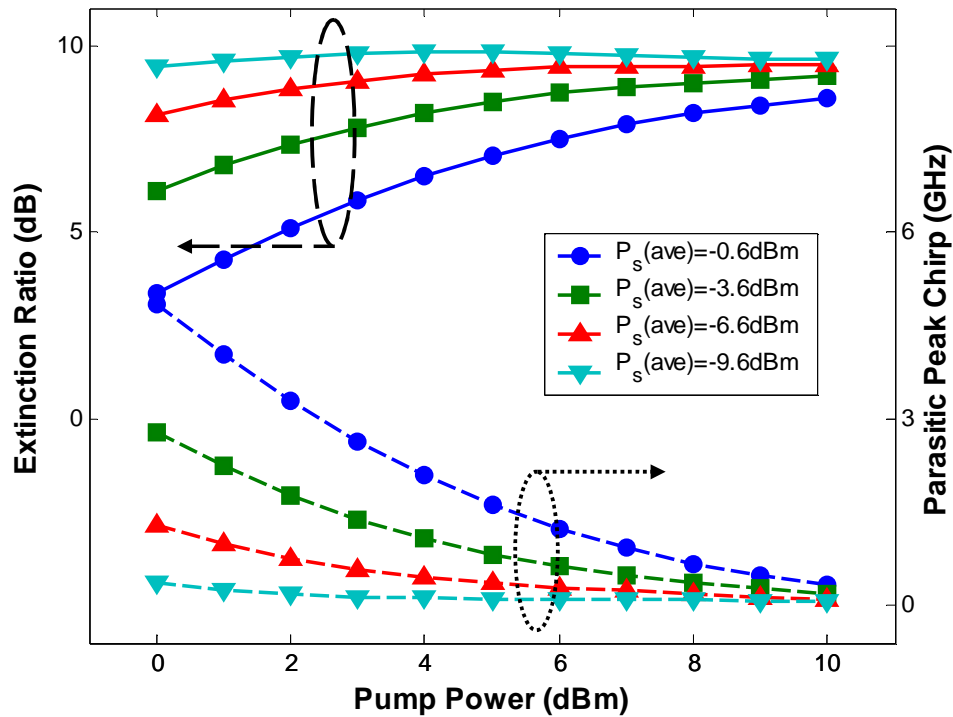


Figure 3-22: ER and parasitic chirp of the converted signal as a function of the pump and the signal power.

3.4.3 ER improvement in rFWM

In order to overcome the problem that the ER degrades in the FWM scheme, the reverse FWM (rFWM) is propose. In common FWM, the converted wavelength I_c is equal to $I_p + I_p - I_s$, and a simplifivative formula of output converted signal is

$$P_c = G_s G_p^2 P_s P_p^2 R(\Delta w) \quad (3-13)$$

where G_i and P_i are the gain and the input power for the signal or the pump, and $R(\Delta w)$ is frequency response of FWM. In contrast, rFWM are operated as $I_c = I_s + I_s - I_p$. From equation (3-13), if the gain of the SOA is unsaturated, ER of the output converted signal will become twice of ER of the input signal. However, the gain would be saturated by input signal, and therefore induce the effect of XGM which could degrade the ER of the converted signal.

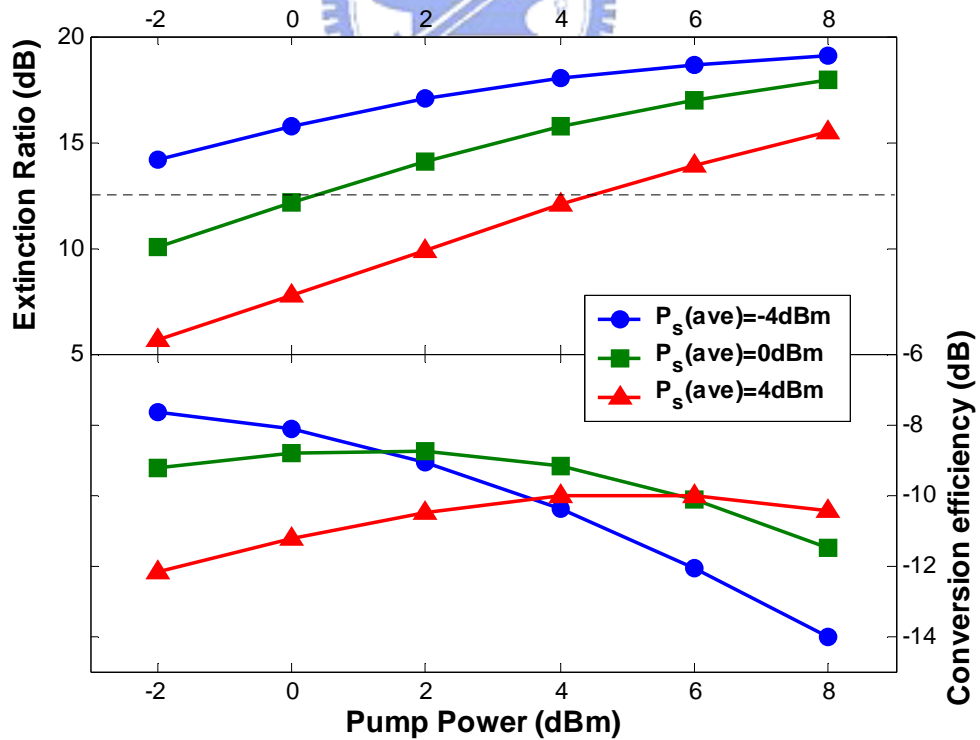


Figure 3-23: ER (upper) and conversion efficiency (lower) of the converted signal using rFWM scheme as a function of the pump and signal power.

In the fig. 3-23, the conversion efficiency and ER of the converted signal by rFWM scheme are shown. The ER is strongly dependent on the signal-to-pump power ratio, and the ER will increase even to ideal ER of 20 dB by decreasing the ratio to reduce the XGM effect. When signal-to-pump power ratio increases, the ER of the converted signal might degrade seriously owing to strong gain saturation.

The conversion efficiency will increase as the pump power increase, if the high power signal which strongly saturated and dominated the gain of the SOA is coupled into the SOA. However, when the weak signal can't dominate the carrier distribution anymore, the conversion efficiency will degrade with higher pump power.

With the same chirp and ER of the input signal illustrated in fig. 3-21, the output signal with amplitude and phase information are shown in fig. 3-24. Because the

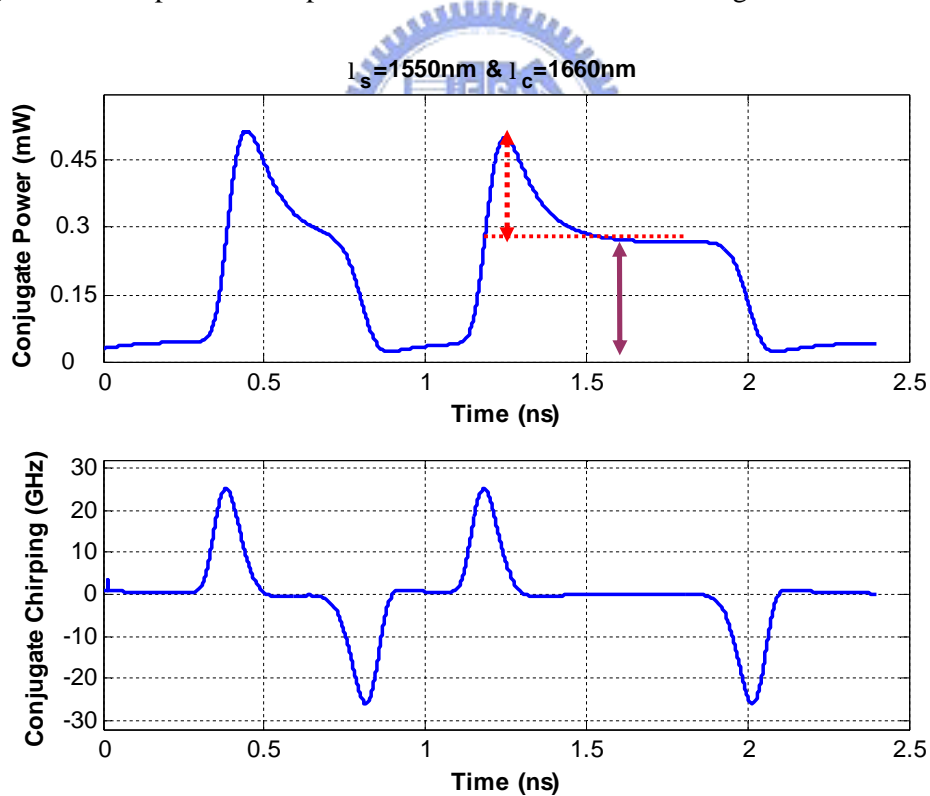


Figure 3-24: Pulse pattern and frequency chirping of the input signal (upper) and the converted signal (lower) using rFWM scheme.

converted field is influenced by the square of the signal field in rFWM scheme, rFWM scheme suffer a very serious problem which the frequency chirping of the converted signal is also double. Further, fig. 3-25 shows the parasitic peak chirp and overshoots as a function of the pump and the signal power. The converted signal contains positive chirp like the input signal. However, the rising edge of the signal which induces the carrier density decreasing would generate a red shift, and vice versa. Thereby, the peak chirp of the converted signal illustrated in fig. 3-24 is below 30 GHz, and the positive parasitic chirp of fig. 3-25 indicates a blue shift during falling edge and the negative parasitic chirp denotes a red shift during rising edge. Again, the signal-to-pump power ratio will also dominate the varying of the value of parasitic chirp, and the negative chirp is larger than positive owing to the faster process of gain

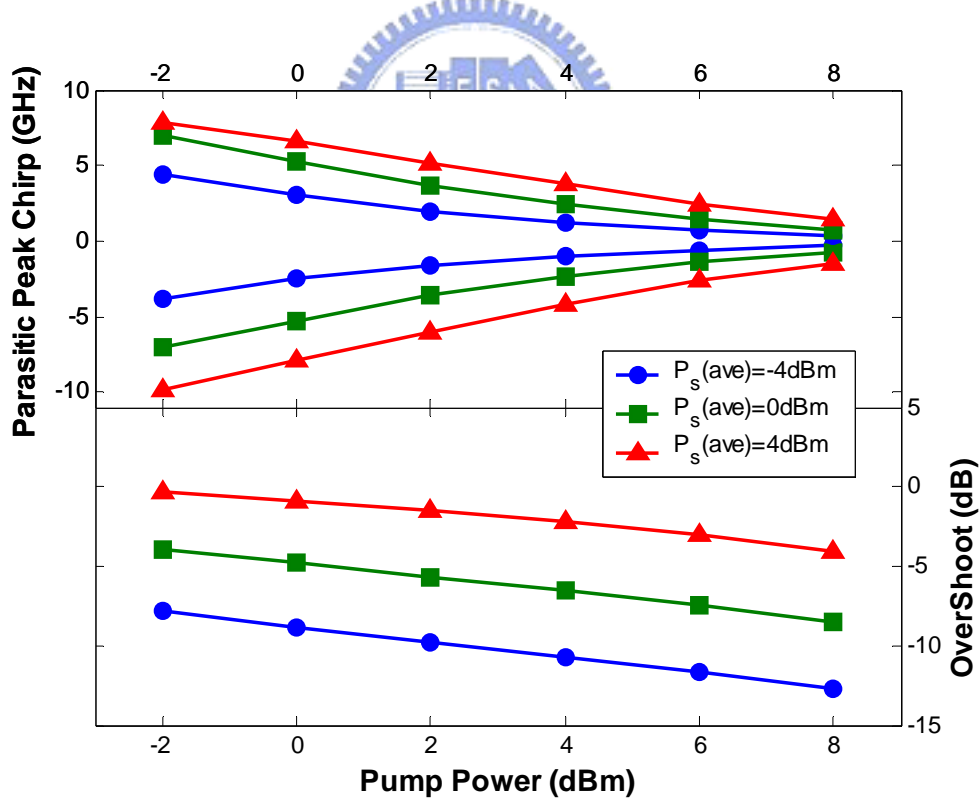


Figure 3-25: Parasitic peak chirp (upper) and overshoot (lower) of the converted signal using rFWM scheme as a function of the pump and signal power.

depletion than recovery as demonstrated in the part of XGM scheme. The value of overshoot, which is defined as the ratio of the overshooting power and the power of level-one illustrated in fig. 3-24 by dashed arrow and solid arrow respectively, is also increasing as signal-to-pump power ratio monotonously.

3.5 Simulation Results And Discussion of Cross Polarization Modulation

3.5.1 Rotation of SOP in a SOA

For asymmetric waveguide geometry, the confinement factors, effective guide refractive indices and carrier distribution are not identical at the TE/TM orientation of a SOA. However, the mainly influence on signal-induced birefringence in the SOA is coming from the difference between the confinement factors at the TE/TM

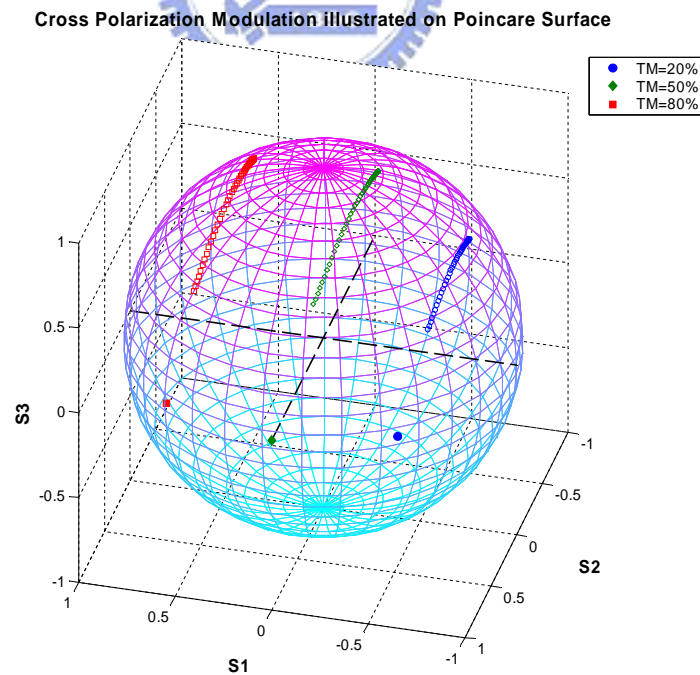
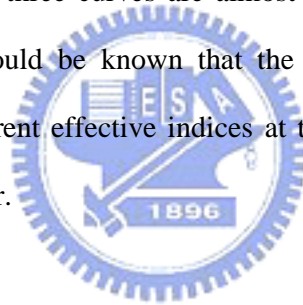


Figure 3-26: The paths of rotation of the output polarization in cross polarization modulation

orientation. Therefore, the carrier distribution, differential refractive indices, and effective refractive indices for zero-free carrier density at the TE/TM orientation are assumed as the same. In the simulation of the cross polarization effect, the confinement factors are set as 0.32 and 0.29 for TE/TM modes, and using these parameters will produce 1 dB polarization dependent gain as the SOA isn't saturation yet. Noteworthy, the polarization of the input signal isn't important and neglected.

Fig 3-26 shows that the path of the output polarization, as the input CW power is 1.5 dBm, and the input signal power is varying from -20 to 10 dBm. In the figure, three line with different makers illustrate three conditions of input linear polarization of the CW which are represented by different power percentage of the TM mode. From the Poincare's sphere, three curves are almost rotated as the varying of input signal power. Hence, it could be known that the rotation of the polarization is mainly induced by the different effective indices at the TE/TM orientation, and the varying of PDG do not matter.



3.5.2 Changing conversion styles by the polarizer

Using the same conditions of fig. 3-26, the static curves of the converted signals are shown in fig. 3-27. Here shows two set of curves, which represent the inverted and non-inverted converted signals. This characteristic is the same as the XPM method owing to the identical interferometric operations mentioned in chapter 1. However, from inverted conversion to non-inverted conversion of the cross polarization modulation method, only changing of the orientation of polarizer is need unlike the XPM method. In the case of non-inverted conversion, the polarizer is set in such a way that the CW cannot pass through the polarizer when only the CW is present. If the signal is coupled into the SOA, the additional birefringence in the SOA leads to a phase difference between TE/TM modes of the CW. As a

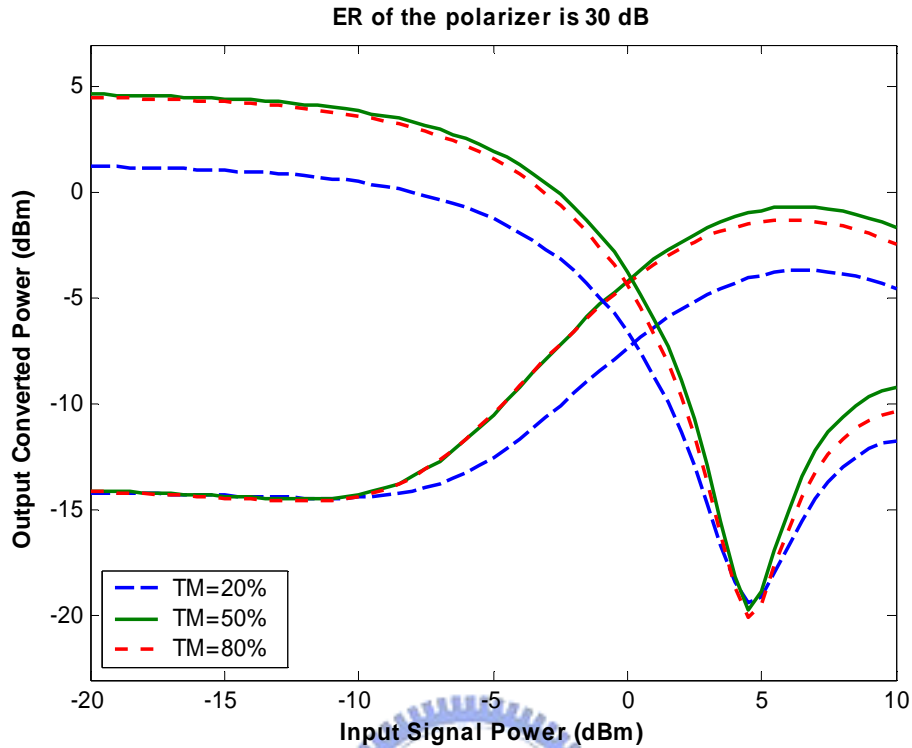


Figure 3-27: Transfer function of the CW with different input polarization containing inverted and non-inverted conversion.

consequence, some CW could pass through the polarizer. In contrast, the maximum output power of CW passing through the polarizer is the inverted scheme. On the other hands, different input polarization of the CW have different conversion slope. For the polarization aligning on complete TE/TM modes, the signal could not induce the birefringence effect, namely, no conversion. 20%, 50% and 80% power coupled to the TM orientation are simulated, in which the 50% behave the best performance in either inverted or non-inverted conversion due to the most degree of rotation induced. However, the curve of 80% power of TM performs better than 80% power of TE, because the light aligning on the TM mode suffers the smaller confinement factor as well as less gain. That is, the more part of the CW is coupled into the TM mode appropriately, the more average distribution of the output between the TE/TM modes is, and the birefringence effect will be more obvious.

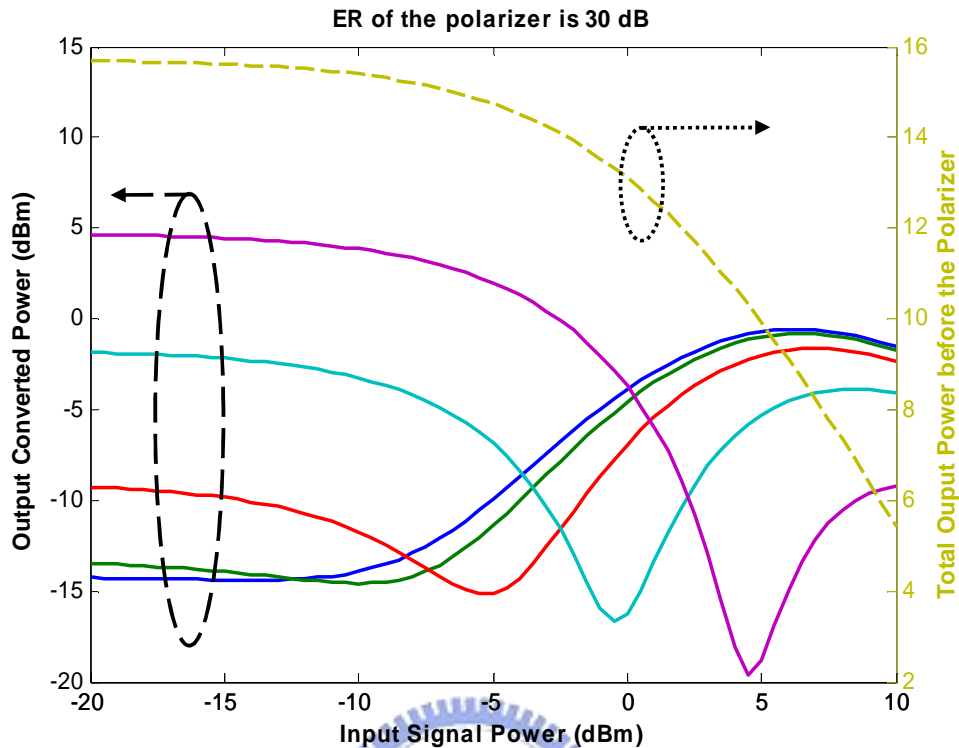


Figure 3-28: Different transfer curves (solid lines) with different orientation of polarizer and the total CW output power (dashed line) decreases as input signal power increasing.

In fig. 3-28, there are several curves which are shifted by adjusting the orientation of the polarizer. These curves show that the power varying of the input signals which come through different length of fibers could be adjusted only by the polarizer. Unlike the XPM method, several parameters, such as currents and the CW power, might be modified complexly. Besides, the inverted transfer functions become steeper as increasing the average signal power due to XGM effect. On the contrary, the non-inverted ones become gentler.

Fig. 3-29 illustrates the pattern of the converted signal including non-inverted and inverted scheme. Like XPM, the non-inverted and inverted converted signals suffer negative and positive frequency chirping, respectively. The amplitude of the frequency chirping is dependent on the on-off degree of the carriers in the SOA. For

the performance of modulation bandwidth, cross polarization modulation is also extremely similar to the XPM method.

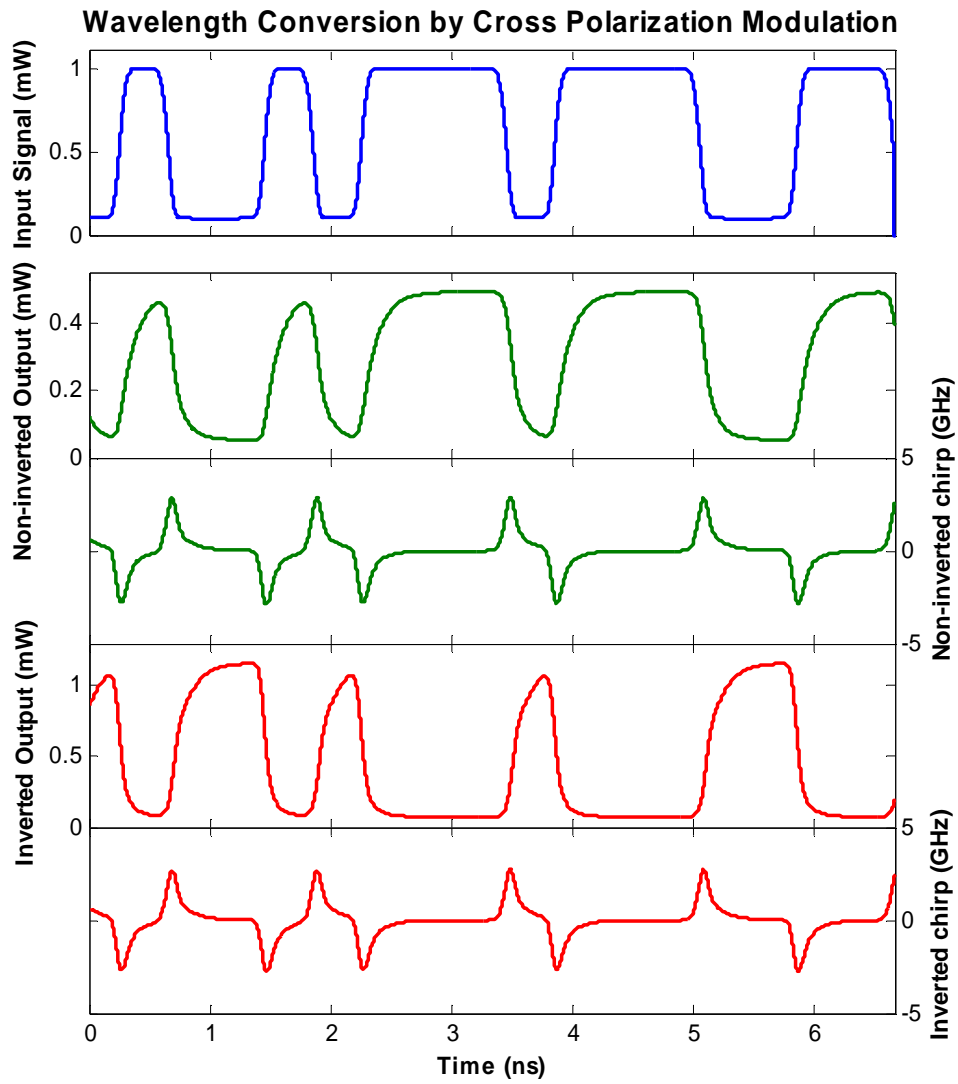


Figure 3-29: Input signal patten (1st), pulse pattern and frequency chirping of the non-inverted converted signal (2nd& 3rd) and the inverted converted signal (4th& 5th).

CHAPTER 4

EXPERIMENT SETUPS AND RESULTS OF WAVELENGTH CONVERTERS

Besides the pulse patterns of converted signals and eye diagrams, the bit error rate (BER) test is also very important for the examination of the performance after wavelength conversion. In order to know the information about the frequency chirping of the converted signal, a simple method which transmits the converted signal through a standard single mode fiber is applied. Therefore, in this chapter, the eye diagrams caught by oscilloscope and the BER test including back-to-back and transmission in SMF are focused.

4.1 Cross Gain Modulation

4.4.1 Experimental setup

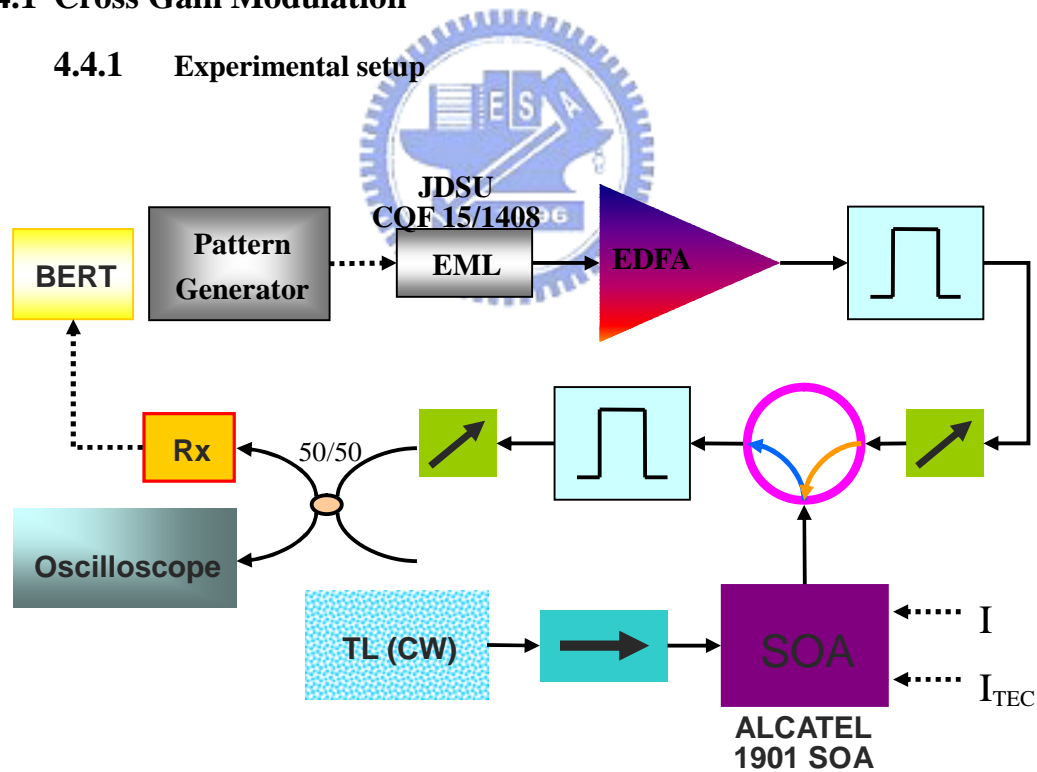


Figure 4-1: Experimental setup of counter-propagation XGM scheme.

Fig. 4-1 shows the experimental setup of counter-propagation XGM method. The transmitter of the input signal is the JDS Uniphase CQF 15/1408 10Gb/s EA-

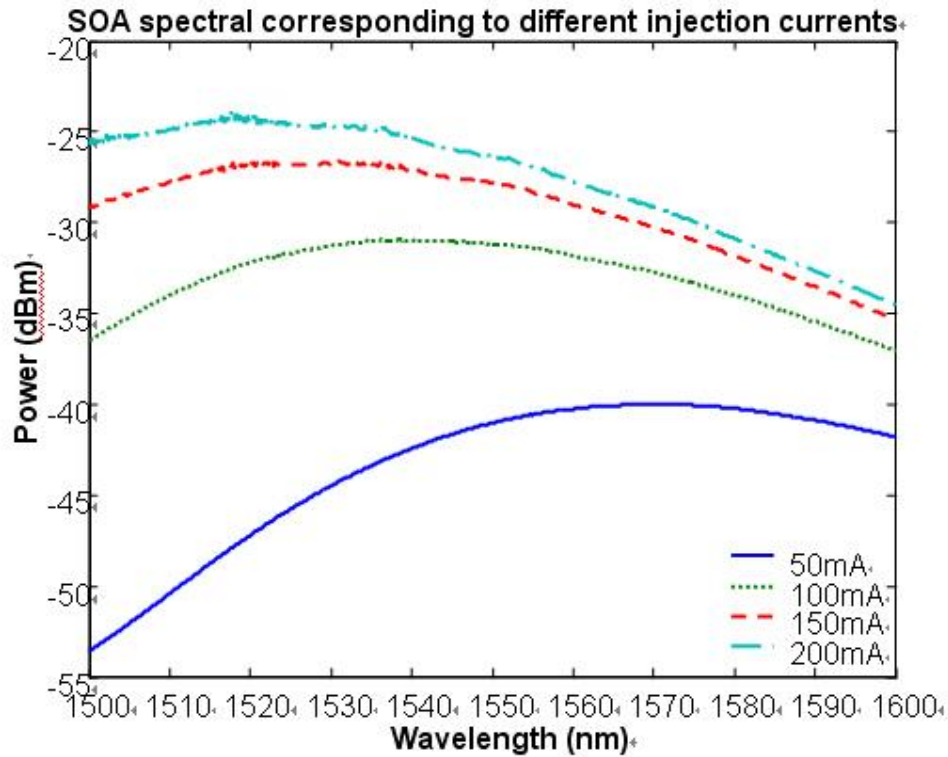


Figure 4-2: Gain spectrums of the Alcatel SOA for different injection currents

Modulated DFB laser and the Alcatel 1901 SOA is used as wavelength converter by the XGM scheme. In order to realize the varying of the SOA gain spectrums, the SOA gain spectrums corresponding to different injection currents are measured and shown in fig. 4-2. The reason for the down-wavelength shift of the gain peak as increasing the injection current has mentioned at chapter 3.2, which is related to the up-moving of the quasi-Fermi level of the conduction band. Moreover, it explains why the wavelength up-conversion might suffer the problem of the ER degradation.

In the experiment, the counter-propagation scheme illustrated in fig. 4-1 is adopted. The -1 dBm input signal at 1551.72 nm and -11.5 dBm CW at 1550.12 nm enter the SOA from the opposite face. It is said that a tunable optical filter used to filter out the original signal could be avoided in the counter-propagation scheme [17]. However, the optical filter is still used in the experiment because of the reflection of

the original signal which becomes non-white noise for the converted signal.

4.4.2 Performance analysis for XGM

The eye diagrams with $2^{31}-1$ pseudo random bit sequence (PRBS) of the converted signal with and without transmission through the SMF are shown in fig. 4-3, in which the patterns of 27-1 PRBS are also presented. The pulses of the converted signal appear the pattern dependent characteristics. The continuous changing between level one and zero makes the converted signal couldn't response in time, like the simulation results illustrated in fig. 3-8. The bandwidth of the wavelength converted also makes the eye diagrams smoother. No matter how the response of the converter is, the serious positive frequency chirping could not be ignored at all. The converted signal after 25 km SMF is distorted by anomalous dispersion completely and

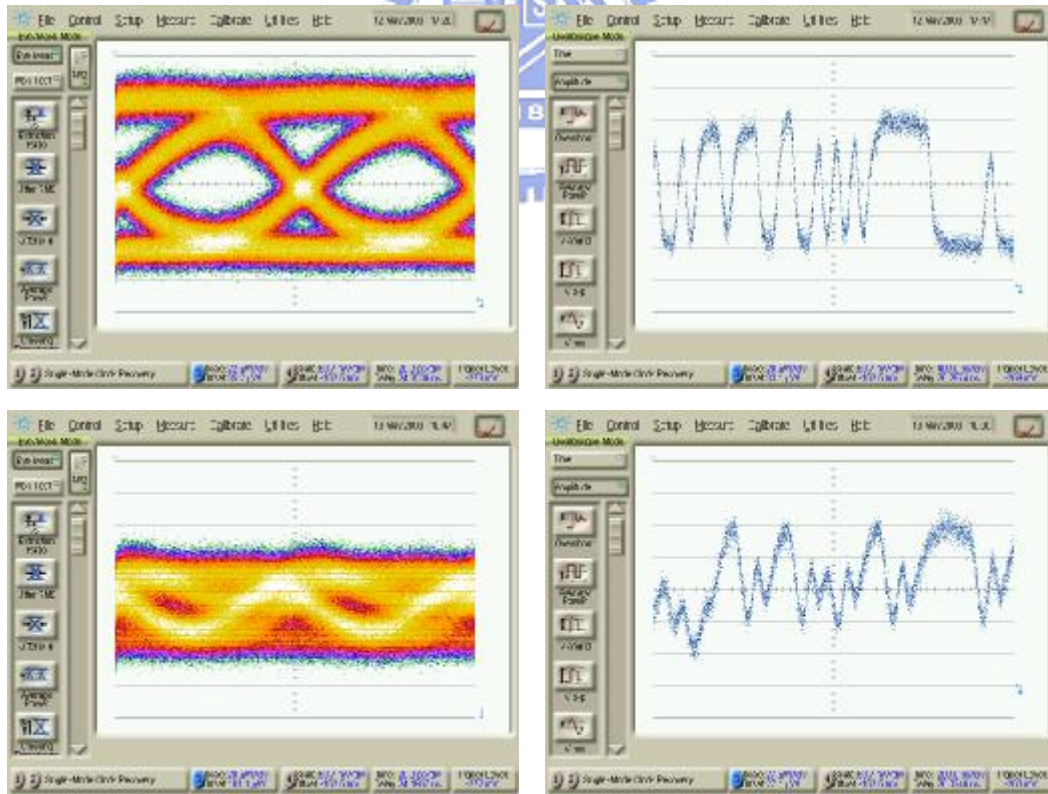


Figure 4-3: The eye diagrams (left) and 2^7-1 PRBS pulse patterns (right) of the converted signal for back-to-back (upper) and transmission after 25 km of SMF28 fiber (lower) in counter-propagation XGM scheme.

the crooked eye diagram and pulse patterns are also shown in fig. 4-3.

Fig. 4-4 shows the BER curves of the input signal and converted signal. Due to the limit of the bandwidth, the converted signal without transmission in SMF has the 4 dB penalty. With transmission, the converted signal has been distorted and the BER can not be measured.

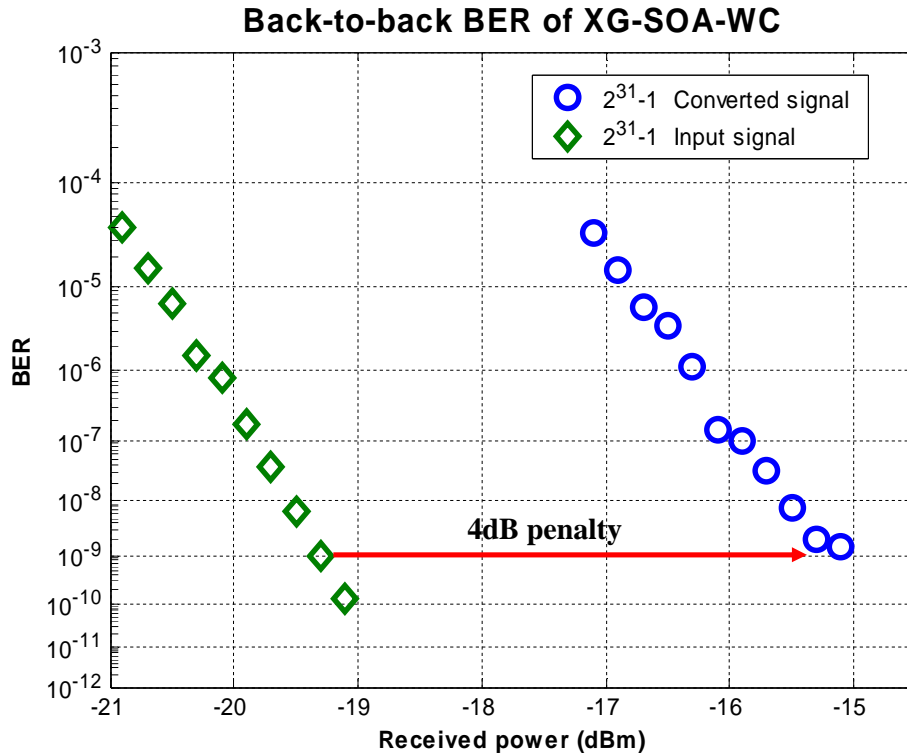


Figure 4-4: BER curves of the input signal and converted signal

4.4.3 The relation between BER and operation powers

In fig. 4-5 and 4-6, the BER curves with the fixed received power (-15 dBm) as a function of the input signal and CW respectively are measured to realize the power dependent performance of the converter. The CW power is fixed at -11.5 dBm and the input signal power is changing to measure BER in fig. 4-5. From the figure, the input signal power to get the best performance is around -1 dBm, and the power

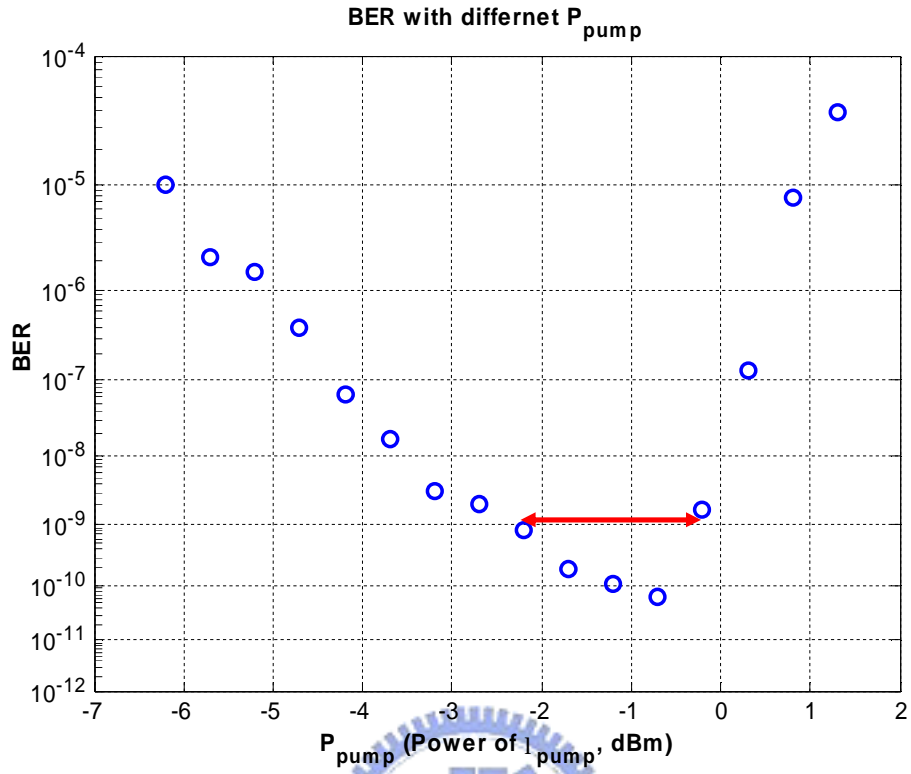


Figure 4-5: BER curve as a function of the input signal power

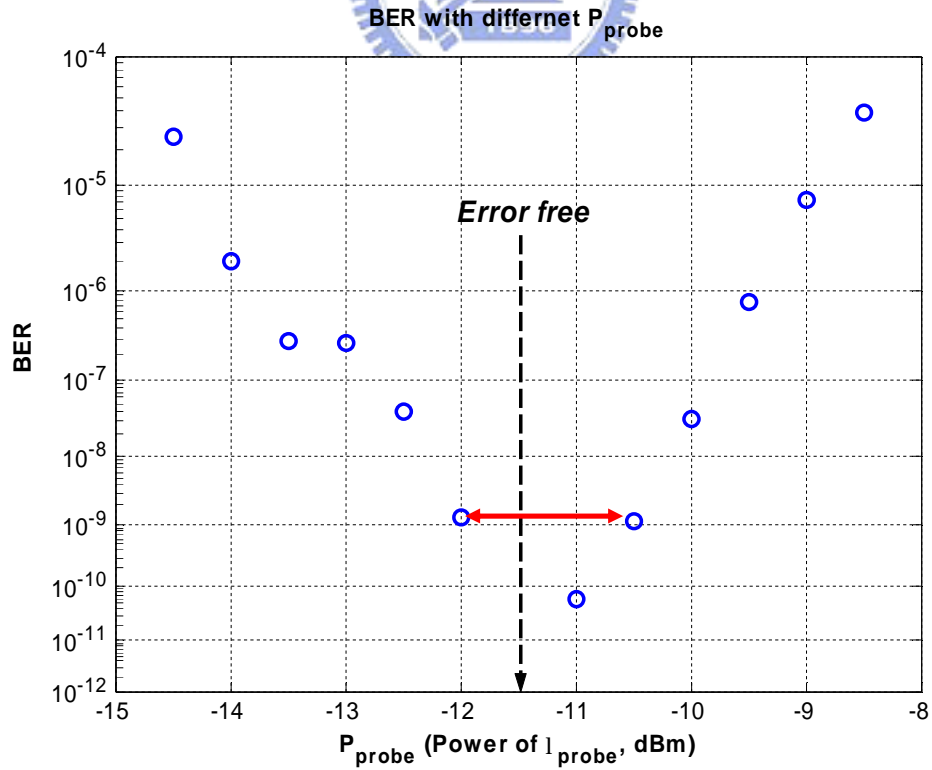


Figure 4-6: BER curve as a function of the CW power

window to obtain the BER below 10^{-9} is about 2 dB. That is, if the fluctuations of the input signal power exceed this range, the BER above 10^{-9} couldn't be obtained for -15 dBm received power. Fig. 4-6 is similar to fig. 4-5, but the CW power change as the input signal power is fixed. The power window for the BER of 10^{-9} is only 1.5 dB. When the CW power becomes smaller, the varying of gain depletion is controlled by the input signal more effectively, and therefore, better performance of the converted signal could be obtained. However, there always is amplified spontaneous emission (ASE) in SOA's, and the smaller output converted signal power for the smaller CW power will become noisier and the performance of the converted signal will degrade.

4.4.4 Timing jitter for co- and counter-propagation

Fig. 4-7 shows the eye diagrams of the converted signal by using co- and counter-propagation XGM methods. It is clear that the timing jitter of the converted signal in counter-propagation scheme is larger than co-propagation scheme due to the different degree of changing of the carrier density in longitudinal domain of a SOA.

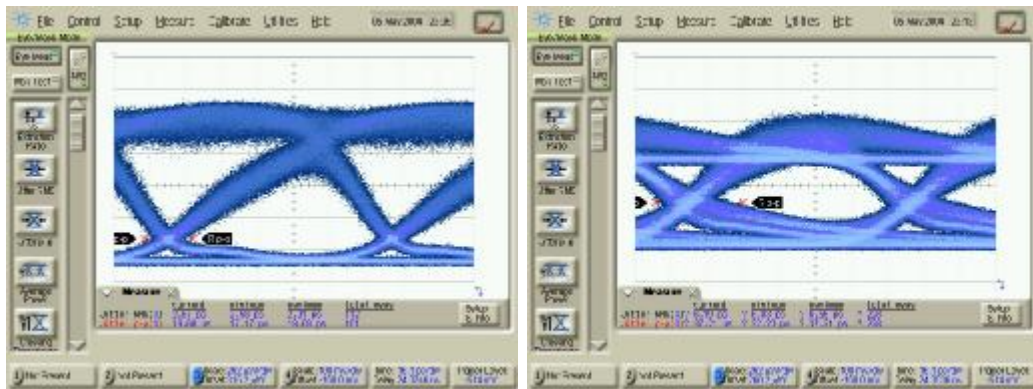


Figure 4-7: The eye diagrams of the converted signal in co- (right) and counter- (left) propagation XGM schemes.

4.2 Cross Phase Modulation

4.4.1 Experimental setup

Because the interference method is sensitive to the optical length of the paths, the SOA's used for XPM are usually integrated in order to obtain steady operation. The XPM modules in the experiment are manufactured by Kamelian which is used in the experimental setup of XPM shown in fig. 4-8. In this experiment, the co-propagation scheme is adopted, and because of two SOA's being used the parameters of the current of the reference SOA is need besides the current of the phase SOA, the signal power and the CW power. Therefore, the search of the parameters for the best conversion performance is more complex compared with XGM scheme. The input signal is modulated at 10 Gb/s by LiNbO₃ Mach-Zehnder external modulator with a $2^{31}-1$ PRBS. As mentioned in chapter 3, the polarization controllers are put on due to the polarization sensitive transfer function in the XPM scheme even the polarization independent SOA's are used.

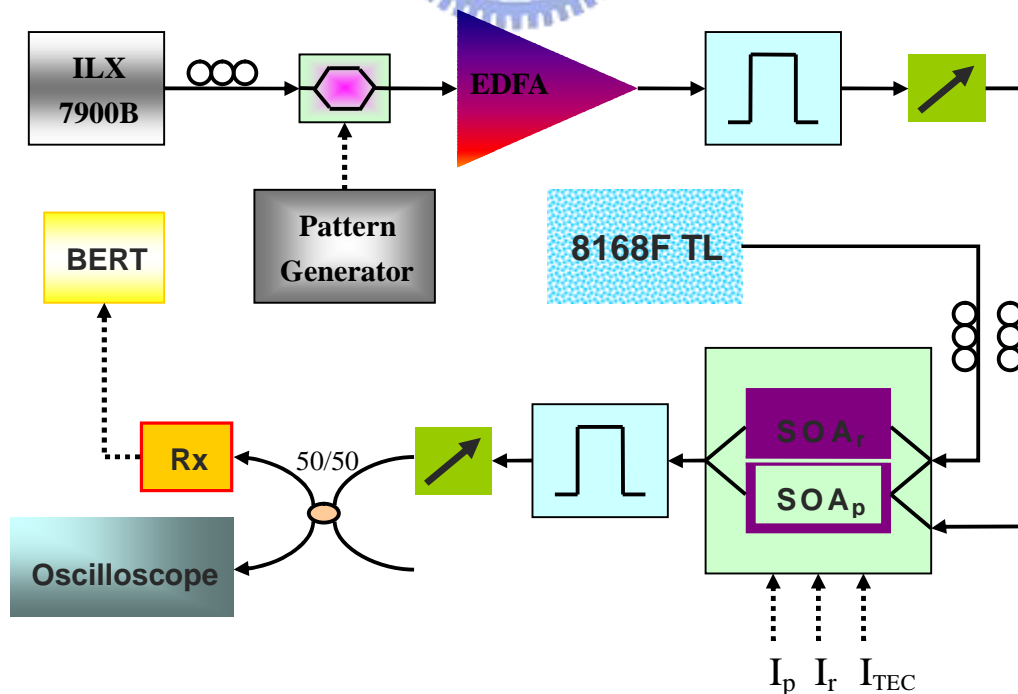


Figure 4-8: Experimental setup of co-propagation XPM scheme.

4.4.2 Performance analysis for XPM

The performance of XPM is illustrated by BER test and shown in fig. 4-9, in which the BER curves of the input signal, the non-inverted signal, and inverted signal with and without transmission are measured. For the non-inverted conversion scheme, the currents of the phase and reference SOA's are 307 mA and 225 mA, respectively, as well as the average input signal power of 1.1 dBm and the CW power of 3.8 dBm. On the other hand, these parameters are 380 mA, 180mA, -0.9 dBm, and -0.2 dBm in turn for the inverted conversion scheme. And the wavelengths of the signal and CW are 1555.75 and 1550.12 nm for both schemes, respectively. The text of the legend of the figure indicate back-to-back, transmission in 25 km SMF, and in 50 km SMF by the abbreviations of B-to-B, 25SMF, and 50SMF, respectively. From the figure, the power penalty for non-inverted conversion is about 2.2 dB and 0.5 dB for inverted conversion. After transmission in 50 km SMF, the signal suffers

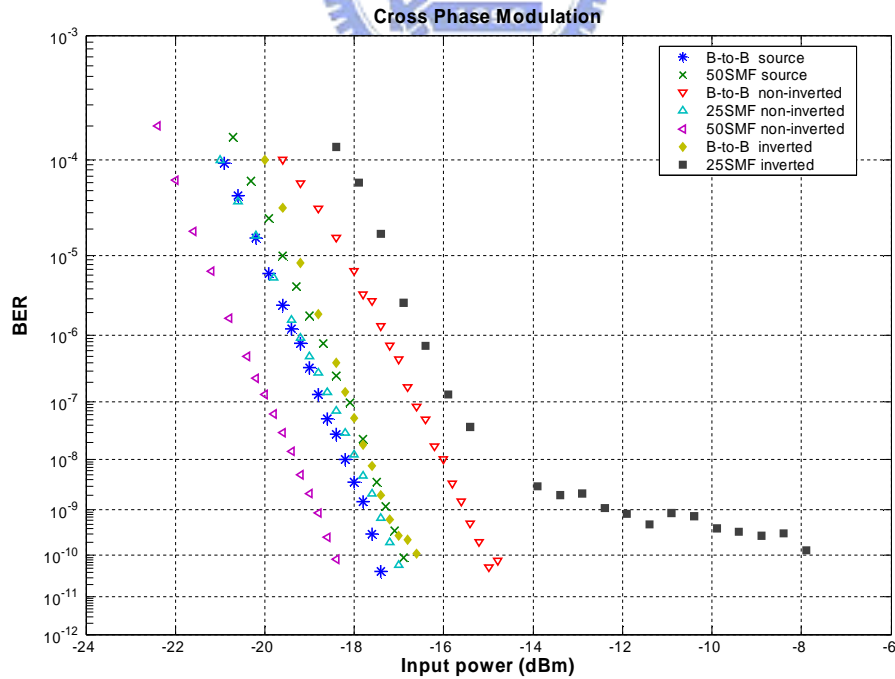


Figure 4-9: The BER curves of the input signal, non-inverted converted signal, and inverted converted signal with and without transmission.

a power penalty of 0.5 dB. However, for the inverted conversion signal which has positive chirp due to the index modulation by the input signal, the power penalty of 5.2 dB is measured after transmission in 25 km SMF and this converted signal, which undergoes noise floor for the BER curve at BER of 10^{-10} , is distorted very seriously by dispersion in SMF. In the figure, the BER of the inverted output signal with transmission in 50 km SMF is not shown through too serious distortion. In contrast,

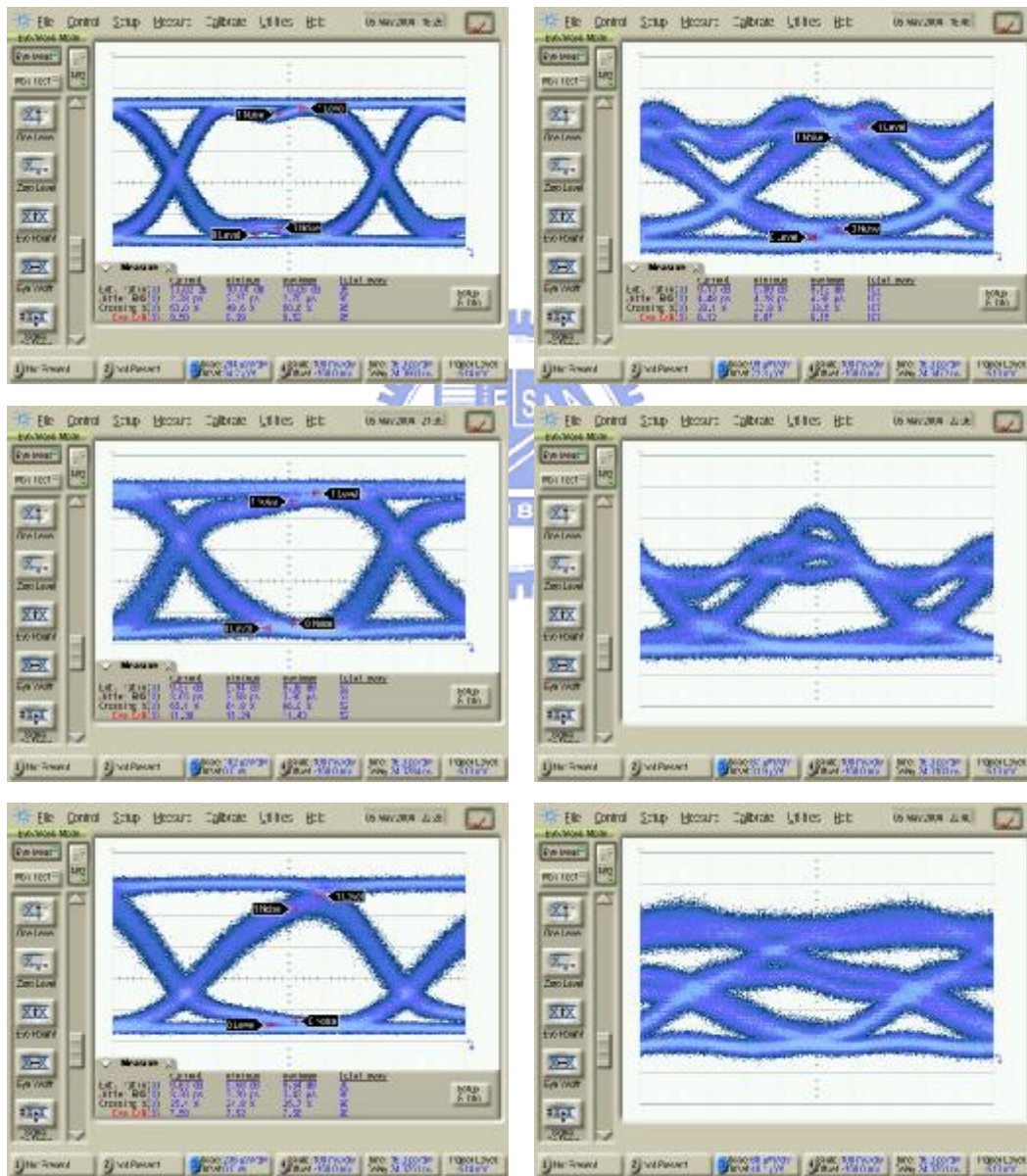


Figure 4-10: Eye diagrams of the input signal (upper), the non-inverted conversion signal (middle), and inverted conversion signal (lower) for back-to-back (left) and transmission in 50 km SMF.

non-inverted conversion suffers carrier depletion at leading edge of the converted pulse, which will result red shift and carrier recovery at the falling edge causes blue shift. Namely, negative frequency chirping which compresses the pulse during the propagation in SMF happens for non-inverted conversion. This is why the non-inverted converted signal obtain negative power penalty with transmission as illustrated in fig. 4-9. The negative power penalties are -2 dB and -3.3 dB for transmission of 25 km and 50 km, respectively.

Fig. 4-10 shows eye diagrams for back-to-back and transmission. From the figure, the compression and broadening effects owing to negative and positive chirp could be observed clearly.

4.4.3 Polarization dependent performance of XPM

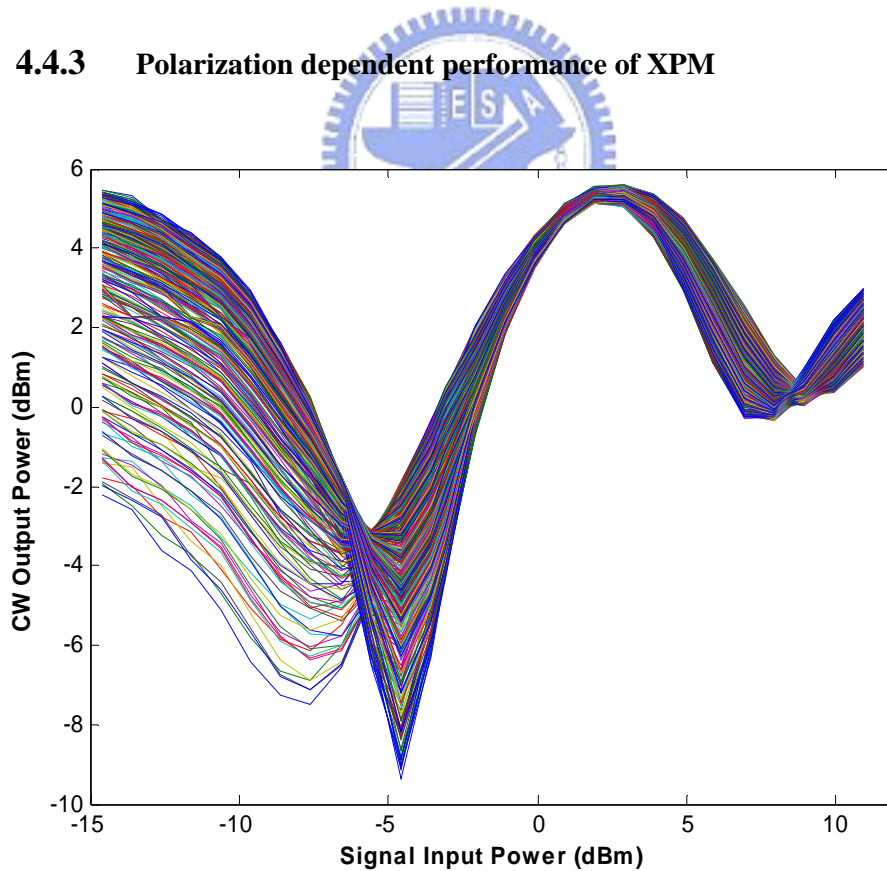


Figure 4-11: The static transfer function of XPM method on different polarization state of the input CW.

The polarization dependent transfer function of XPM method is measured and shown in fig. 4-11, in which, the currents of the phase and reference SOA are 310 mA and 222 mA and the input signal and CW are at 1555.75 nm and 1550.92 nm with CW power of 0 dBm. But the two SOA's of this module are not manufactured well for removing PDG. The maximum PDG of the phase and reference SOA's with the current of 300 mA are 2 dB and 4 dB, respectively and this results the difference

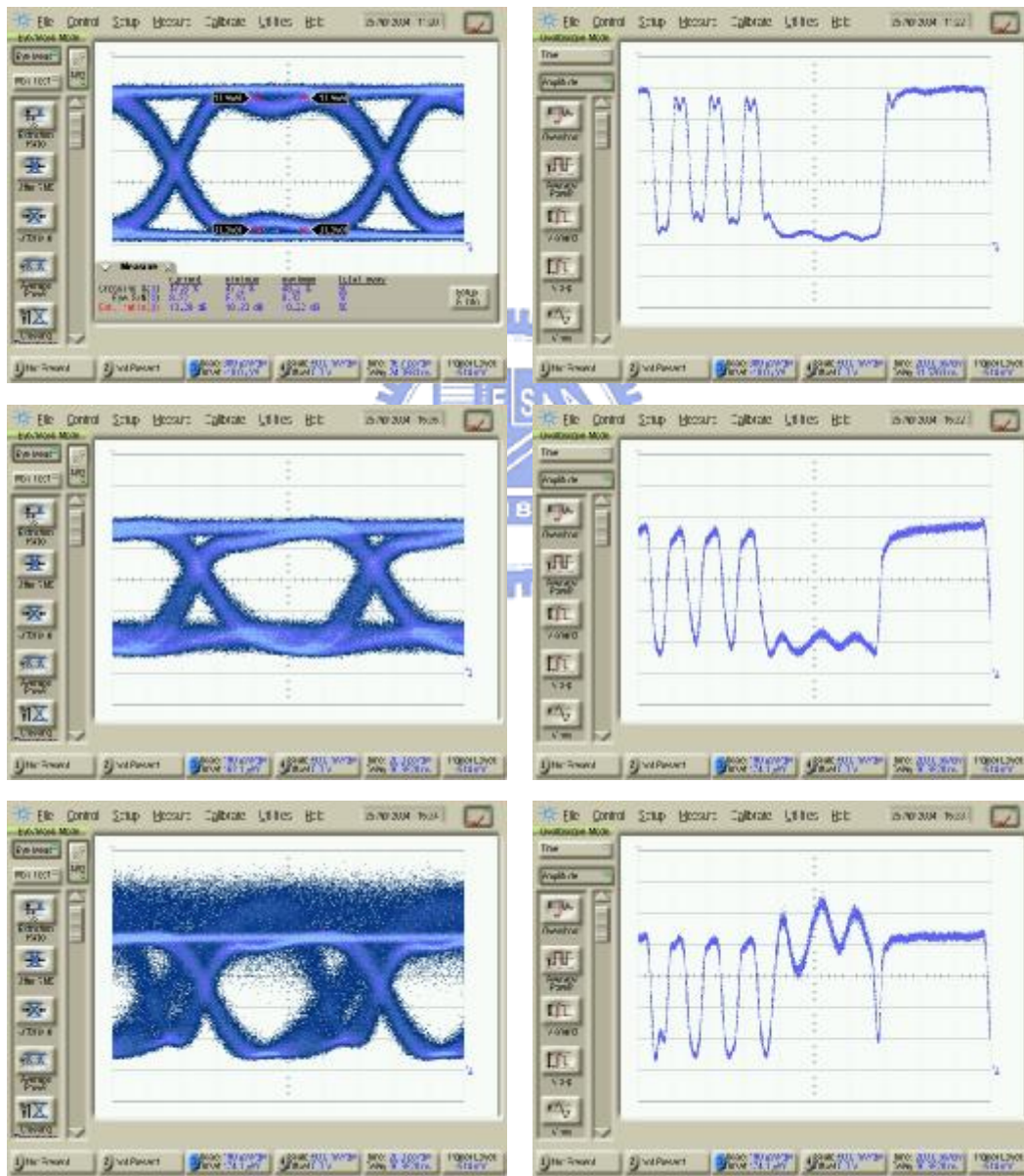


Figure 4-12: The eye diagrams and pulse patterns of the input signal (upper), the best converted signal (middle), and the worst converted signal (lower).

between the transfer functions are larger than the simulation in the fig. 3-18. The largest offset of the input signal power for minimum output power is 3 dB in the experiment. The two most different transfer functions are used to test the dynamic performance and the results are illustrated in fig. 4-12. The level one and level zero of the input signal are about 2 dBm and -8 dBm, respectively. In the fig 4-12, the best condition is corresponding to the curve which meets the minimum output for input power of -8 dBm in fig 4-11. On the other hand, the worst condition is corresponding to the other extreme static curve which causes the level one of converted signal to be folded as the pulse patterns shown in fig. 4-12.

4.3 Four Wave Mixing

4.3.1 Experimental setup

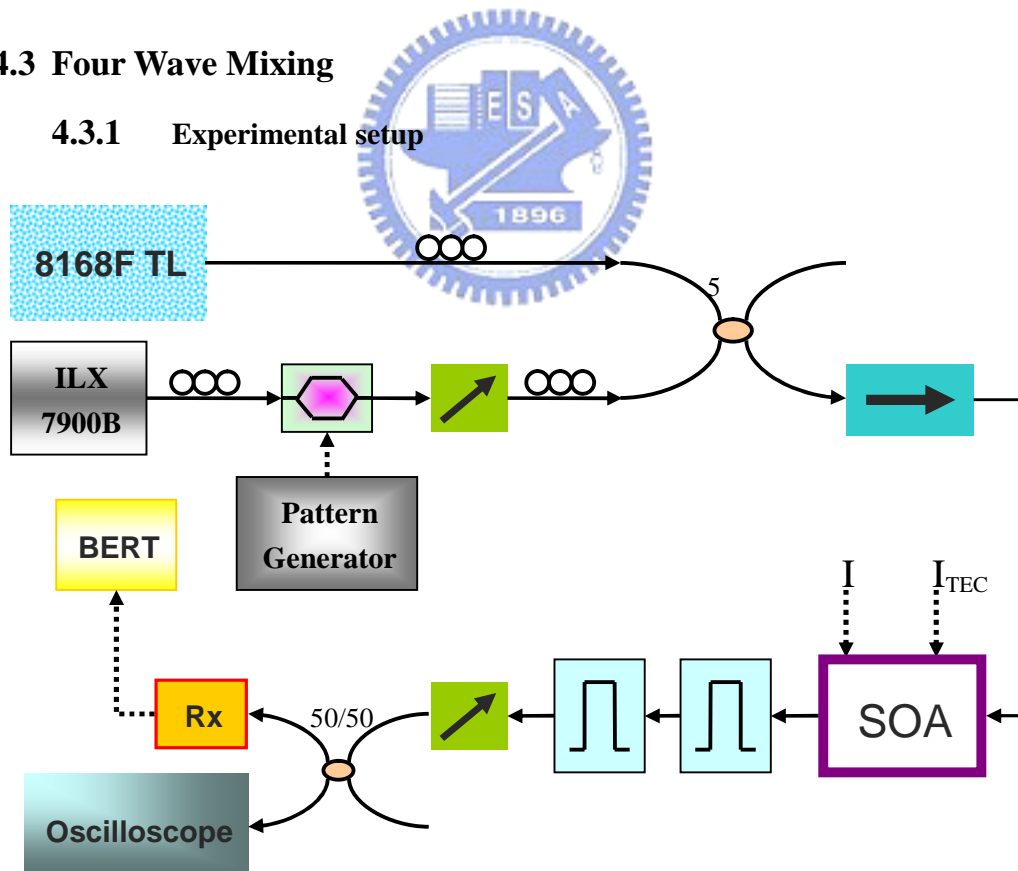


Figure 4-13: Experimental setup of FWM scheme.

The experiment setup of the FWM method is illustrated in fig. 4-13. The part of the transmitters including the input signal and CW is the same as those in the experiment using XPM method. Because FWM is a nonlinear process which the phase matching between the beating lights is very significant for, the wavelength conversion using FWM could only operated in co-propagation scheme. In other words, the optical filter is necessary in this experiment. In the experimental setup, the cascaded filters are used in order to filter out the stronger CW power. And the co-polarization is another necessary condition for this nonlinear process taking place. For this reason, there also are two polarization controllers to adjust co-polarization condition. Here, the SOA CQF872 is manufactured by JDS Uniphase.

In fig. 4-14, the conversion efficiency which is one of the major drawbacks in FWM scheme in comparison with XGM and XPM is shown. The signal wavelength

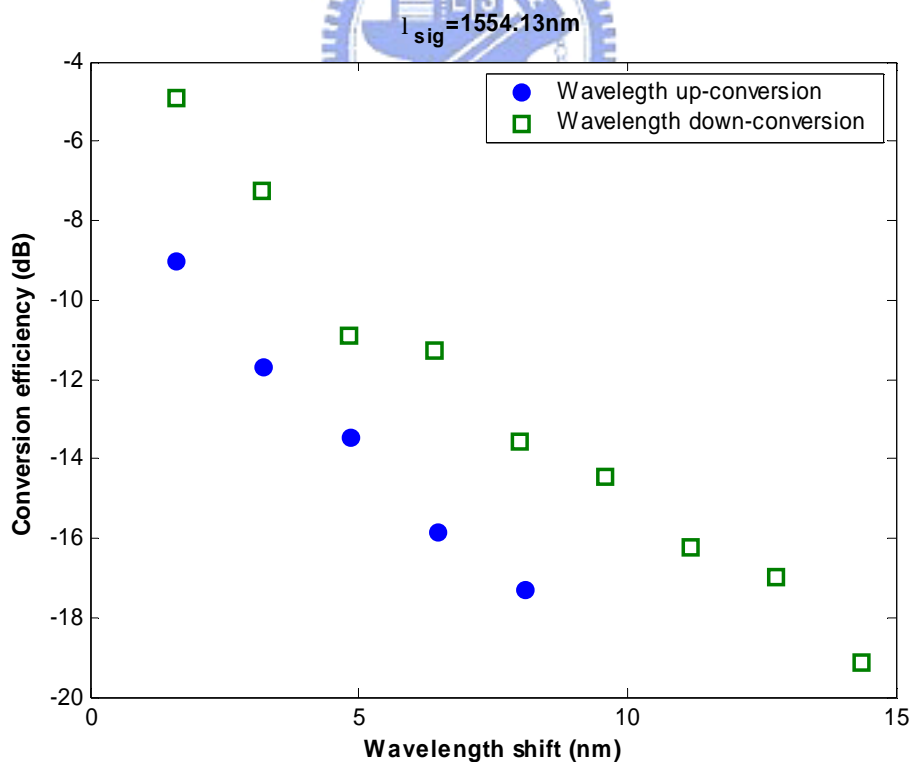


Figure 4-14: The conversion efficiency of FWM as a function of wavelength shift

and power are 1554.13 nm and -0.5 dB, and the pump (i.e. CW) power is 8 dB. The current supplied to the SOA is 300 mA. The conversion efficiency for wavelength down conversion is obviously higher than wavelength up conversion. As increasing the detuning frequency, no matter wavelength up or down conversion, the conversion efficiency decreases very quickly which is another serious problem for FWM. These two phenomena are owing to the intraband processes, and because of the limits of the bandwidth of the signal and the optical filter, the very small frequency detuning which the interband process dominates could not be practiced here.

4.3.2 Performance analysis for FWM and rFWM

In fig. 4-15, the performances of the converted signal by FWM and rFWM scheme are shown by measuring the BER curves. For the FWM scheme, the input signal is at 1554.13 nm and -2.5 dBm, and the pump is at 1552.52 nm and 8 dBm.

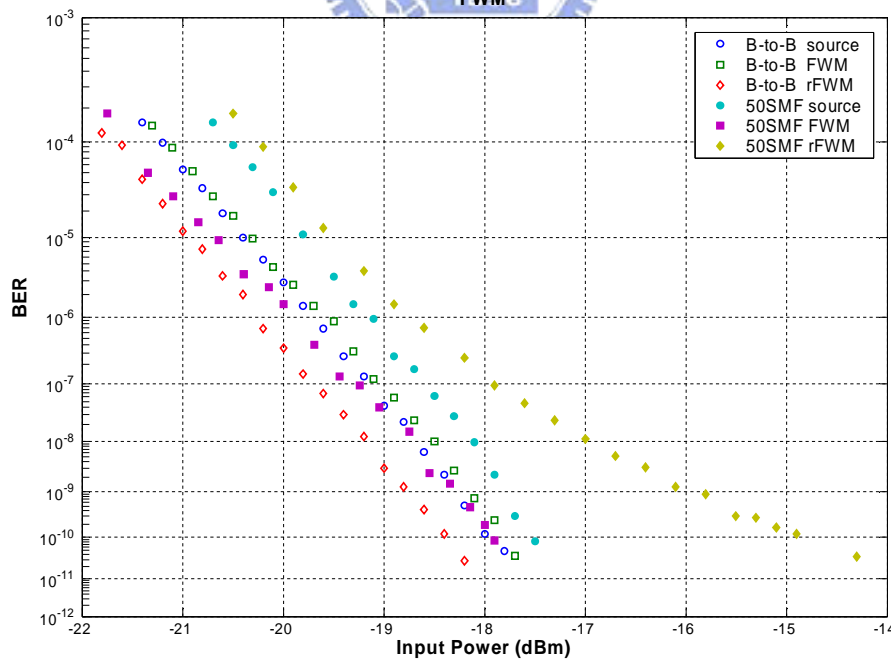


Figure 4-15: The BER curves of the input signal and converted signal by FWM and rFWM scheme for back-to-back and transmission in 50 km SMF.

Namely, the output converted signal is at 1550.92 nm. On the other hand, the input signal and pump are at 1554.13 nm, +2.5 dBm, 1555.75 nm, and 8dBm, respectively, for the rFWM scheme. In this experiment, the signal wavelength and frequency detuning are set the same for FWM and rFWM schemes, and the current of the SOA is 300 mA. From fig. 4-15, the power penalty of the converted signal by FWM for back-to-back is only about 0.1 dB compared with the back-to-back original signal. This penalty of 0.1 dB might be induced by added ASE noise of the SOA, and the effect of ER degradation may not obvious due to small signal-to-pump power ratio. For the signal converted by rFWM, however, the ER has been improved and the negative power penalty of -0.6 dB is shown in fig. 4-15. To be no different from the behavior of the positive and negative chirp in the XPM scheme, the signal converted by FWM method which causes the inverse chirp, namely, negative chirp, performs the negative power penalty of -0.1 dB for transmission in 50 km SMF compared with itself for back-to-back. The signals with positive chirp including the original signal and the converted signal by rFWM scheme behave the positive power penalties. The positive chirp of the converted signal is almost twice in comparison with the original signal. The power penalties of the original signal and the signal converted by rFWM are 0.5 dB and 2.8 dB after transmission. In addition, the penalty of 2.8 dB might be induced by not only double chirp but also the small conversion efficiency which makes the signal sensitive to added noise.

The eye diagrams of the converted signals are shown in fig. 4-16. It is clear that there is apparent overshooting at the rising edge with large signal-to-pump power ratio. On the contrary, there is little overshooting for conversion with small signal-to-pump power ratio but more noisy signals are obtained through smaller conversion efficiency, especially for the rFWM scheme. The eye diagrams for transmission are also shown in the figure.

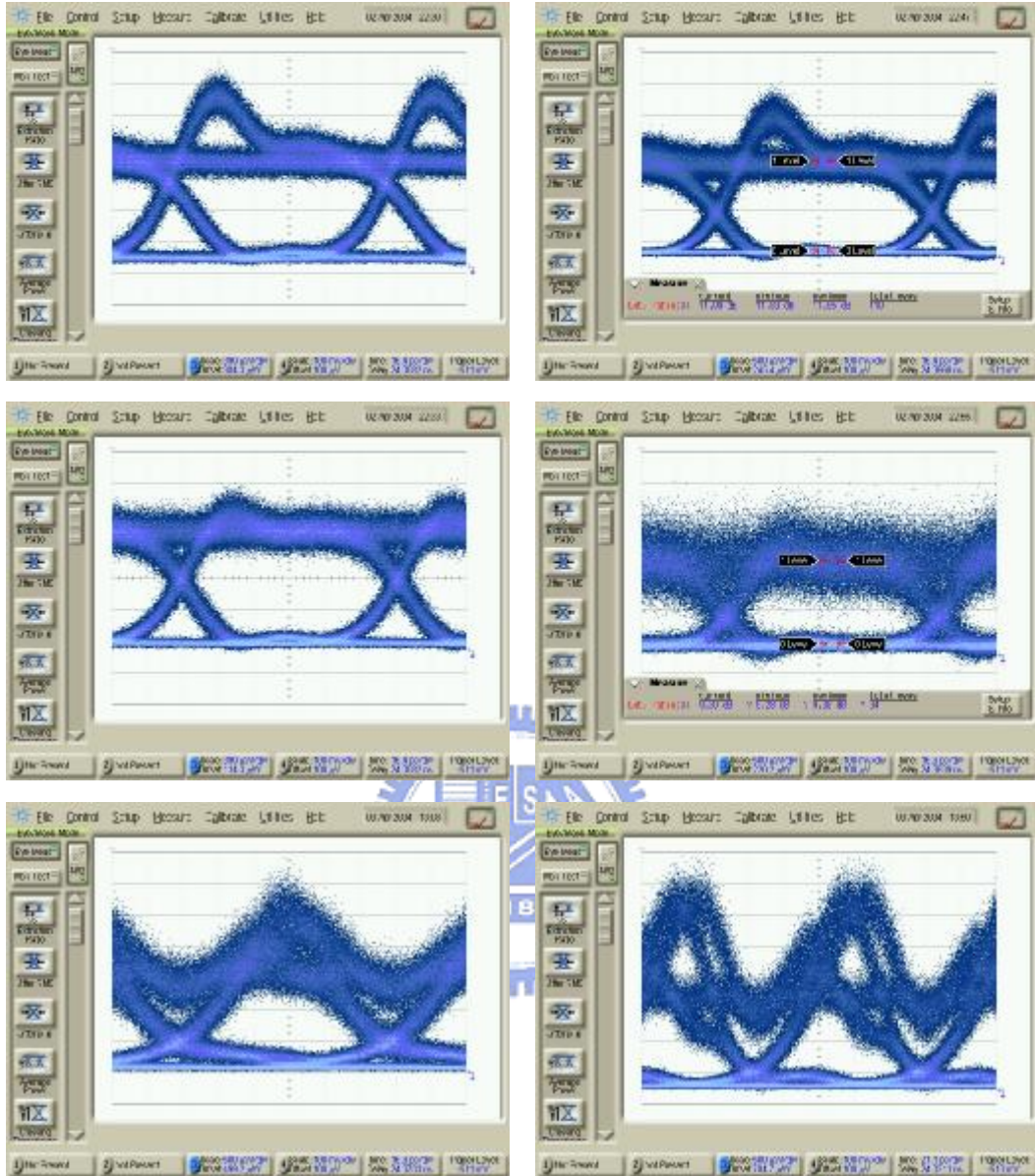


Figure 4-16: The eye diagrams of the signals converted by FWM (left) and rFWM (right) schemes. Conversion with large signal-to-pump power ratio of -4.5 dB (upper) and small signal-to-pump power ratio of -10.5 dB (middle) for back-to-back and transmission in 50 km SMF (lower).

4.4 Cross Polarization Modulation

4.4.1 Experimental setup

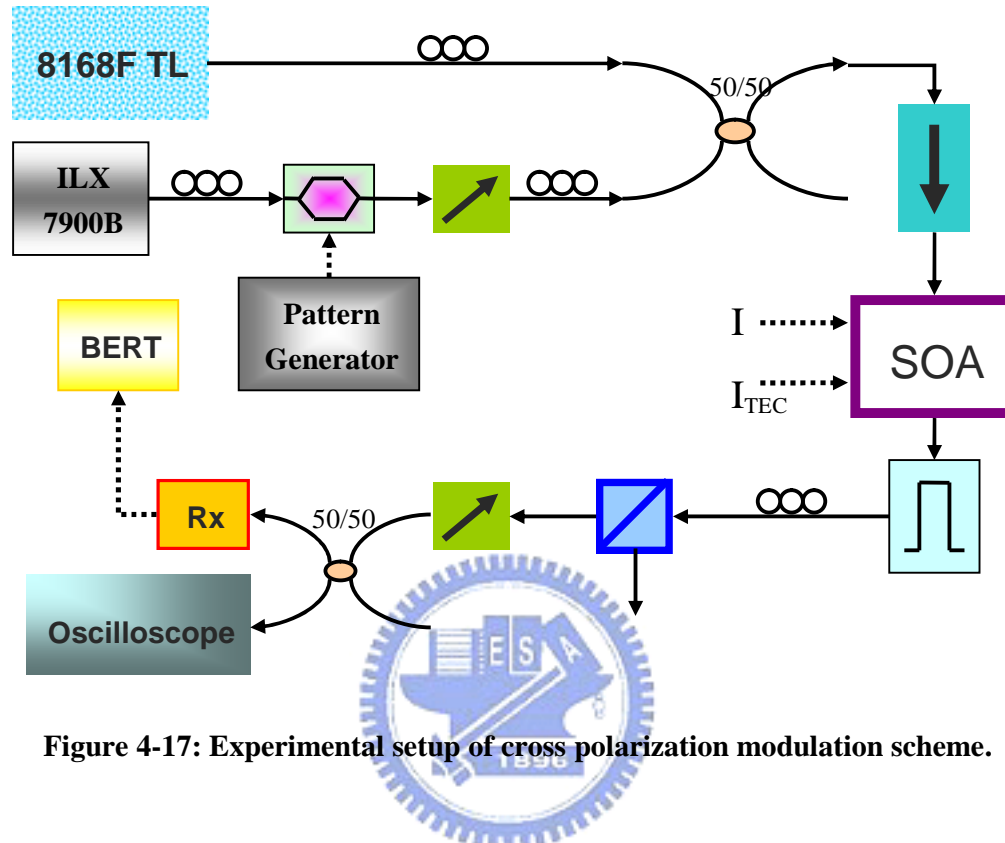


Figure 4-17: Experimental setup of cross polarization modulation scheme.

The experiment setup of cross polarization modulation scheme is shown in fig. 4-17. The setup is very similar to the experiment of FWM scheme. The differences between them are that there are one more polarization controller and a polarization beam splitter put behind the optical filter. The polarization controller and polarization beam splitter are combined and used as a tunable polarizer. In the experiment, the JDS Uniphase PBC-serious (polarization beam combiner) is used as polarization beam splitter by reversing the input and output port of the PBC.

In fig. 4-18, the measured static transfer functions of cross polarization modulation are shown. The signal wavelength is 1554.94 nm and CW is 1549.32 nm at 1 dBm. For the three solid lines operated with current of 200 mA, the operation parameters are the same at all. From these curves, the inverted or non-

inverted conversion could be choice only by detuning the tunable polarizer. Moreover, the transfer functions could be shift to matching the different average input signal power. This characteristic might be important when the signals come from different fiber paths and signal powers are dependent on the length of the fibers. In the figure, the dashed line are operated with current of 250 mA and the curves behave a little steeper.

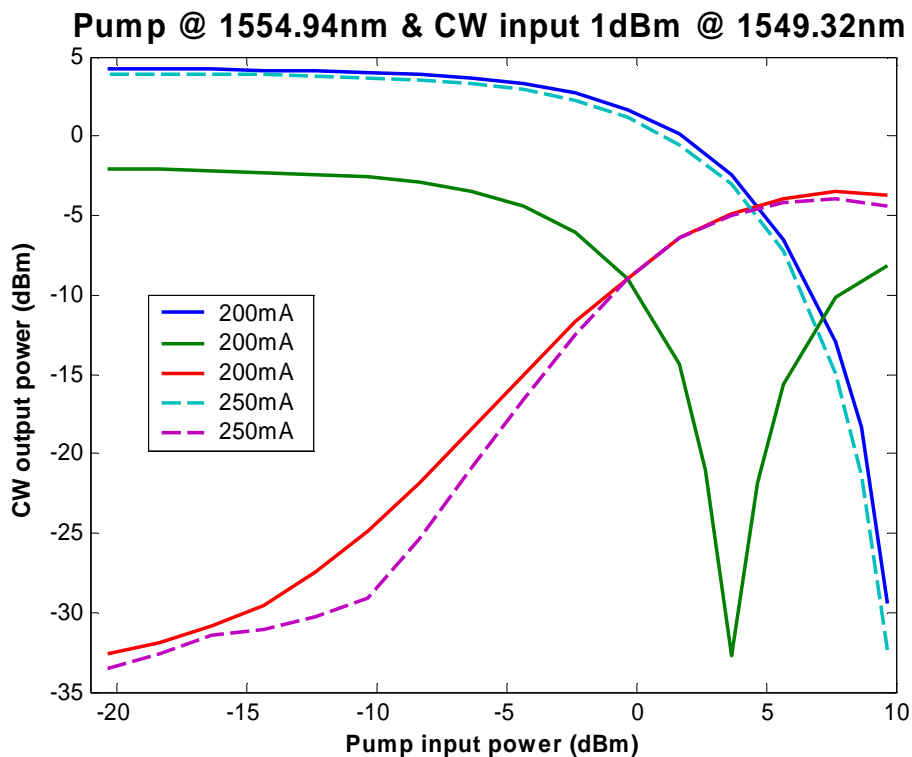


Figure 4-18: The static transfer function of cross polarization scheme.

4.4.2 Performance analysis for cross polarization modulation

As mentioned at chapter 3, the length of the SOA will influence the frequency bandwidth of modulation and the longer the SOA is, the larger the bandwidth is. In the experiments of FWM and cross polarization modulation, the JDS Uniphase SOA CQF872 is used, and the length of this SOA is shorter than the SOA manufactured by Alcatel in order to obtain higher saturation power. In other words, the performance

of the conversion signals by XGM and cross polarization at 10 Gb/s will be very bad by using the JDS Uniphase SOA. Therefore, the BER curves of 10 Gb/s conversion are not measured here. This fact also shows that the response of the FWM scheme is much larger than XGM and cross polarization modulation. The BER curves of the signal and conversion signal at 2.5 Gb/s and 5 Gb/s are shown in fig. 4-19. At low bit rate of 2.5 Gb/s, the ER of the conversion signals are improved and the negative power penalties of -0.4 dB and -0.3 dB due to the ER improvement by conversion are shown for inverted and non-inverted conversion, respectively. However, as bit rate of the signal is increased to 5 Gb/s, the power penalties are changed to 2 dB and 1.1 dB for inverted and non-inverted conversion, respectively, owing to the limit of the bandwidth. For both 2.5 Gb/s and 5 Gb/s, the signal and CW wavelength are 1554.29 nm and 1549.32 nm, respectively. The average input signal power and CW power are 1.5 dBm and 5.5 dBm, respectively. In fact, for the interferometric

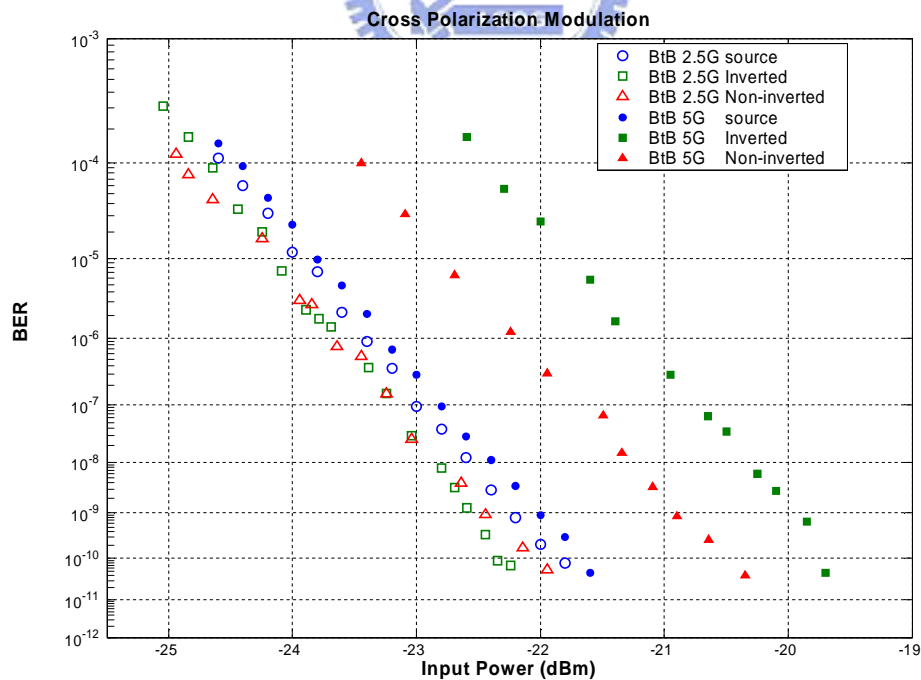


Figure 4-19: The BER curves of the original signal and conversion signals at 2.5 Gb/s and 5 Gb/s.

arrangement, a stable operation environment is very important in order to obtain good performance. But for the cross polarization modulation scheme, the fluctuation of the SOP will influence the power distribution between two arms of the interferometer. Furthermore, the output powers are no longer stable whether level one or level zero of the converted signal. This phenomenon could be seen from the power meter which displays the fluctuation of the converted signal power. The most serious condition has ever been seen is the amplitude of fluctuation of near 1 dB. It can be also appreciated clearly from the eye diagrams which would vary suddenly every a while. Therefore, even the best condition of the polarizer is found, it can't be guaranteed to be always the best condition during conversion and measuring. This is another reason that the performance of cross polarization modulation is not as good as expected.

Although the BER curves of the converted signals at high bit rate and with transmission are not illustrated in fig. 4-19, the eye diagrams of them are shown in fig. 4-20, which includes the eye diagrams at 2.5 Gb/s and 10 Gb/s with and without transmission. From the figure, the EOR degrade as the bit rate of the signal increase owing to insufficient bandwidth. On the other hand, the chirp of the converted signal is the same as using XPM scheme. The inverted signal is influenced by positive chirp and distorted seriously in SMF, but EOR of the non-inverted signal which is dominated by negative chirp become larger.

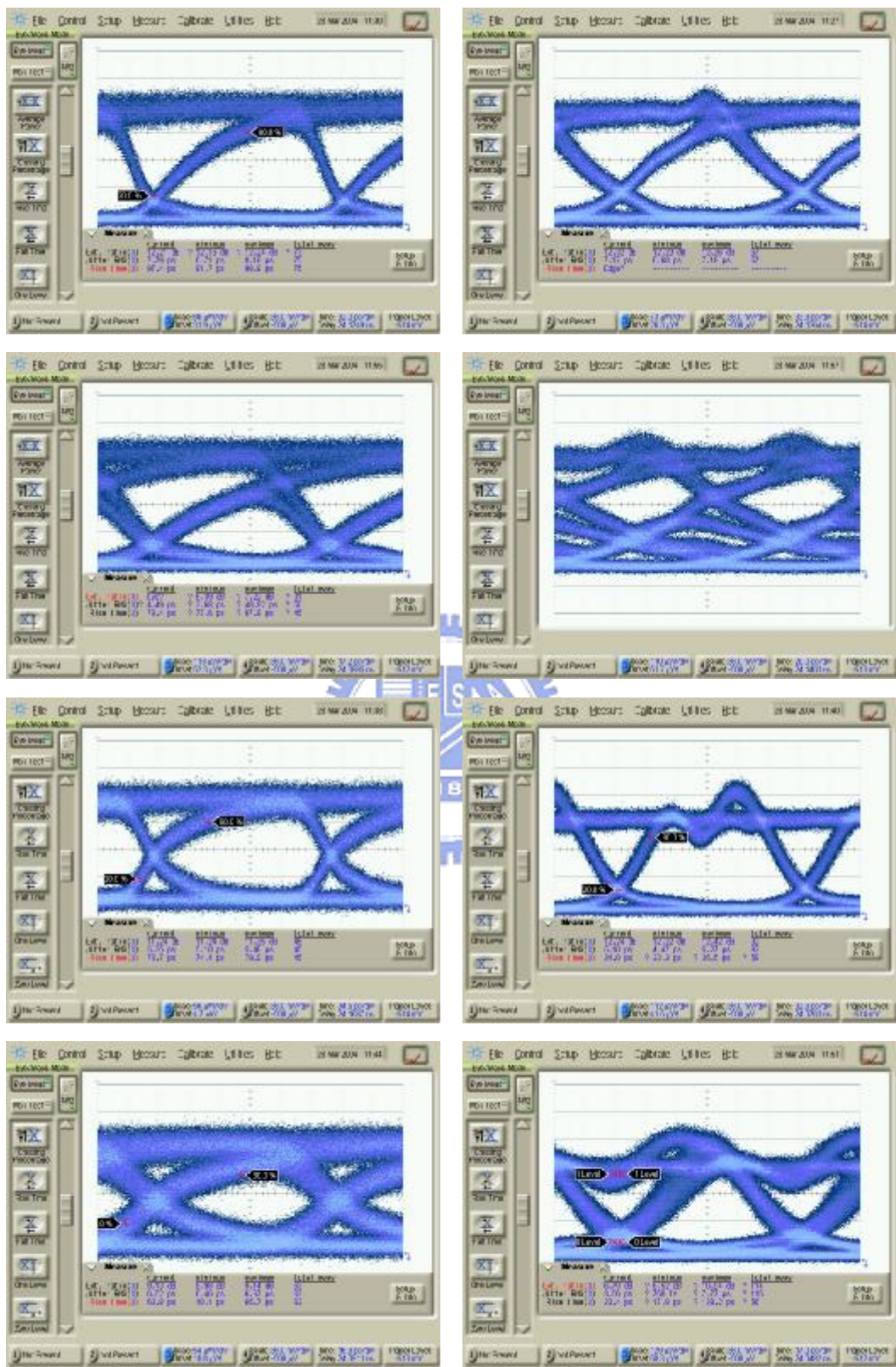


Figure 4-20: The eye diagrams of the 2.5 Gb/s inverted (1st row), 10 Gb/s inverted (2nd row), 2.5 Gb/s non-inverted (3rd row) and 10 Gb/s non-inverted (4th row) signals for back-to-back (left) and transmission in 50 km SMF (right).

4.4.3 Wavelength conversion to different wavelengths

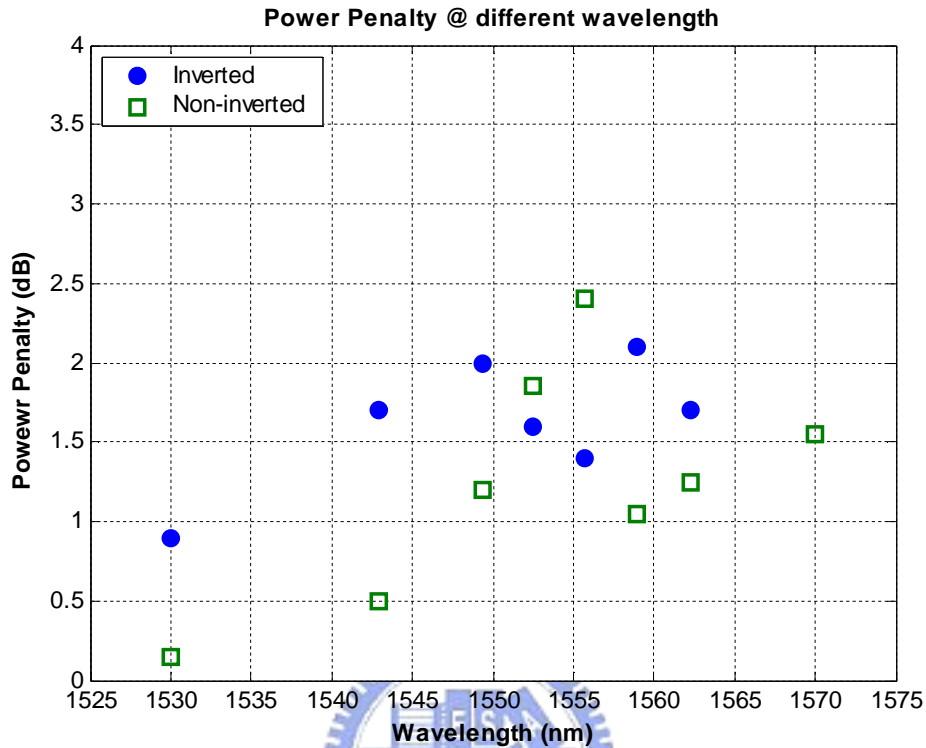


Figure 4-21: The power penalties of the converted signal by cross polarization modulation as a function of CW wavelength.

The wavelength conversion to different wavelengths by cross polarization modulation is measured, and the performances of them are represented by the power penalties illustrated in fig. 4-21. In the experiment, the signal is 1554.94 nm, 5.5 dBm at 5 Gb/s and CW power is 1.5 dBm. Most of the power penalties are under 2 dB, and the result shows little dependence on the CE wavelength. Moreover, it seems somewhat irregular which is probably because the polarizer is not guaranteed to be operated at best conditions every times.

CHAPTER 5

CONCLUSION

5.1 Summary

Wavelength conversion will become an important function in WDM systems and photonic switch blocks. In this thesis, the simulations and experiments of four kinds of the wavelength converters which include the XGM, XPM, FWM, and cross polarization modulation in SOA's have been done. The simulations by the program, MatLab, are helpful for realizing the details of the mechanisms. It is also very convenient to set different parameters. The parameters include not only the currents, wavelengths and powers which are easy to change in experiments but also the length, confinement factor, and linewidth enhancement factor of SOA's which are difficult to change unless the specially made SOA's are bought. Moreover, the phase information of a signal is hard to be measured which is only compared by using the dispersion of SMF, and in the simulations the frequency chirping is calculated following the amplitude information. As the results of the simulations shown in chapter 3, the shapes, ER's, frequency chirpings, EOR's, conversion efficiency, and static transfer functions of converted signals and carrier distribution of SOA's are calculated. However, the parameters used in simulations may not always realistic, and some parameters are not easy to set in order to get the best performance of the converted signals especially for signals at very high bit rate. Therefore, the experiments are important for retrieve these drawbacks of the simulations and used to prove or be compared with the results of the simulations.

For XGM scheme, the most important advantage is easy. It is indeed easy to set up and the best parameters are also easy to find and be adjusted. However, the serious problems are the high positive frequency chirping and ER degradation for

wavelength up-conversion which becomes more and more serious when the signal pass through several wavelength converters by XGM.

For XPM scheme, it has very good performance of the converted signals, such as lower frequency chirping, ER improvement, and free choices between inverted and non-inverted conversion. If the non-inverted scheme is selected, the negative chirp which will cause negative power penalties with transmission in SMF is accompanied with wavelength conversion. But it is very complicated and troublesome to find the best operations because of too many parameters influencing the result. The polarization dependence is another trouble even using so-called polarization independent SOA's. As shown in the simulation and experiment, the SOP of the CW may affect the performance of the converted signals strongly.

For FWM scheme, the bit rate and signal format transparency are very attractive. But it is lamentable that the conversion efficiency of FWM is so low and therefore may be very noisy, as well as the polarization sensitivity is also troublesome. In addition the ER of the converted signals may degrade a little. Although this problem could be solve by using a similar scheme rFWM which could enlarge the ER of the output signal, it suffers another serious problem in which the frequency chirping of the original signal will be converted double and the chirp is usually positive.

For cross polarization modulation, it is very similar to XPM scheme. Namely, it is also an interferometer in which only one SOA is needed and the operation is not so complicated compared with XPM. The same as XPM, non-inverted and inverted conversion could be chosen free as well as the characteristics of the frequency chirping. Nevertheless, the conversion efficiency is also too low like FWM compared with XGM and XPM in which the efficiency could be larger than 0 dB and the unstable output power and performance due to the fluctuation of the SOP are main drawbacks of this scheme.

5.2 Future Works

For the time being, there is still no the best solution for wavelength conversion although so many methods are proposed. However, many disadvantages of wavelength converters by using SOA's are owing to the insufficient characteristics of SOA's. It has been proposed [18] that the quantum dot SOA own many qualities, such as very wide gain bandwidths, inhomogeneous broadened gain spectra, high saturation powers, fast gain dynamics and a low linewidth enhancement factor, which are useful for wavelength conversion and could improve the converted performance as general bulk or quantum well SOA's used. Therefore, a specially made quantum dot SOA might be bought and used to be a wavelength converter in XGM and FWM scheme. On the other hand, the SOA which employs a strained active region is polarization dependent and the PDG of this kind of SOA's is larger than common SOA's. It also could be used in cross polarization scheme for improving the degree of polarization rotation. Furthermore, if a tunable polarizer is set behind the SOA in the experimental setup of FWM, the ER of the converted signal might be improved. Yet, the too small conversion efficiency is the most important question which must be overcome to realize this idea.

REFERENCE

- [1]. J. S. Perino, J. M. Wiesenfeld, and B. Glance, "Fiber Transmission of 10Gbit/s Signals Following Wavelength Conversion Using a Travelling-Wave Semiconductor Optical Amplifier" , *Electron. Lett.*, Vol.30, pp. 256-258, 1994.
- [2]. T. Durhuus, C. Joergensen, B. Mikkelsen, R.J.S. Pedersen, and K.E. Stubkjaer, "All Optical Wavelength Conversion by SOA's in a Mach-Zehnder Configuration," *IEEE Photon. Tech. Lett.*, vol. 6, pp. 53-55, 1994.
- [3]. D. F. Geraghty, R. B. Lee, K. J. Vahala, M. Verdiell, M. Ziari, and A. Mathur, "Wavelength Conversion up to 18 nm at 10 Gb/s by Four-Wave Mixing in a Semiconductor Optical Amplifier," *IEEE Photon. Tech. Lett.*, vol. 9, pp. 452-454, 1997.
- [4]. Y. Liu, M. T. Hill, E. Tangdiongga, H. de Waardt, N. Calabretta, G. D. Khoe, and H. H. S. Dorren, "Wavelength Conversion Using Nonlinear Polarization Rotation in a Single Semiconductor Optical Amplifier," *IEEE Photon. Tech. Lett.*, vol. 15, pp. 90-92, 2003.
- [5]. S. Hojfeldt, S. Bischoff, and J. Mork, "All-Optical Wavelength Conversion and Signal Regeneration Using an Electroabsorption Modulator," *J. Lightwave Tech.*, vol. 18, pp. 1121-1127, 2000.
- [6]. S. Tadanaga, M. Asobe, H. Miyazawa, Y. Nishida, and H. Suzuki, "A 1-THz Optical Frequency Shifter Using Quasi-phase-matched LiNbO₃ Wavelength Converters," *OFC'02*, paper ThDD, 2002.
- [7]. M. Fujiwara, J. Kani, H. Suzuki, K. Araya, and M. Teshima, "Flattened Optical Multicarrier Generation of 12.5GHz Spaced 256 Channels Based on

Sinusoidal Amplitude and Phase Hybrid Modulation,” *Electron. Lett.*, vol. 37 ,pp.967-968, 2001.

- [8]. M. J. O’Mahony, “Semiconductor Laser Optical Amplifiers for Use in Future Fiber Systems,” *J. Lightwave Tech.*, vol. 6, pp. 531-544, 1988.
- [9]. A. E. Willner and W. Shieh, “Optimal Spectral and Power Parameters for All Optical Wavelength Shifting: Single Stage, Fanout, and Cascadability,” *J. Lightwave Tech.*, vol. 13, pp. 771-781, May 1995.
- [10]. G. P. Agrawal, and N. A. Olsson, “Self-Phase Modulation and Spectral Broadening of Optical Pulseds in Semiconductor Laser Amplifiers,” *IEEE J. Quantum Electron.*, vol. 25, pp. 2297-2306, 1989.
- [11]. G. P. Agrawal, and N. K. Dutta, *Long-Wavelength Semiconductor Lasers*. New York: Van Nostrand Reinhold, ch. 2, 1986.
- [12]. A. Uskov, J. Mork, and J. Mark, “Wave Mixing in Semiconductor Laser Amplifiers Due to Carrier Heating and Spectral-Hole Burning,” *IEEE J. Quantum Electron.*, vol. 30, pp. 1769-1781, 1994.
- [13]. M. G. Davis and R. F. O’Dowd, “A Transfer Matrix Method Based Large-Signal Dynamic Model for Multi-Electrode DFB Lasers,” *IEEE J. Quantum Electron.*, vol. 30, pp. 2458-2466, 1994.
- [14]. H. Lee, H. Yoon, Y. Kim, and J. Jeong, “Theoretical Study of Frequency Chirping and Extinction Ratio of Wavelength-Converted Optical Signals by XGM and XPM Using SOA’s,” *IEEE J. Quantum Electron.*, vol. 35, pp. 1213-1219, 1999.
- [15]. D. Marcenac, “Travelling Wave Effects for Wavelength Conversion by Cross-Gain and Cross-Phase Modulation in Optical Amplifiers,” *International J. Optoelectron.*, vol. 10, pp 325-329, 1995.

- [16]. Y. Kim, H. Lee, S. Kim, J. Ko, and J. Jeong, "Analysis of Frequency Chirping and Extinction Ratio of Optical Phase Conjugate Signals by Four-Wave Mixing in SOA's," *IEEE J. Sel. Top. Quantum Electron.*, vol. 5, pp. 873-879, 1999.
- [17]. K. Obermann, S. Kindt, D. Breuer, and K. Petermann, "Performance Analysis of Wavelength Converters Based on Cross-Gain Modulation in Semiconductor-Optical Amplifiers," *J. Lightwave Tech.*, vol. 16, pp. 78-85, 1998.
- [18]. A. Bilenca, R. Alizon, d. Dahan, G. Eisenstein, R. Schwerberger, D. Gold, J. Reithmaier, and a. Forchel, "Multi-THz Wavelength Conversion by Four Wave Mixing and Cross Gain Modulation in an InAs/InP Quantum Dash Semiconductor Optical Amplifier Operating at 1550nm," *OFC'03*, paper ThO2, 2003.

